CLOUD OBSERVATIONS FROM THE MARS SCIENCE LABORATORY MISSION: SEASONAL VARIABILITY, SCATTERING PHASE FUNCTION, AND VALIDATION OF OPTICAL DEPTHS USING LIDAR MEASUREMENTS OF TERRESTRIAL CIRRUS CLOUDS

JACOB KLOOS

A THESIS SUBMITTED TO
THE FACULTY OF GRADUATE STUDIES
IN PARTIAL FULFILMENT OF THE REQUIREMENTS
FOR THE DEGREE OF

MASTER OF SCIENCE

GRADUATE PROGRAM IN EARTH AND SPACE SCIENCE
YORK UNIVERSITY
TORONTO, ONTARIO

September 2016

Abstract

Using images from the Navigation Cameras onboard the Mars Science Laboratory (MSL) rover Curiosity, atmospheric movies were created to monitor the cloud activity above its landing site, Gale Crater. Over the course of two Martian years of operations ($L_S = 160^\circ$ of MY 31 to $L_S = 160^\circ$ of MY 33), over 500 cloud imaging sequences have been returned to Earth, revealing tenuous clouds that form predominantly in the autumn and winter seasons. This thesis examines the results of these cloud observations, including a detailed overview of the seasonality, opacity, spacing, and scattering properties of the clouds that appear in the observations. The cloud opacities were validated by testing the high cloud method by imaging high altitude cirrus clouds using a radiometrically calibrated camera and capturing simultaneous measurements wth the York University Lidar. In total, four coordinated experiments were conducted between September of 2015 and June of 2016.

Dedication

I would like to dedicate this work to my mother.

Acknowledgements

I would first like to express my sincerest appreciation to my supervisor, Dr. John Moores, for his guidance and support over the last two years. It has been both a pleasure and an honour to have him as a supervisor. The earnestness with which he approaches his job as a scientist, an engineer, and an educator has been a source of inspiration to me, and I look forward to the next four years of working together.

I would also like to give a big thanks to Monika Aggarwal for donating so much of her time to acquire the lidar measurements. Coordinating the experiments was not always easy as the weather in Toronto can shift quickly. Acquiring the necessary data often required short notice and sometimes staying late, and yet Monika was always willing to help out - often at the expense of rearranging her schedule.

Thank you also to Dr. Mark Gordon, Dr. Jim Whiteway, and Dr. Patrick Hall for kindly agreeing to serve as members of my examining committee. Their expertise during the exam was very insightful, and the feedback they provided has substantially improved the substance and quality of my thesis.

I would also like to thank all of the other members of the Planetary Volatiles Laboratory for their encouragement and support. A special thanks to Casey Moore and Christina Smith for editing my thesis and for the useful advice before my defence.

Finally, thank you to my family for their love and support. Love you guys.

Table of Contents

List of Tables

List of Figures

Chapter 1

Introduction

Over the past few centuries, the Martian climate has been widely studied through a combined effort of telescopic monitoring, orbital remote sensing, and surface remote sensing measurements. Historically, our drive to understand Mars and the physics and chemistry of its environment has been propelled by the possible existence, past or present, of indigenous life on its surface. Studying the Martian climate, however, is also valuable as it can lend insight into the complex feedback systems that exist within the environment in which we live. Earth's climate is a complex network containing elaborate connections between its various systems, and it is often difficult to account for all of its interactions in even the most sophisticated atmospheric models. Studying the Martian climate represents an opportunity to untangle and isolate these complex interactions through comparison with the terrestrial system.

While ground-based telescopic observations provided information on the basic properties of Mars, such as its size and rate of rotation, our current understanding of its climate has been revealed through the high resolution measurements obtained from orbital and surface spacecraft. At present, there are three orbiting spacecraft and two surface vehicles that are operational and actively returning data from Mars. One of the surface vehicles is NASA's Mars Science Laboratory (MSL) rover Curiosity, which landed on the surface in August of 2012 within an equatorial region of the planet (Vasavada et al. 2014). The mission's primary focus is to investigate the past environment of Mars which is achieved through geologic remote sensing, however Curiosity has also returned a wealth of data concerning the local and regional present day environment of its landing site (Audouard et al. 2015; Pla-García and Rafkin 2015; Savijärvi, Harri, and Kemppinen 2015).

Among the environmental investigations conducted by Curiosity are studies into the regional cloud activity (Moores et al. 2015a; Kloos et al. 2016). From the onset of the mission, Curiosity has executed two separate cloud imaging observations that have captured tenuous,

sub-optical water-ice and dust clouds in the skies of its landing site. These observations have been executed with a regular frequency, and in two Martian years these sequences have accumulated into a data set extending to just over 500 observations. Each observation, also referred to in this document as a movie, consists of a sequence of images captured using a specific pointing of the rover's Navigation Cameras (NavCam): Zenith Movies use a vertical pointing while Supra-Horizon Movies use a lower elevation angle pointing. The MSL cloud movies are structured around similar observations conducted by the Phoenix lander, which observed both water-ice and dust clouds over the course of its 151 sol mission (Moores et al. 2010). Similarly, the MSL cloud movies have captured water-ice and dust clouds, while the long collection period of the movies has enabled seasonal patterns of cloud formation to be observed.

It is well known that condensate clouds can play a substantial role in the global climate by both reflecting solar radiation into space, as well as absorbing upwelling Infrared Radiation (IR) from the surface. Recent work has shown that Martian clouds exhibit a measurable impact on the environment, and that their radiative influence must be taken into account within Global Circulation Models (GCMs) to accurately determine regional surface temperatures (Richardson, Wilson, and Rodin 2002; Hinson and Wilson 2004; Montmessin et al. 2004; Wilson, Neumann, and Smith 2007). The specific radiative influence that clouds have on their environment depends on the cloud altitude and geographical location, but also on the specific optical properties of the cloud. Of particular importance is the optical depth of the cloud, which is a measure of the amount of light that is attenuated through scattering and absorption by the cloud's constituent particles. Values of cloud optical depth, or opacity, provide information on the amount material that is present in the cloud, and are a functional parameter used in GCMs.

Over the years, a large catalogue of Martian cloud opacities has been established primarily through orbital remote sensing techniques (Clancy, Wolff, and Christensen 2003; Smith et al. 2003; Hale et al. 2011). Opacity measurements are also made for clouds in the MSL observations through the use of radiative transfer equations and spectral radiance values obtained from the NavCam images. Moores et al. (2015a) and Kloos et al. (2016) have detailed two separate methods used for deriving cloud opacity: the whole atmosphere method and the high cloud method. Each method makes specific assumptions about the scattering properties, and thus composition, of the imaged clouds; the high cloud method is appropriate for high altitude, optically thin water-ice clouds while the whole atmosphere method is appropriate for low-lying dust clouds. Because the cloud composition cannot be known a priori, the composition must be inferred using orbital observations of clouds at equatorial latitudes, as well as any morphologic expression that the clouds might exhibit over the time

span of the observation.

The high cloud method is particularly significant given that it is appropriate for water-ice clouds, which have an important role in the Martian climate. The high cloud method was first introduced by Moores et al. (2015a) due to orbital data showing the presence of discrete water-ice clouds in equatorial regions during late autumn and winter in the southern hemisphere. Due to the novelty of this method, it has only been examined theoretically, and not experimentally. To quantitatively assess the high cloud method, and therefore validate the values reported by Moores et al. (2015a) and Kloos et al. (2016), the MSL NavCam movies were adapted to the terrestrial environment. Four coordinated experiments were conducted in which a radiometrically calibrated camera was used to image high altitude cirrus clouds while concurrent lidar (light detection and ranging) measurements of the imaged clouds were made by the York University lidar instrument in Toronto, Ontario. The lidar provides a measure of the cloud opacity which is then compared with the camera-derived value calculated using the high cloud method.

This thesis will give a comprehensive survey of the MSL cloud observations, providing a detailed examination of the observational parameters, analysis methods, as well as the findings over a two Martian year period. Chapter 2 will provide the reader with the necessary background information on the Martian climate, including a brief history of the preceding cloud investigations that will help to place the MSL work in context. Chapter 3 will describe the MSL data set which will include a description of the Zenith and Supra-Horizon Movies, as well as a detailed overview of the analysis techniques used. The results of the MSL work is detailed in chapter 4, which describes the observed cloud seasonality and opacity measurements as well as a discussion of the significance of the results. Chapter 5 will give an overview of the experimental setup of the terrestrial experiments, while chapter 6 will present the experimental results of the lidar-coordinated experiments, which will include a discussion of how the MSL opacity computational methods compare with the lidar values, and a description of the significance to the MSL work.

Chapter 2

Background Information

2.1 An Introduction to the Martian Climate

In many ways, Mars is the most Earth-like planet in our solar system. Its rotational period is only 39.5 minutes longer than Earth's, and it experiences distinct hemispheric seasons owing to the 25.2° tilt of its equatorial plane relative to its orbital plane. The seasons are further enabled by a thin atmosphere which hosts a complex global weather cycle, driven, as is on Earth, by differential equator-pole heating from the Sun. The differential heating produces atmospheric circulation patterns, allowing material and energy to be transported around the planet, giving rise to familiar processes and events such as wind, condensation, dust storms, and ultimately even a hydrological and carbon cycle.

While similarities between the terrestrial and Martian environments can be found, the present day Martian atmosphere is very different from Earth's. By volume, the atmosphere of Mars is composed of 95% carbon dioxide (CO_2), 2.7% nitrogen (N_2), 1.6% argon (Ar), and 0.13% oxygen (O_2), with trace amounts of water vapour. The pressure at the surface of Mars is exceedingly low, and varies between 4 and 8.7 mbar depending on the geographic location and season. During winter in each hemisphere, the temperatures in the polar regions drop below the frost point of CO_2, allowing the atmosphere's major constituent to condense as an ice, resulting in a decrease in global pressure. As temperatures increase during the spring and summer, the CO_2 sublimates, where it is then released back into the atmosphere.

Additionally, the orbit of Mars is more eccentric than that of Earth's, resulting in as much as a 40% fluctuation in total solar insolation over the course of one full orbital revolution. The large disparity in seasonal solar energy leads to asymmetries between seasons in the northern and southern hemispheres, and even causes synoptic-scale weather patterns to emerge (Clancy et al. 1996). The current orbital configuration of Mars is such that winter in the southern hemisphere occurs when Mars is approaching aphelion, which leads to more

extreme winter seasons in the southern hemisphere relative to the northern.

In addition to CO_2 ice, the Martian polar caps are also composed of water-ice, which is also seasonally exchanged into the atmosphere. As temperatures rise during summer in the respective hemisphere, the solid water that makes up the polar caps begin to sublimate, where it enters into the atmosphere and is driven equator-ward by wind. The north polar cap is substantially larger than that of the southern cap, and thus more water is released into the atmosphere during northern summer, which is important for the observed seasonal and spatial distribution of condensate water-ice clouds. It is worth noting, however, that the amount of water contained in the atmosphere of Mars is exceedingly low. Measurements of the column abundance of water vapour averaged over the entire globe for one Mars year amounts to only $10 - 15$ precipitable microns ($pr.\mu m$) (Jakosky and Farmer 1982; Trokhimovskiy et al. 2015). The term precipitable micron is used to describe the height, or thickness, of liquid water that would occur from condensing out all of the vapour in a column of atmosphere. Thus, if all of the water vapour contained in the atmosphere of Mars were to be condensed into a liquid and allowed to fall to the surface, it would form a layer of water $10 - 15$ μm in depth covering the entire globe of Mars.

A prominent feature of Mars is the dichotomy boundary, which is a steep change in elevation that divides the northern and southern hemispheres. The southern hemisphere is a heavily cratered plateau elevated 2-3 km above the relatively smooth northern hemispheric plains. The topographical relief is large enough to influence meridional wind circulation patterns, which is important for the formation of equatorial water-ice clouds. The dichotomy boundary acts as a barrier, forcing air upwards and allowing for saturation of air, and condensation of water-vapour, to occur (Montmessin et al. 2007). The following section will discuss some of the cloud observations made by orbital and surface spacecraft to provide the reader with a broader context for the MSL cloud observations.

Before moving on, however, it is first necessary to clarify some of the time-keeping terminology on Mars that will be used frequently throughout this work. The first is known as aerocentric solar longitude, denoted as L_S, and is used to keep track of the season. An arbitrary convention was chosen, such that $L_S = 0^\circ$ marks the beginning of spring, $L_S = 90^\circ$ marks the beginning of summer, $L_S = 180^\circ$ of Autumn and $L_S = 270^\circ$ of winter in the northern hemisphere. Secondly, to conveniently compare seasonal data between successive Mars years, a convention was established by Clancy et al. (2000) in which $L_S = 0^\circ$ on April 11, 1955 marks the beginning of Mars Year (MY) 1. The current MY at the time of writing is 33.

2.2 Martian Clouds

Consistent Earth-based telescopic imaging of Mars, particularly in the last century, enabled the first insights into the variability of water-ice clouds to be made. Reporting on ground-based data collected between 1924 and 1971, Smith and Smith (1972) observed discrete white clouds preferentially forming during late spring and early summer in the northern hemisphere, with the peak activity occurring between $L_S = 90^\circ - 130^\circ$. Diurnal variation was also observed, with increased cloud activity in the late morning and early afternoon corresponding to the same seasonal time period of increased formation. The enhanced cloud activity reported was centralized in the Tharsis region, which is a volcanic plateau that rises 7 km above the surrounding plains, and hosts a number of large topographic features, such as the Prince volcanoes and Olympus Mons.

The Tharsis region was examined from close up when the Mariner 6 and 7 probes flew by Mars in February and August of 1969, respectively. Analyzing images returned from these flybys, Peale (1973) observed cloud formation at a similar time of day and year consistent with Smith and Smith (1972), and further suggested that the diurnal variability could indicate an exchange of water vapour between the atmosphere and the surface, which is induced by the warming and cooling surface. Using the Infrared Spectrometer on the Mariner 9 orbiter, Curran et al. (1973) provided spectroscopic evidence that the clouds associated with the Tharsis region were composed of water-ice. The seasonality of water-ice clouds was studied for the Tharsis and Valles Marineris region by Benson et al. (2003) using high-resolution global maps acquired with the Mars Orbiter Camera on the Mars Global Surveyor spacecraft. They reported that the peak in cloud activity at $L_S = 120^\circ$ corresponds with peak in column water abundances obtained by Jakosky and Farmer (1982) in the northern hemisphere, suggesting that the seasonality in cloud activity is due to the increased presence of atmospheric water vapour.

The surge in cloud activity above the Tharsis region and other regions of equatorial latitudes occurs as Mars is beginning to approach aphelion, which is centred around $L_S = 71^\circ$. The eccentricity of Mars' orbit is great enough for the increased orbital distance during aphelion to decrease atmospheric temperatures by 20 K, allowing for increased saturation conditions. This effect is so pronounced that the increased distance during aphelion is responsible for a distinct "season," which is characterized by a globally extant belt of optically thin water-ice clouds covering equatorial regions of the planet. This belt of water-ice clouds is known as the Aphelion Cloud Belt (ACB), and is an annually recurring feature on Mars.

Orbital observations have shown that the ACB is primarily confined to a latitude range of $10^\circ S - 30^\circ N$, and begins to develop around $L_S = 40^\circ - 60^\circ$ and disappears around $L_S = 150^\circ$

(Clancy et al. 1996; Madeleine et al. 2012; Mateshvili et al. 2007; Wang and Ingersoll 2002; Wolff et al. 1999). Both Clancy et al. (1996) and Wolff et al. (1999) observe that the cloud belt is offset 10° north of the equator, and find a maximal cloud optical thickness occurring between $L_S = 60° - 100°$. The range of cloud opacities during this period measured by Clancy et al. (1996) was 0.2 and 0.6.

Cloud imaging from the surface of Mars has been relatively rare, as surface vehicles focus primarily on geologic research. The Mars Exploration Rovers (MER) Spirit and Opportunity have occasionally imaged clouds associated with the ACB, however, these observations are not documented in the literature and were only described at the American Geophysical Union Fall meeting in 2005 (Wolff et al. 2005). The Phoenix lander, however, produced an impressive atmospheric data set over the course of its 151 sol mission, which included a large number of cloud observation sequences using two separate pointings of the Surface Stereo Image (SSI) camera. The SSI used filter parings which allowed simultaneous capture of clouds at two wavelength bands. The two filtered images were then ratioed and compared to a radiative transfer model to determine whether the clouds were likely composed of dust or ice (Moores et al. 2010).

The MSL cloud observations make up the largest data set of cloud imaging form the surface in the history of Martian exploration, and its equatorial landing site has enabled observations of the ACB to be made from the surface. Zenith Movies and Supra-Horizon Movies have been acquired with a regular cadence since the beginning of the mission, and now consist of a data set containing over 500 observations over a two Martian year period. This thesis will report on all cloud observations, corresponding to a study period of $L_S = 160°$ of MY 31 to $L_S = 160°$ of MY 33. Chapter 3 will give an in-depth overview of the MSL cloud observations, including the analysis methods used. Before discussing these observations, however, a brief overview of the Mars Science Laboratory mission and the environment of its landing site will be given.

2.3 The Mars Science Laboratory Mission and the Environment of Gale Crater

The Mars Science Laboratory rover Curiosity (shown in figure 2.1a) landed on Mars on August 6th, 2012. The primary phase of its surface mission lasted a little over a Martian year, and ended on September 28, 2014. At the time of writing, the MSL mission is in its first extended phase, and has been on the surface of Mars for approximately two Martian years. The primary scientific objective of the mission, as established by the Mars Exploration

Program, is to quantitatively assess the habitability of Gale Crater and to determine whether this local environment of Mars is, or was in its past, suitable for microbial life to exist. This broad mission goal is further broken down into four objectives:

- "The first is to assess the biological potential of at least one target environment by determining the nature and inventory of organic carbon compounds, searching for the chemical building blocks of life, and identifying features that may record the actions of biologically relevant processes.

- The second objective is to characterize the geology of the landing region at all appropriate spatial scales by investigating the chemical, isotopic, and mineralogical composition of surface and near-surface materials, and interpreting the processes that have formed rocks and soils.

- The third objective is to investigate planetary processes of relevance to past habitability (including the role of water) by assessing the long timescale atmospheric evolution and determining the present state, distribution, and cycling of water and carbon dioxide.

- The fourth objective is to characterize the broad spectrum of surface radiation, including galactic cosmic radiation, solar proton events, and secondary neutrons." (*Science Goals*)

MSL's landing site, Gale Crater (4.5° S, 137.4° E), is a 155-km diameter impact crater that is situated on the hemispheric dichotomy. Gale was selected on the basis of its geologic environment, most notably the flat-lying strata that make up the crater's central mound, Aeolis Mons (informally called Mt. Sharp). These strata record evidence of past aqueous activity (most likely water), and are important for geologic study as each layer acts as a proxy for the environment in which it was formed, allowing information about the past Martian environment to be obtained. Additional evidence for the former presence of water at Gale is presented in the form of mineralogic and morphologic features observed from orbit, such as the presence of clay minerals and valley networks that are prominent in the local region (Grotzinger et al. 2012). The presence of water is a key driver for site selection, given its significance to our current understanding of habitability.

Curiosity is equipped with 10 primary scientific instruments, although the engineering cameras on board, such as the Navigation Camera and the Hazard Cameras, may also return valuable science information (Moore et al. 2016; Moores et al. 2015a; Moores et al. 2015b). As the research presented in this thesis is environmental in nature, the description of the scientific payload will be limited to instruments capable of acquiring environmental

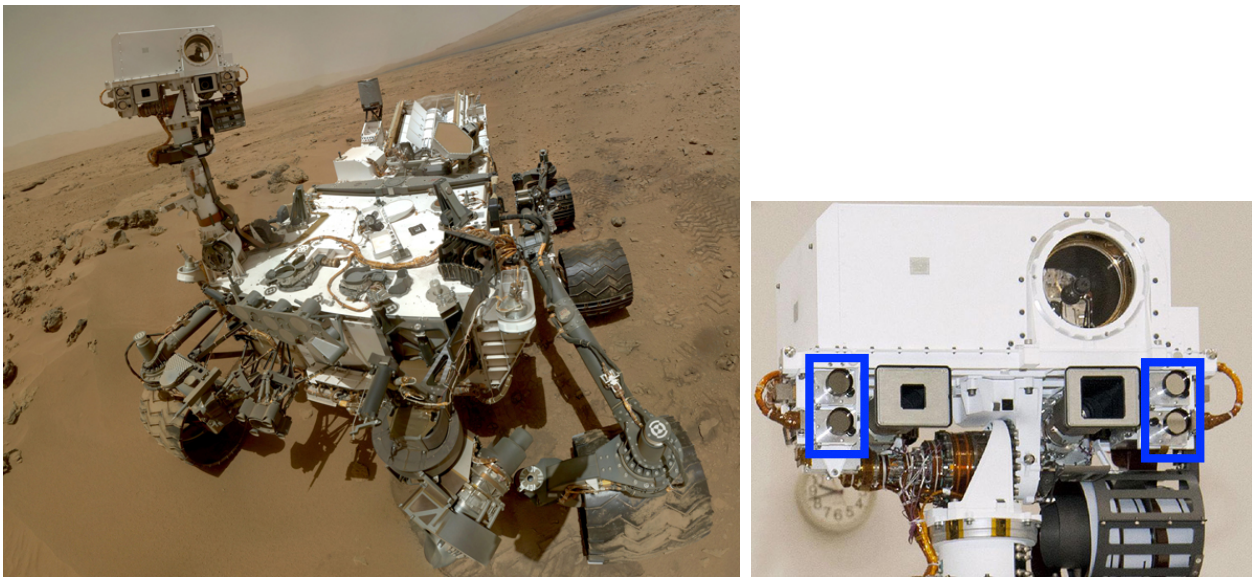

(a) (b)

Figure 2.1: (a) A composite self-portrait of the MSL rover Curiosity taken with the MArs Hand Lens Imager (MAHLI) on sols 84 and 85 of the mission. (b) A close up image of Curiosity's Remote Sensing Mast. The blue boxes highlight the position of the left and right pairs of the rover's Navigation Cameras.

measurements. Curiosity's primary environmental instrument is the Rover Environmental Monitoring Station (REMS) which monitors the air and ground temperature, wind speed and direction, UV radiation, air pressure, and relative humidity at a distance of 1.5 metres above the surface (Gómez-Elvira et al. 2012). While these measurements are useful for understanding local conditions near the surface, atmospheric imaging is used to augment the REMS data set by acquiring information about the atmospheric conditions away from the rover.

To monitor the dust levels in the atmosphere, atmospheric opacity measurements are routinely made from solar disc images using the rover's Mast Cameras (MastCam) (Lemmon 2014). Using the MastCam and NavCam, line-of-sight (LOS) extinction measurements are also routinely acquired to understand how the planetary boundary layer (PBL) mixes with the surrounding atmosphere (Moore et al. 2016). Finally, cloud observations are made using the rover NavCams (shown in figure 2.1b). These observations will be discussed at length in the following chapter.

Chapter 3

MSL: Data Set and Analysis Methods

3.1 Navigation Camera (NavCam)

Curiosity is equipped with 2 pairs of Navigation Cameras, 4 NavCams total, which are attached to the camera mounting plate on the Remote Sensing Mast. The NavCams are classified as engineering cameras, rather than science cameras, as their primary use is for traverse imaging and providing terrain context for other imagers on board the rover. Each pair of cameras use a broadband visible filter, and are spectrally responsive in the wavelength range of $600 - 850$ nm, with a Signal to Noise Ratio (SNR) of 200:1 for well-exposed images (Maki et al. 2012). The spectral responsivity for the NavCam is shown figure 3.1. Each camera has a sizeable $45 \times 45^{\circ}$ Field of View (FOV), which enables a relatively large portion of the sky to be monitored when compared with other cameras onboard the rover.

The detectors used in the NavCam are flight spare Charge Coupled Devices (CCDs) from the Mars Exploration Rovers, and consist of a 1024×1024 pixel photosensitive imaging region. Prior to downlink, the images are flat field and dark current corrected, as well as corrected for exposure time. The images are then binned in 2×2 pixels bins, which decreases the total data being downlinked while preserving the angular size of the imaged area. All MSL NavCam observations discussed in this thesis, save the Mt. Sharp + LOS observations between sols $594 - 910$, consist of a series of 512×512 pixel images. The bit depth of the camera is 12 bits/pixel, and thus each pixel can have a possible Digital Number (DN) between $0 - 4096$.

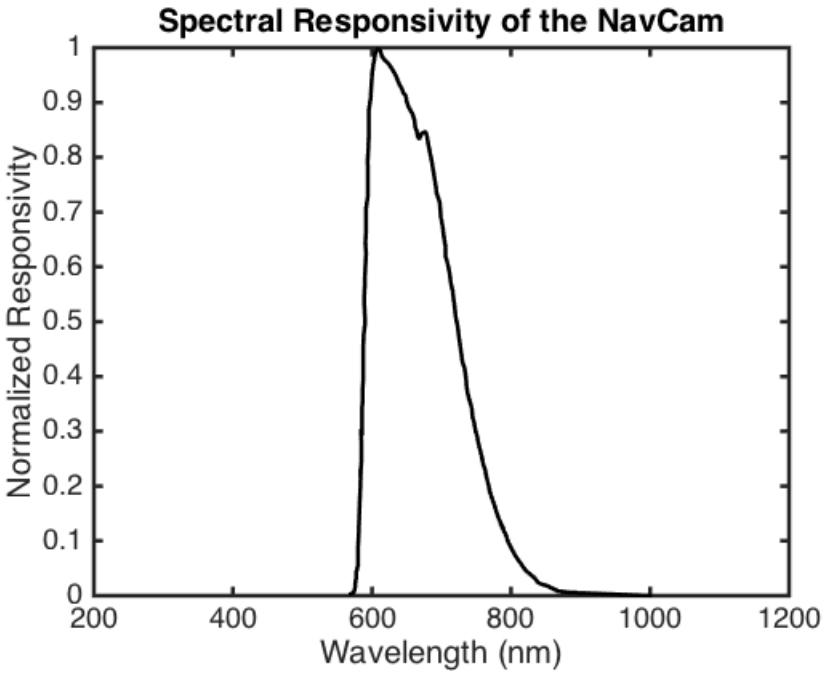

Figure 3.1: Spectral Responsivity of the Navigation Camera from Maki et al. (2012)

3.2 Zenith Movies (ZMs)

Each Zenith Movie observation consists of eight 512×512 pixel images captured using a near-vertical pointing of the NavCam (85° of elevation) such that the zenith point is captured within each frame. For observations acquired between sols $0 - 914$, the eight images are spaced approximately 13 seconds apart, and thus each movie is captured over approximately 91 seconds in time. On sol 915, a long span ZM observation was implemented due to analysis showing that a greater image spacing in time resulted in increased sensitivity for cloud detection (see section 4.7 for a detailed analysis). The long span ZM consisted of eight images spaced 38 seconds apart, and thus each movie is 266 seconds in length. In total, 233 ZMs have been acquired, with a movie being executed on average once every 3-4 sols.

The motivation for the vertical pointing of the ZM is that, by observing cloud motion, the upper level wind direction can be determined at a significant vertical distance from the rover. Long term analysis of upper level wind direction could shed light on the regional circulation patterns, and further augment the meteorological measurements made at the surface. However, the vertical pointing of the camera imposes a time restriction on the observation, which is also restricted by the rover's equatorial landing site and the large FOV of the NavCam. To prevent image saturation from the Sun, the observations are constrained from running within of 3 hours of local solar noon.

The specific timing of the movies depends on rover operations, however the vast majority

of ZMs are acquired in the late afternoon near 16:00 Local True Solar Time (LTST). Due to the implementation of semi-weekly science blocks reserved for environmental science activities during tactical mission planning, an increasing number of early morning ZMs have recently been acquired. The morning environmental science blocks were implemented in order to sample the early morning atmospheric conditions. A temporal distribution of the ZMs over the two year study period is shown in figure 3.2. Two solar conjunction events exist within the study period for which no data was acquired: $L_S = 295^\circ - 310^\circ$ of MY 31 and $L_S = 352^\circ - 7^\circ$ of MY 32/33.

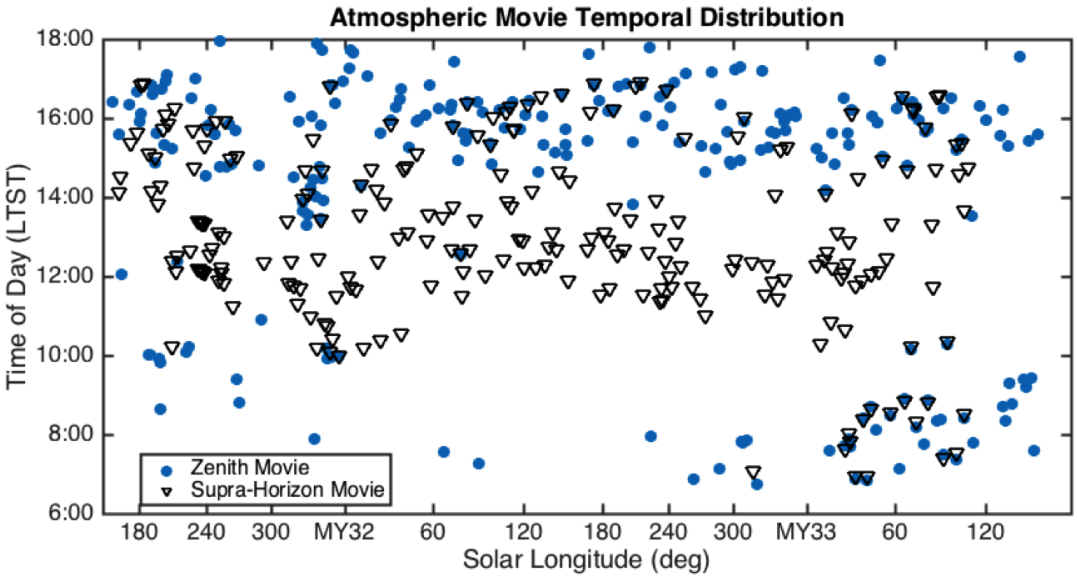

Figure 3.2: Temporal distribution of the Zenith and Supra-Horizon Movies from the beginning of the mission, up to sol 1352 ($L_S = 159^\circ$), spanning two Martian years.

As the path of the Sun on the sky changes throughout the year, the azimuthal pointing of the NavCam also changes to minimize image saturation. During autumn and winter when the Sun is in the northern sky, the NavCam azimuth is chosen as due south, centred around a local level coordinate of 180° in azimuth and 85° in elevation. As the Sun moves into the southern sky near $L_S = 180^\circ$, the pointing is changed to due north, 0° azimuth, and 85° elevation. Here, the local level coordinate system is based on a rover-derived geometry, where north is 0° and east is 90°.

The clouds observed at Gale Crater are extremely tenuous and typically cannot be observed in raw, unprocessed images. To enhance the visibility of the thin clouds, a mean frame subtraction technique is applied to each image sequence. This technique entails taking the eight sequence frames, and creating an average frame on a pixel-by-pixel basis. The average frame is then subtracted from each individual image (as raw data) to isolate the time-variable component, i.e. the cloud, thereby creating a perturbation movie. A compari-

son showing the unprocessed images and mean frame subtracted images for the sol 429 ZM is shown in figure 3.3a and 3.3b, respectively. Examining clouds in the mean frame subtracted sequences allows detail, that would otherwise be irretrievable, to be obtained, such as cloud morphology, spacing and opacity.

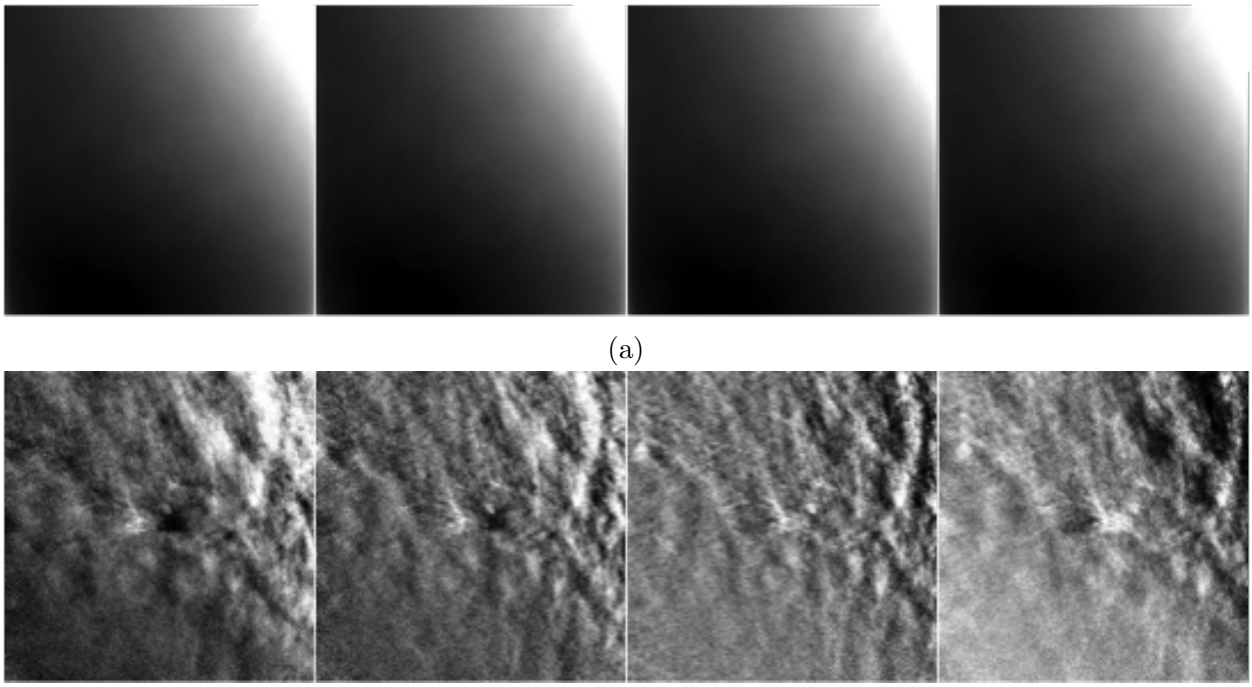

(a)

(b)

Figure 3.3: (a) Four raw frames from the sol 429 Zenith Movie showing the variation in spectral radiance across the frame. (b) The same four frames from the sol 429 ZM processed using the mean frame subtraction technique.

Mean frame subtraction is a suitable technique for the MSL sequences given that the background for each image is static, and therefore the difference between each image is due only to the movement of clouds between successive frames. Other processing methods, however, also exploit this fact, and can produce a similar output as mean frame subtraction. One such method involves subtracting successive frames on a pixel-by-pixel basis, without doing any additional analysis. This technique works on the same basic principle as mean frame subtraction, as the differenced image contains only information due to the clouds, given a static background. The drawback of this technique is that the output movie contains one less frame than if the sequence were processed using mean frame subtraction.

Subsequent to mean frame subtraction, the movies are analyzed by a human operator, and assigned a quality ranking based on the clarity and contrast of the cloud features relative to the background sky. This ranking scheme, shown in table 3.1, is subjective and is only used to determine which image sets are suitable for further analysis. The rankings for this

Table 3.1: Atmospheric movie visual quality ranking scheme. Note that all scores between -1 and 10 are used, however only a sampling is presented here.

Quality Ranking	Description
10	No mean frame subtraction necessary to see features
5	Clear features visible upon mean frame subtraction
1	Faint features visible upon mean frame subtraction
0	Featureless frame upon mean frame subtraction
-1	Unusable frame due to error or proximity to the sun

scheme extend from -1 to 10, where a ranking of -1 indicates an unusable frame, 0 indicates a featureless frame, and 10 indicates that clouds can be observed in unprocessed images. All scores between -1 and 10 are used, however only a sampling of the rankings and the associated descriptions are presented in table 3.1. All movies that receive a quality ranking of 1 or higher are subjected to further analysis to extract information on the opacity and spacing of the clouds that are apparent in the images. More information on the procedure for this analysis is presented in section 3.4. All analysis in this work is achieved using mean frame subtracted perturbation images only.

3.3 Supra-Horizon Movies (SHMs)

Supra-Horizon Movies (SHMs) make up a second data set with which to monitor the cloud activity above Gale Crater. Unlike the Zenith Movies which use a vertical pointing, SHMs use a lower elevation angle pointing of the NavCam, and capture a long path length through the atmosphere helping to interpret cloud morphology. The exact pointing used for this observation has changed over the course of the mission, with each change reflecting different scientific intent. At the beginning of the mission, SHMs consisted of eight 512×512 pixel images and captured a patch of sky directly above the peak of Mt. Sharp, centred around a local level coordinate of 134.8° in azimuth and 38.5° in elevation. The motivation for this pointing was twofold. First, similar cloud observations acquired by the Phoenix mission showed that the long path length through the low atmosphere made the observation more sensitive to low altitude clouds, and provided a better angle with which to observe cloud morphology. Secondly, Mt. Sharp rises 5.5 km above the crater floor, and thus constitutes a significant topographic feature. By observing the patch of sky directly above the mountain's peak, orographic condensation can potentially be observed.

On sol 594 ($L_S = 113°$), a new version of the SHM was implemented, that was intended to enhance the science return of the observation. The new observation utilized a different aspect ratio and pointing, such that each frame was 1024 pixels tall by 512 pixels wide, and

captured portions of the sky, mountain and foreground. This new pointing allowed the LOS extinction (Moores et al. 2015b) to be measured at a second pointing while simultaneously allowing for the detection of clouds above Mt. Sharp. Additionally, the parameters of the observation were also changed such that each movie consisted of only 4 frames spanning 39 seconds so that the data-volume for the observation was unchanged. The SHMs acquired during the sol $0 - 594$ period will hereby be referred to as "original Mt. Sharp" while those acquired during the sol $594 - 910$ period will be referred to as "Mt. Sharp + LOS". For simplicity, the term "Supra-Horizon Movie" will be used at times to simply refer to an observation that uses a lower elevation angle pointing of the NavCam, thus distinguishing it from the ZM. Thus, all Mt. Sharp movies are also considered Supra-Horizon Movies however the reverse is not true.

Later analysis of the Mt. Sharp + LOS observations showed that the decreased time span diminished the sensitivity of the observation. Although LOS measurements could still be obtained from these images, the decreased time span coupled with the mean frame subtraction did not prove to be useful for detecting clouds. Thus, on sol 911, a new observation, referred to as the long span Mt. Sharp movie, was implemented with eight 512×512 frames and a 266 second time span using a similar elevation and azimuthal pointing as the original Mt. Sharp movie. Due to the lack of orographic condensation observed within any of the Mt. Sharp activities, the pointing was later altered to point directly above the crater rim, centred around a local level coordinate of 0° in azimuth and 26.3° in elevation. This observation is referred to as the north-facing Supra-Horizon Movie, and uses eight frames captured over a time span of 266 seconds. As is done with the ZMs, the SHMs were also given a seasonal pointing in order to prevent image saturation and maximize image quality. Thus, when the Sun is in the northern part of the sky, a south-facing SHM is executed using eight frames and a 266 second time span. Table 3.2 is provided for the reader that notes the changes made to the pointing and time span of the observation over the two year study period.

Table 3.2: Supra-Horizon Movie reference table that documents the changes made to the observation over the course of the mission.

Sol Range	Pointing (AZ, EL)	Frame Number	Movie Span (s)	# of Movies Acquired	In-Text Reference
0-594	134.8°, 38.5°	8	91	119	original Mt. Sharp
594-910	125.1°, 10°	4	39	50	Mt. Sharp + LOS
911-1031	134.6°, 43.5°	8	266	13	long span Mt. Sharp
1032-1258	0°, 26.3°	8	266	55	north-facing SHM
1259-current	180°, 26.3°	8	266	35	south-facing SHM

The majority of the Mt. Sharp and SHM observations were acquired in the afternoon,

near 12:00 LTST. Due to the southeasterly pointing of the Mt. Sharp Movies, this observation was restricted to being executed after 10:00 LTST. This time restriction, however, was not imposed on the north and south facing SHMs, allowing early morning SHMs to be collected beginning on sol 1032 ($L_S = 6.89^\circ$ of MY 33). The temporal distribution of the SHMs over the study period is shown in figure 3.2. In total, 272 Mt. Sharp and SHM observations acquired with the relative number of each pointing given in table 3.2. As with the ZMs, the Mt. Sharp and SHMs that receive a quality ranking of 1 or higher are subjected to further analysis to obtain information on the cloud opacity and spacing.

3.4 Analysis Methods

3.4.1 Spectral Radiance Determinations

Spectral radiance is a radiometric quantity that possesses units of W/m^2/Sr/nm. This is equivalent to the total energy (J) per unit time (s) per unit area (m^2) per unit solid angle (Sterradian, abbreviated Sr) per unit wavelength interval (nm). Section 3.4.2 will document the physics of the high cloud and whole atmosphere methods, however, to measure the cloud opacity, the difference in spectral radiance between the cloud and sky must first be determined. This is achieved by individually examining a frame from each sequence and manually selecting a cloudy region and empty sky region from the mean frame subtracted image. The selected cloudy clear sky regions are averaged using a circle of a 5-pixel radius in order to get above the noise of the camera. Figure 3.4 shows an example of a radiance map from the fourth perturbation image of the sol 429 ZM, which shows clouds as the warmer colours and the empty sky as blue.

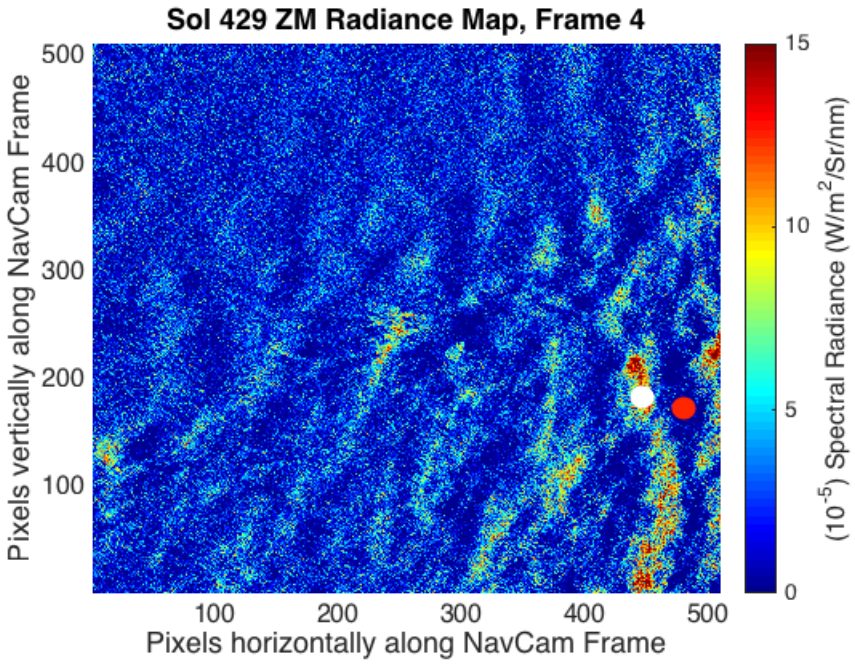

Figure 3.4: A spectral radiance map of the fourth frame from the sol 429 ZM processed using mean frame subtraction. To make an approximation of the cloud opacity, the variation in spectral radiance is measured between the cloud (white circle) and the sky (red circle). To get above the noise of the camera, the radiance value is measured using a circle of a 5 pixel radius. The size of the measured area shown here is exaggerated for clarity. Note that the scale of the colourbar is 10^{-5} W/m^2/Sr/nm.

3.4.2 Cloud Opacity

The values of opacity that will be reported depend on the interpretation of the clouds features that are apparent in the cloud movies. As mentioned previously, Moores et al. (2015a) and Kloos et al. (2016) compute the optical depth of the MSL clouds using two independently derived formulations, each making its own separate assumptions regarding the optical properties of the observed clouds. One possible interpretation of these clouds is that they result from alternating regions of a greater or lesser number of scattering centres, but otherwise have the same scattering properties as the bulk atmosphere. Moores et al. (2010) previously considered this situation and found that the small change in optical depth resulting in clouds, denoted as $\Delta\tau_{WA}$, could be described as:

$$\Delta\tau_{WA} = -ln\left[1 + a - \frac{a}{\exp(-\tau_{COL})}\right] \tag{3.1}$$

where τ_{COL} is the extinction optical depth of the average atmosphere and a is the proportional amplitude of the variation in spectral radiance resulting from these optical depth variations ($I_{\lambda,VAR}$) as compared to the average radiance in the frame, due to scattering from the entire atmosphere ($I_{\lambda,MEAN}$), i.e. $I_{\lambda,VAR} = aI_{\lambda,MEAN}$. This method, referred to as the Whole Atmosphere method and denoted with a subscription WA, has several advantages. As the average background spectral radiance is used, the phase function, single scattering albedo and illumination conditions do not need to be known a priori. Equation 3.1 was used successfully by Moores et al. (2010) to interpret the billowing dust and clouds observed at the Phoenix landing site. The observed clouds matched up well with data acquired by the Phoenix lidar (Whiteway et al. 2009; Dickinson et al. 2010; Komguem et al. 2013), and the morphology of the clouds observed also supported the conclusion that they were relatively low in altitude and intimately mixed within the planetary boundary layer.

However, for many of the clouds seen at Gale Crater, a better interpretation is that they are located at an altitude above the atmospheric scattering due to dust. As with Moores et al. (2015a), this interpretation is supported by the relatively small size of the clouds, their morphology as distinct cloud streets and observations taken at similar times from MCS and the Mars Color Imager (MARCI) which both observe high cloud, though it should be noted that neither instrument is optimized for the observation of thin, low altitude, PBL clouds such as those reported by Moores et al. (2010). To interpret the clouds seen in the MSL movies at Gale, an alternative model is used, which is referred to as the high cloud model. A derivation from first principles of this method will be provided here.

Following the derivation of Liou (1992), the equation of radiative transfer for a horizontal cloud in a scattering atmosphere (Eq. 3.1.1 from Liou, 1992) is:

$$\mu \frac{dI(\tau, \mu, \phi)}{d\tau} = I(\tau, \mu, \phi) - J(\tau, \mu, \phi) \tag{3.2}$$

Here, μ is the cosine of the viewing angle of the cloud, ϕ. The extinction optical depth of the atmosphere at the location where the radiance is changing is τ, I is the radiance at optical depth τ, and J is the source function at optical depth τ. This equation can be substantially simplified using the high cloud model.

Beginning with the source function, the cloud is assumed to be so thin that there is no multiple scattering within the cloud. Furthermore, it is assumed that the solar contribution to the cloud is much greater at the wavelengths of the NavCam than is reflection from the ground. Under these assumptions, the source term simplifies to:

$$J(\tau, \mu, \phi) = \frac{\overline{\omega}}{4\pi} F_{\lambda,0} P(\Theta) \exp(-\frac{\tau}{\mu_0}) \tag{3.3}$$

Here, $\overline{\omega}$ is the single scattering albedo, $F_{\lambda,0}$ is the solar flux at the cloud, P is the phase function, which depends on the scattering angle, Θ. Finally μ_0 is the cosine of the solar zenith angle. It will be assumed that the single scattering albedo is 1, typical of terrestrial clouds (e.g., Liou, 1992, Table 5.2) as well as Martian dust (Moores et al. 2015b) in the visible and near IR portion of the spectrum.

Next, it will be assumed that there is no radiance behind the cloud, due to the lack of scattering centres above the cloud, so $I = 0$ at the cloud in the direction of the observer. The implicit assumption here is that all radiance that is emitted towards the NavCam is generated by the source term within the cloud, i.e. through scattering of sunlight. If we further assume that the cloud is very thin and single scattering dominates, the source term generated is an integral equation in optical depth for the radiance, analogous to Eq. (3.4.11a) of Liou (2002):

$$I(\tau, \mu, \phi) = \int_0^{\Delta\tau} \frac{d\tau}{4\pi\mu} F_{\lambda,0} P(\Theta) \exp\left[-\tau(\frac{1}{\mu_0} + \frac{1}{\mu}) \right] \tag{3.4}$$

Equation 3.4 may be integrated to determine the radiance at the edge of the cloud closest to the NavCam and in the direction of the NavCam to produce:

$$I(\tau, \mu, \phi) = \frac{\mu_0}{4\pi(\mu + \mu_0)} F_{\lambda,0} P(\Theta) \left[1 - \exp\left[-\Delta\tau(\frac{1}{\mu_0} + \frac{1}{\mu}) \right] \right] \tag{3.5}$$

Note that the integrated optical depth of the cloud is described as $\Delta\tau$. As the cloud is assumed to be very thin, we can use the approximation that $1 - \exp(-x) \approx x$ for small values of x. This allows the equation to be simplified further to:

$$I(\tau, \mu, \phi) = \frac{\Delta\tau}{4\pi\mu} F_{\lambda,0} P(\Theta) \tag{3.6}$$

To extend this radiance down through the attenuating atmosphere in order to derive the observed radiance at the NavCam, we need to multiply this radiance, using Beer's Law, by $exp(-\tau_{COL})$ where τ_{COL} is the column extinction optical depth determined by the MastCam. As these values are obtained only approximately every 10 sols, they are interpolated for each of the cloud movies.

Furthermore, measurements obtained from the Planetary Data System for NavCam are in terms of spectral radiance, therefore it is necessary to multiply the values obtained from NavCam by the spectral band-pass, $\Delta\lambda$. To distinguish between the radiance added by the intervening atmosphere and the radiance from the cloud, the mean frame is removed yielding the time-variable signal only, which is due to clouds:

$$I_{\lambda,VAR}\Delta\lambda = \frac{\Delta\tau}{4\pi\mu} F_{\lambda,0} P(\Theta) \exp\left(- \frac{\tau_{COL}}{\mu} \right) \tag{3.7}$$

Rearranging this equation for the optical thickness of the cloud, $\Delta\tau$, yields:

$$\Delta\tau_{HC} = \frac{4\pi\mu I_{\lambda,VAR}\Delta\lambda}{P(\Theta) F_{\lambda,0} \exp(-\frac{\tau_{COL}}{\mu})} \tag{3.8}$$

Finally, a value must be assumed for the phase function for cloud particles. Liou (1992) and Chepfer et al. (2002) describe many different microphysical types of cloud particles. In the neighbourhood of scattering angles of 90°, which applies to nearly all cloud movie observations, values of the phase function average to approximately 1/15. This parameter will be examined in greater detail in section 4.6. The subscript "HC" stands for High Cloud, and is used to distinguish this method from the Whole Atmosphere approximation method previously discussed.

3.4.3 Frequency Domain Analysis

The majority of the cloud features observed in the Zenith and Supra-Horizon movies exhibit regular spacing, such as the sol 429 example shown in figure 3.4. To estimate the cloud spacing, the image sequences that rank 1 or higher on the quality ranking scheme are subjected to further analysis using a 2-dimensional Fast Fourier Transform. The remainder of this section will detail the FFT analysis of the cloud images, while the results will be reported in section 4.3.

A 1-dimensional Fourier Transform is a common technique used in signal processing in

which a time-varying signal is treated as a weighted combination of sinusoids with varying frequencies (ω), amplitudes (also referred to here as power) and phase shifts. The 2-dimensional Fourier Transform works in the same way, however instead of a 1-D input signal, the input is a 2-dimensional image within the spatial domain. As with the 1-D Fourier Transform, the information that makes up the 2-D input image is treated as a weighted combination of sinusoids, however the 2-D Fourier Transform allows the integral frequencies to vary in space, permitting information about their orientation to be obtained.

Simply put, the 2-D Fourier Transform looks for periodic variations of pixel intensity within the image, and expresses any detected variation as a summation of sinusoidal waves. The frequencies of the expressed waves are given in units of radians/pixel. The amplitude of the frequency is the pixel intensity, i.e. the greater the frequency's amplitude the higher the DN. As the summation of the constituent frequencies that make up the image cannot be expressed as a continuous function, a computational method known as a Discrete Fourier Transform is used. Rather than sampling the image at an infinite number of frequencies as can be achieved analytically, the Discrete Fourier Transform samples the image at a specific frequency interval which is determined by the size of the image. The algorithm used to compute the discrete Fourier Transform is known as a Fast Fourier Transform (FFT), which is used in this work.

The procedure begins with the selection of a single cloud image from the movie. The image is typically selected from the middle of the sequence (frames 3, 4, or 5), as these are typically free of the large brightness gradient that characterizes beginning and end sequence frames. The selected image is then multiplied by a Welch window (Welch 1967), which is a 3-dimensional gaussian function that is applied to minimize edge effects and diminish spectral leakage. An example of a selected sequence frame, and a frame with the Welch window applied is shown if figures 3.5a and 3.5b, respectively.

As the tenuous cloud features within the MSL movies can often be difficult to distinguish against the background noise within the perturbation images, the same FFT analysis is also applied to a frame consisting of random noise. The frame of random noise is generated based on the SNR of the NavCam. By quantitatively comparing the FFT output for the cloud image and the frame of random noise, the frequencies that make up the cloud image can be determined. An example of a random frame of noise and a frame of noise with the Welch window applied is shown in figure 3.5c and 3.5d, respectively.

Following the application of the Welch window, the spatial information within the image is transformed into the frequency domain using an FFT native to Matlab. The output of the FFT is a 512×512 pixel image containing information about the frequencies and their corresponding magnitude (or power) that make up the image. The frequency is represented

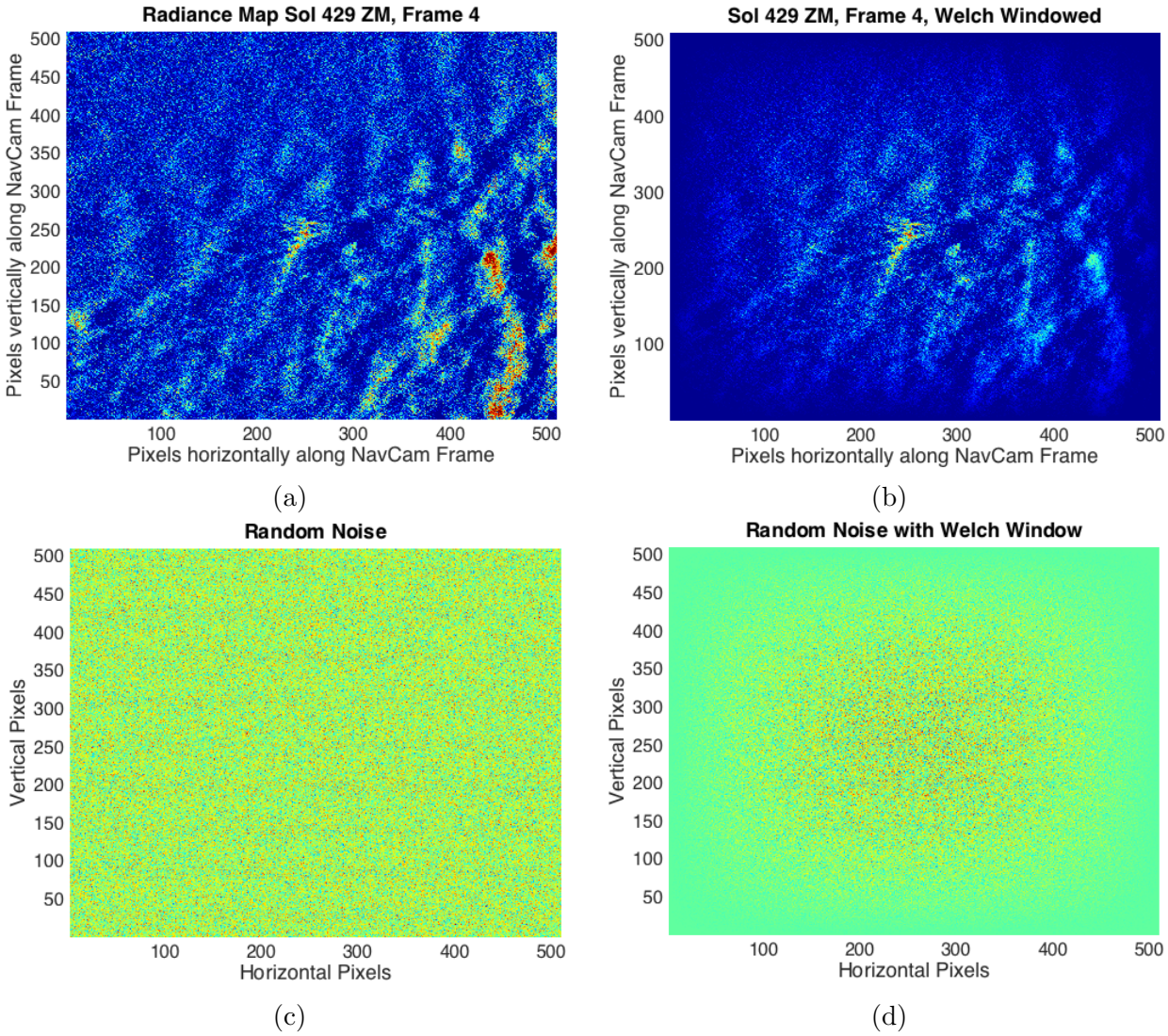

Figure 3.5: (a) The fourth frame from the mean frame subtracted sol 429 ZM sequence. (b) The fourth frame from the sol 429 sequence after the application of a Welch Window. (c) A frame of random noise based on the signal to noise ratio of the NavCam (200:1). (d) A frame of random noise subsequent to the application of a Welch Window.

by the location relative to the axis of the image, as demonstrated in figure 3.6a, while the power of the frequency is represented by the pixel brightness. An easier way to interpret the FFT output is to shift the quadrants about the (0,0) point, which is shown in figure 3.6b. In figure 3.6b, the low frequencies are observed near the origin, while increasing radial distance from the origin moves towards higher frequencies in the respective horizontal and vertical directions.

In addition to horizontal and vertical frequency information, the output images also contain information about the orientation of the clouds by their position relative to the x and y axis. Because the cloud orientation is irrelevant for this analysis, the vertical and horizontal frequency information is not used specifically, and quadrants are co-added. The result of this is a 256×256 pixel image containing the power and frequency information for the selected cloud sequence image. To quantitatively assess the frequency and power information, the image is averaged using concentric circles over the entire image. The average power spectrum for the sol 429 ZM is compared to a synthetic noise frame in figure 3.7a.

The frequency with the greatest power compared to a synthetic frame of random noise is considered to be the frequency that is representative of the spacing of cloud features. This is referred to as the characteristic frequency, denoted as ω_{CHAR}, and is expressed in units of radians/pixel. ω_{CHAR} is obtained by subtracting the synthetic noise average spectrum from the average cloud image specrum, and extracting the maximum value. An example of the output for the ratioed curves is given in figure 3.7b, which shows that the frequency range for which the sol 429 ZM and synthetic noise frame differ lies between $0.05 - 0.7$ radians/pixel, peaking at 0.2 radians/pixel. Thus, the peak frequency is selected as ω_{CHAR}, and is converted to a wavelength using $\omega_{CHAR} = 2\pi f = 2\pi\lambda_{CHAR}^{-1}$, where λ_{CHAR} is the characteristic wavelength in pixel distance that contributes the excess power of the cloud image. A better way to represent the characteristic spacing is to use the angle that the spacing subtends within the camera frame, and is converted to an angle using a conversion factor of 0.0879° per pixel, given that there are 512 pixels that cover 45° of FOV.

As will be seen further on, a number of the MSL cloud sequence images contain artifacts that arise from the optical assembly of the Navigation camera. These artifacts can be clearly seen in the sol 1138 ZMs and the 1211 ZMs shown in figure 4.2. These artifacts are defined by sharp boundaries, and are present within each sequence image. When cloud images contain camera artifacts, the FFT analysis described above will pick up the sharp boundaries, producing erroneous results that are not representative of the cloud spacing. To mitigate this, cloud images were cropped to remove the camera artifacts, and the FFT analysis was performed on the cropped images.

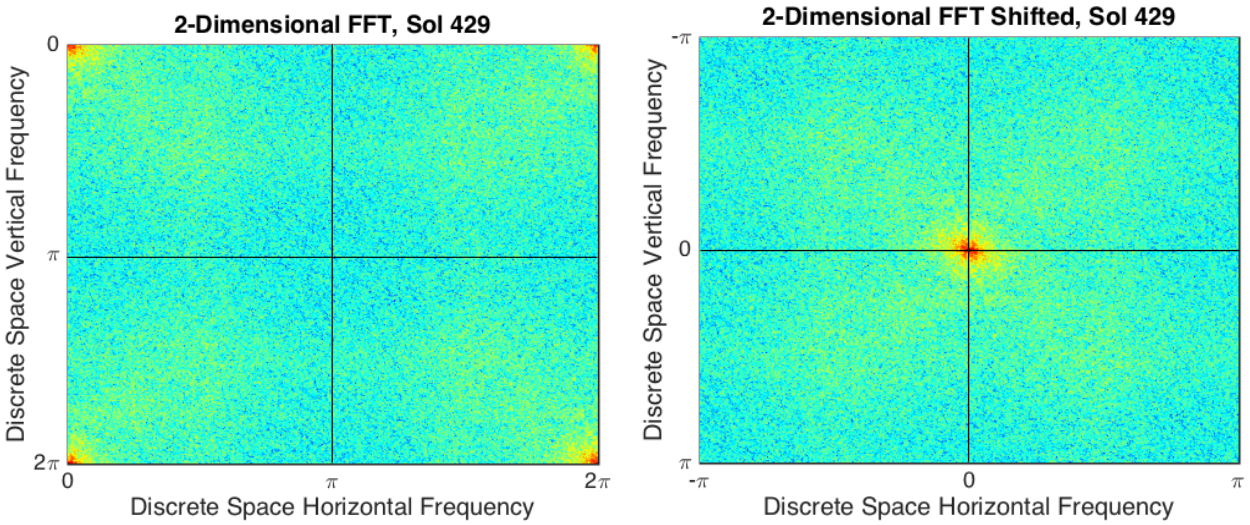

(a) (b)

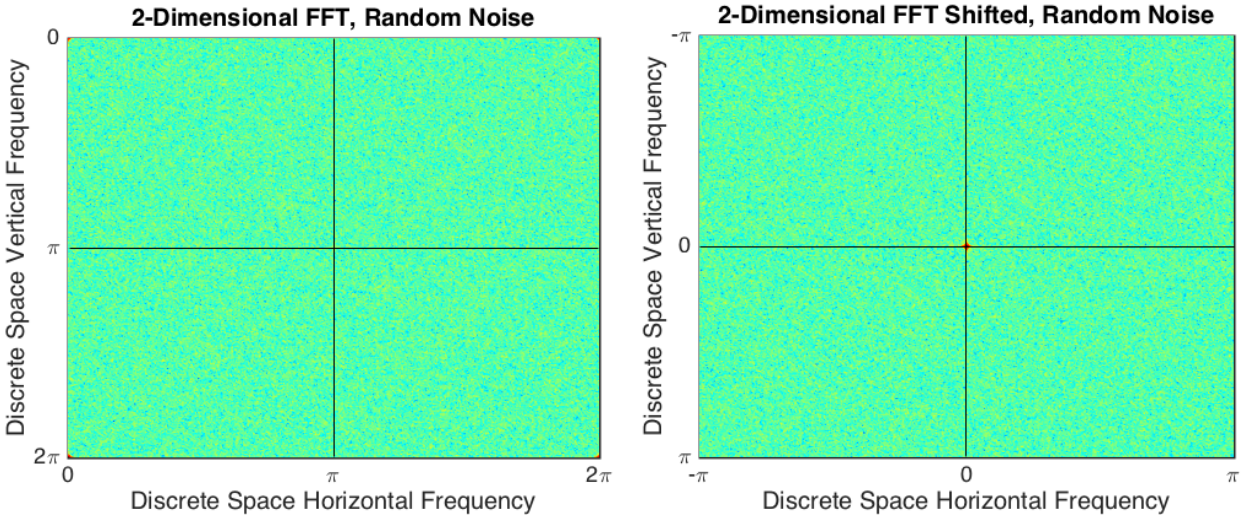

(c) (d)

Figure 3.6: (a) Output of a 2-Dimensional FFT for the fourth frame of the sol 429 ZM. The location relative to the x and y axis of the image indicate the frequency, while the amplitude of the frequency is given by the colour scheme of the image, with warm colours representing high amplitude frequencies, and cooler colours indicating lower amplitude frequencies. (b) FFT output data shifted about about the (0,0) point of horizontal and vertical frequencies. (c) Output of a 2-Dimensional FFT applied to a frame of random noise. (d) FFT output of the frame of random noise shifted about (0,0).

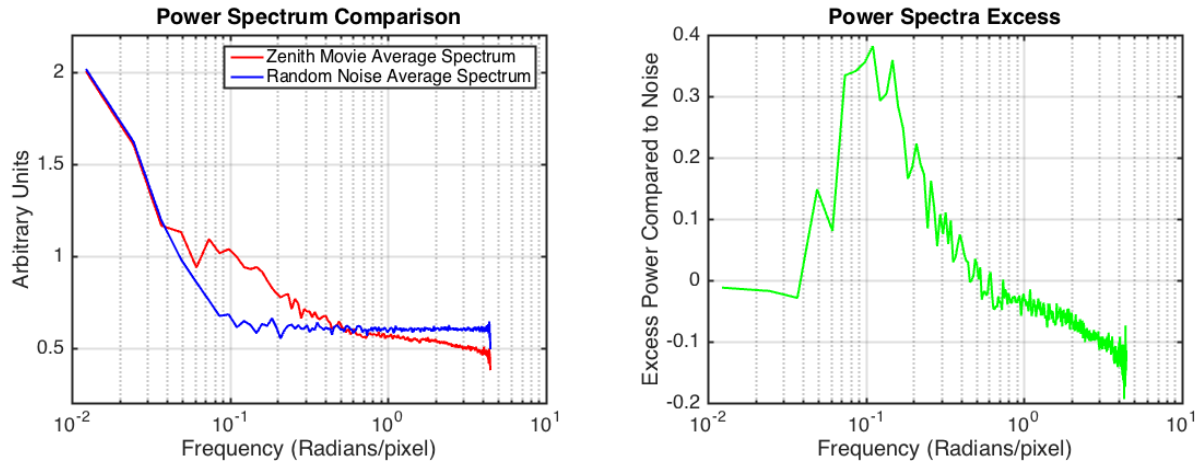

(a) (b)

Figure 3.7: (a) Power spectrum comparison for the sol 429 ZM and a synthetic frame of random noise based on the SNR of the NavCam. (b) The excess power spectrum of the sol 429 cloud sequence image compared to that of a frame of random noise.

Chapter 4

MSL: Results and Analysis

4.1 Seasonality and Noteworthy Movies

4.1.1 Zenith Movies

Over the two year study period, there are distinct periods of increased cloud formation as seen within the ZM data set. In MY 32, and for the data available in MY 31 and 33, clouds are more frequently observed between $L_S = 0^\circ - 180^\circ$, corresponding to autumn and winter in the southern hemisphere. Moores et al. (2015a) reported on observations between sols $0-360$, and found movies acquired up to sol 60 ($L_S = 184^\circ$) showed visible clouds after mean frame subtraction, and movies outside of this time period were largely featureless. During the sol $0-60$ period, 6 of the 7 movies acquired contained visible clouds, with the excepted movie (sol 27) being unusable as it was captured too close to local solar noon.

The sol 49 ZM shows the most opaque clouds detected during the sol $0-60$ period, ranking 10 on the quality scheme, indicating that clouds are faintly visible in the unprocessed images. Figure 4.1a presents 6 perturbation images from this sequence, in which small, discrete, and evenly spaced clouds ($\lambda_{CHAR} = 2.7^\circ$) can be observed rigidly translating across the frame in a direction approximately 135° E of N. It should be noted that the sol 49 ZM is not necessarily characteristic of cloud morphology or cloud opacity during the sol $0-60$ time period, and rather is what can now be classified as an example of infrequent detection of more opaque condensate clouds.

During $L_S = 184^\circ - 3^\circ$ of MY 31/32, the majority of movies were largely featureless, as only 23 of the 63 acquired movies contained visible clouds after mean frame subtraction. The 23 movies that detected clouds were not grouped together in time and showed no associated seasonal pattern. In spite of this, a single noteworthy ZM was captured on sol 193, which is shown in figure 4.1b. When juxtaposed against the sol 49 ZM, the clouds of the sol 193 ZM

have a larger angular size, in addition to a larger characteristic wavelength of $\lambda_{CHAR} = 11°$. The increased angular size could indicate low altitude water-ice clouds, given that the clouds appear to rigidly translate across each frame. This, however, is conjecture, as the cloud altitude cannot be ascertained from the NavCam images.

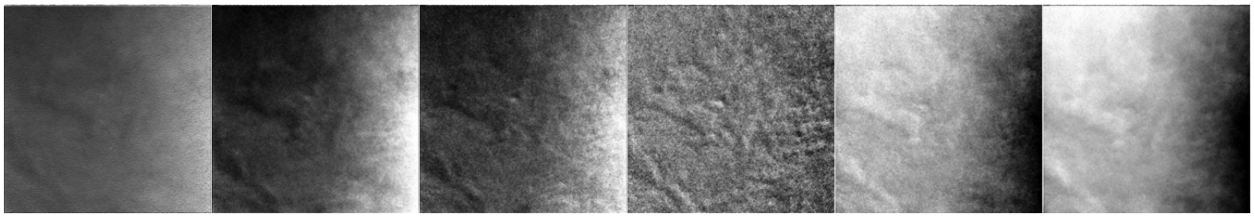

(a) Sol 49 ZM

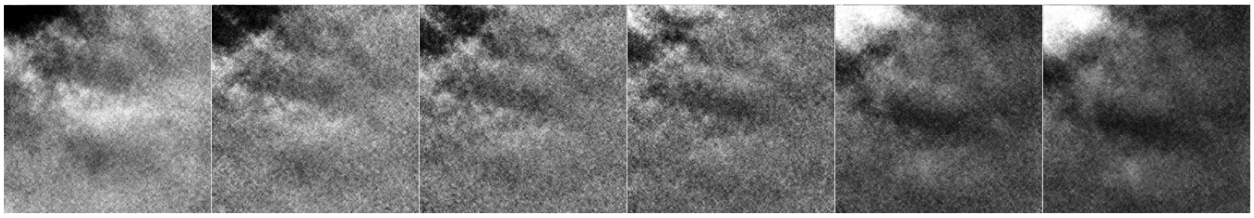

(b) Sol 193 ZM

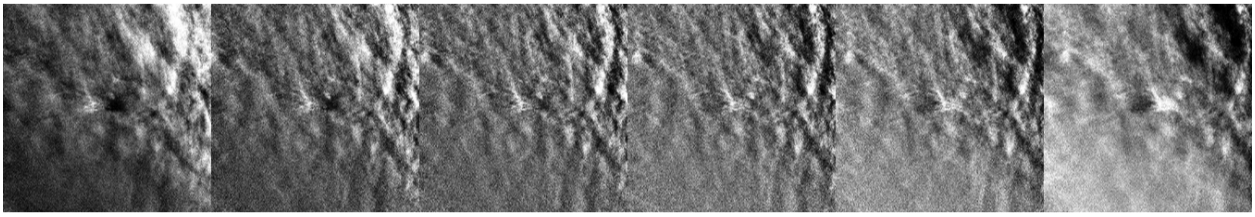

(c) Sol 429 ZM

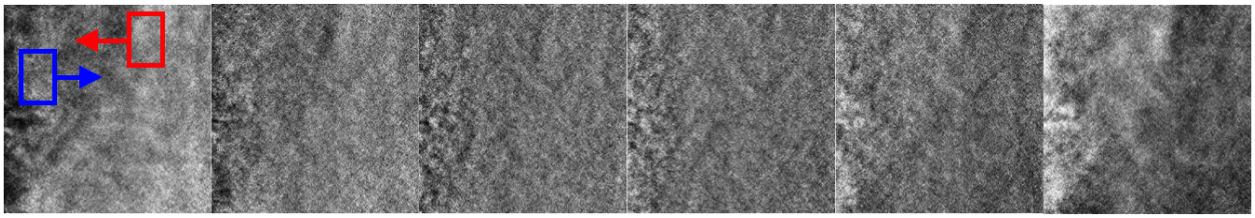

(d) Sol 543 ZM

Figure 4.1: Notable ZMs from MY 31 and 32: (a) 6 perturbation images from the sol 49 ZM showing small, discrete clouds. (b) Sol 193 ZM, showing large cloud features with a characteristic wavelength of $\lambda_{CHAR} = 11°$, which could indicate low altitude clouds. (c) Sol 429 ZM showing relatively opaque clouds moving from left to right, indicating an eastward motion. (d) Sol 543 ZM showing clouds moving in opposing directions, indicating wind shear. Clouds within the blue box can be observed moving from west to east while clouds within the red box are observed moving from east to west.

At the beginning of MY 32, as the atmospheric temperature begins to drop, a slow transition to cloudier conditions occurs. The onset of the increased cloud formation, as seen within the ZMs, begins at $L_S = 3°$ and persists through to $L_S = 170°$. Throughout this

time period, 43 of the 47 movies collected showed visible clouds upon examination with quality rankings between 1 and 10 on the subjective quality ranking scheme. Subsequent to $L_S = 170°$, the majority of movies are featureless through to the end of MY 32. The notable ZMs from MY 32 are shown in figure 4.1.

Cloud activity begins to pick up again at the onset of MY 33 near $L_S = 0°$ when seasonal atmospheric temperatures begin to decline. The transition, as in MY 32, begins slowly. The first half of the autumn season can be characterized by equal numbers of quality 0, 1 and 2 ZMs, with sol 1338 ($L_S = 56.7°$, shown in figure 4.2a) being a notable exception. A more consistent period of cloud formation begins as Mars reaches aphelion at $L_S = 71°$, as 15 of the 32 usable movies collected between $L_S = 71° - 160°$, were ranked ranked a quality 3 or higher.

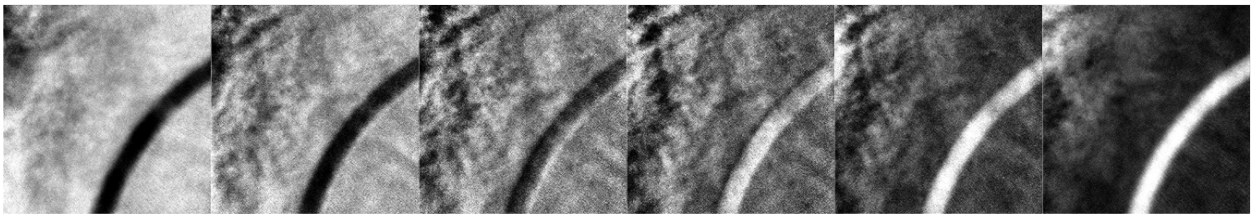

(a) Sol 1138 ZM

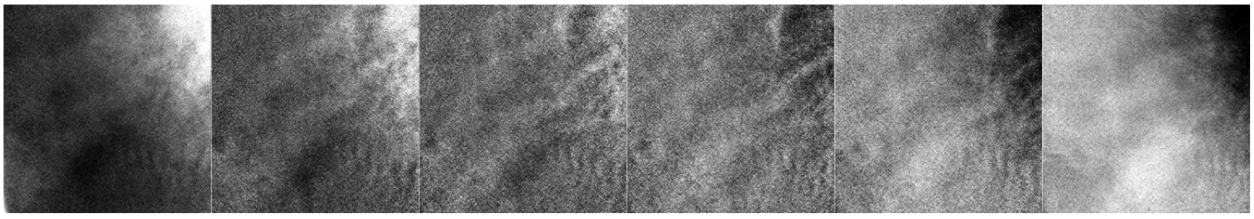

(b) Sol 1181 ZM

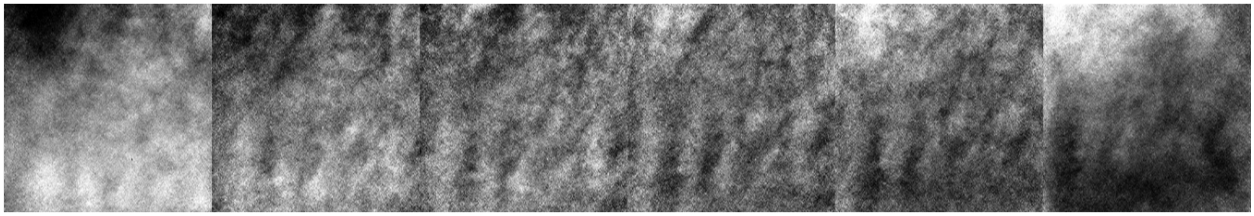

(c) Sol 1216 ZM

Figure 4.2: Notable ZMs from MY 33: (a) 6 perturbation images from the sol 1138 ZM showing clouds with high contrast against the background, as well as an image artifact from the camera lens. (b) Sol 1181 ZM in which thin, evenly spaced ripples are visible in the lower righthand side of the frame. The ripples seen in this sequence are characteristic of gravity waves, discussed in section 4.5. (c) Sol 1216 ZM in which evenly spaced clouds, similar to those in (b), although subtending a larger angle in the frame.

Seasonal activity related in terms of quality ranking is presented to convey the time periods of increased cloud activity, however the subjective nature of the quality ranking

scheme does provide a meaningful measure of the meteorological conditions of the regional environment. A more precise way to quantitatively assess the seasonality of clouds is to examine the ratio of the variation in spectral radiance between the cloud and the sky and the mean radiance for the entire frame ($I_{\lambda,VAR}/I_{\lambda,MEAN}$). Figure 4.3a plots these values for both the ZMs and the SHMs for the entire study period. Although the values are low, ranging between 0 and 0.025, a clear seasonal trend is observed. $I_{\lambda,VAR}/I_{\lambda,MEAN}$ is greatest between $L_S = 60^\circ - 180^\circ$ in MY 32, and $L_S = 60^\circ - 160^\circ$ of MY 33. This period of increased cloud activity occurs when the temperatures in the southern hemisphere are lower, as is shown by the REMS air temperature data in figure 4.3b. This data is provided simply to compare the seasonality of cloud detection with seasonal temperatures in the southern hemisphere, and is not used to indicate the temperature at which the clouds are forming.

For many of the ZMs, particularly those that rank lower on the quality ranking scheme (1 or 2), the cloud features do not exhibit conclusive morphologic expression that could implicate them as water-ice. Despite this, arguments of composition can be made by comparing the ZM seasonal cloud activity against other long-term orbital observations of equatorial clouds. The Mars Color Imager (MARCI), monitors the global weather of Mars and produces weekly report of the geographic and temporal distribution of condensate clouds and dust storm activity. The reports are particularly useful as they specifically give an account of the cloud and dust activity near the landing sites of the two operational landed spacecraft: Opportunity and MSL, both of which are located equatorially.

All MARCI weather reports were reviewed between $L_S = 160^\circ$ of MY 31 to $L_S = 160^\circ$ of MY 33, with specific attention given to condensate clouds near the MSL landing site and at equatorial latitudes. With the exception of a few cloud sightings near MSL towards the beginning of the mission (Moores et al. 2015a), the MARCI reports contain virtually no direct sightings of clouds over Gale Crater. MARCI weather reports, however, do contain frequent sightings of condensate water-ice clouds associated with the ACB at equatorial latitudes between $L_S = 10^\circ - 172^\circ$ of MY 32 (Malin et al. 2013; Malin et al. 2014b) and $L_S = 42^\circ - 146^\circ$ of MY 33 (Malin et al. 2015; Malin et al. 2016).

The appearance of the ACB, as documented by MARCI, is in agreement with the periods of increased cloud activity evident in the ZMs. This agreement suggests a water-ice composition for the MSL clouds during the aphelion season when the ACB is regularly overhead (as documented by MARCI in the time periods listed above). While it does indicate that the MSL clouds are likely water-ice during the aphelion season, the seasonality does not necessarily indicate a preference for composition outside of the aphelion season.

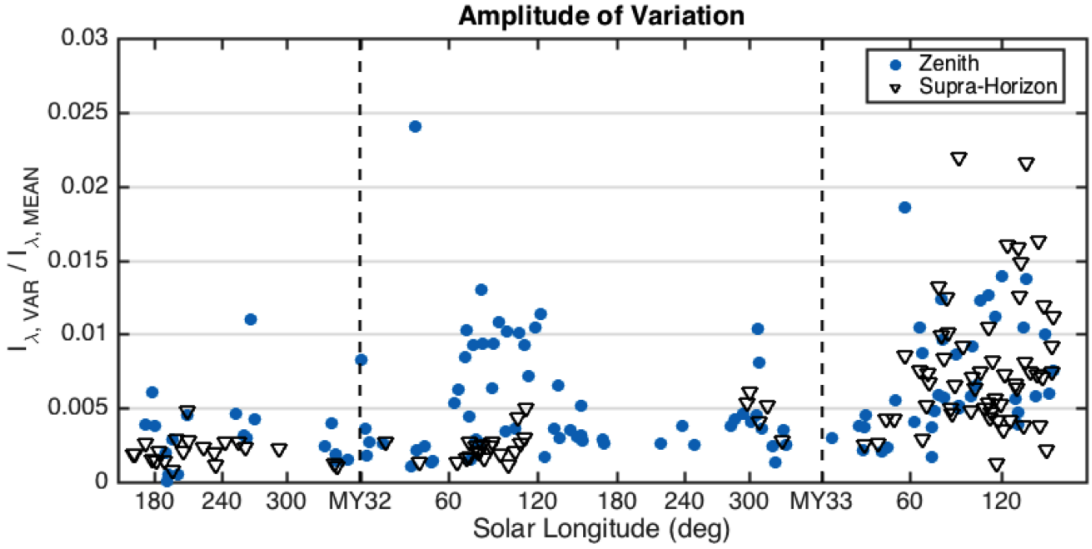

(a)

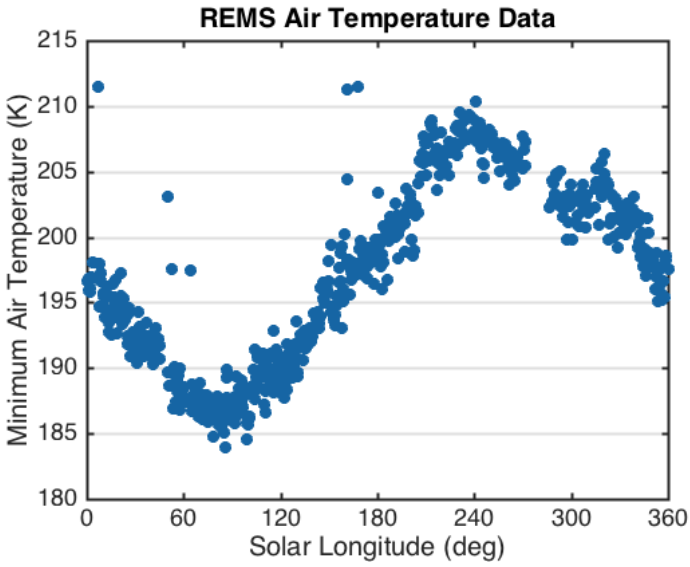

(b)

Figure 4.3: (a) Amplitude of variation of the ZMs and SHMs for the study period. (b) Minimum air temperature within Gale Crater as measured by the REMS instrument for the first Martian year of operations. As the temperature is repeatable from year to year, only a single MY is provided.

4.1.2 Supra-Horizon Movies

The clarity and contrast of cloud features observed within the SHMs are generally diminished when compared to the ZMs, with the exception of all south-facing SHMs and a few of the north-facing SHMs. Few of the Mt. Sharp movies, which were acquired between sols 0 and 1031, show discernible clouds after mean frame subtraction. Even when clouds are observed, they exhibit low contrast with the background sky, and often appear indistinct in shape and size, with many of the movies prior to sol 60 being excepted. The relatively low contrast observed in the SHMs is likely a result of the longer line of sight through the atmosphere due to the lower elevation angle of the NavCam. This suggests that these clouds are located at high altitudes, as the bulk of the atmosphere must be between the rover and the clouds for this effect to manifest. This effect is so pronounced when considering the 45° FOV of the NavCam, clouds are more often observed in the upper parts of the frame of the Mt. Sharp Movies and SHMs. This effect can be easily seen in the sol 1258 and sol 1138 south-facing SHMs shown in figures 4.4a and 4.4c, respectively.

Despite the diminished quality, seasonality is still observed when the data set is examined over the study period. In MY 31, increased cloud activity is observed between $L_S = 160^\circ - 184^\circ$, as all 6 of the acquired movies during this short time period show clouds that exhibit relatively good contrast with the background sky subsequent to mean frame subtraction. Like the trend observed in the ZMs during MY 31, a long stretch of featureless movies follows, with clouds only periodically observed during the southern spring and summer when the relatively high atmospheric temperatures diminish saturation probability. In MY 32, however, the onset of increased cloud detection occurs much later in the season compared to the ZMs, with cloud detection slowly starting to pick up in the SHMs near $L_S = 72^\circ$, and persisting through to $L_S = 108^\circ$. The disparity in the seasonal detection between the ZMs and SHMs likely reflects the relative sensitivity of the observations, which is even more likely given that the increased period of detection in MY 32 for the SHMs corresponds to the time of year when the ACB is known to be at be at its peak thickness (Clancy et al. 1996; Wolff et al. 1999). During $L_S = 72^\circ - 108^\circ$ of MY 32, 14 of the 16 acquired original Mt. Sharp movies obtained showed visible clouds in the mean frame subtracted sequences.

The Mt. Sharp + LOS observations implemented between $L_S = 108^\circ - 298^\circ$ did not prove useful for detecting the thin clouds that are typically observed above Gale Crater, as clouds were not visible in any of these observations. Given that clouds were regularly detected in the ZMs during this time period, the most likely explanation for this is that the shortened time span, which was half of the original Mt. Sharp Movie, inhibited the ability of the observation to resolve the tenuous clouds. As will be discussed below in section 4.7, there is a strong correlation between the visibility of the clouds and the distance that they

translate across the frame throughout the time span the movies are acquired. This indicates that when clouds are moving in a direction towards or away from the camera, the imaged translation is foreshortened. This has the undesired effect of decreasing the sensitivity of the observation. This finding explains the disagreement between the ZM and SHM data sets, and further implies that the seasonality of clouds within the SHM data set for MY 32 is not representative of the seasonal cloud activity.

The long span Mt. Sharp movies were implemented as a remedy to the featureless Mt. Sharp + LOS observations, and were executed between sols 911-1031 ($L_S = 299^\circ - 6^\circ$ of MY 32/33). The lengthened time span did increase the sensitivity, as 6 of the 14 observations ranked 1 or higher on the quality ranking, however the low quality of the observations and the inconsistent detection suggest a lull in cloud formation during this time of year. Seasonal cloud activity as seen in the long span Mt. Sharp movies is consistent with the ZMs for the $L_S = 299^\circ - 6^\circ$ period, suggesting that the lengthened time span improved the sensitivity of the observation, and that the observations were at a comparable sensitivity. In MY 33, cloud activity in the north and south-facing SHMs is consistent with MY 32, as activity begins to slowly pick up near $L_S = 55^\circ$ and persists through to the end of the study period. The majority of SHMs during this period capture visible clouds, with two of the observations (sols 1292 and 1302) even showing clouds in unprocessed images. Five of the noteworthy SHMs are shown in figure 4.4.

As seen in the examples provided in figure 4.4, the low elevation angle pointing of the camera offers a unique perspective with which to observe clouds. A particularly striking example is the sol 1302 south-facing SHM shown in figure 4.4b. The straight, parallel rows of clouds towards the bottom of the frame rigidly translate in a direction towards the rover. This cloud formation is characteristic of gravity waves and will be discussed in section 4.5.

4.2 Cloud Opacity

Opacity measurements are made for all movies, quality 1 or higher, using the high cloud and whole atmosphere approximation methods. Although both methods are implemented for each observation, one method is preferred based on the presence of clouds from orbital data. When high altitude water-ice clouds are observed equatorially from MARCI, the MSL clouds are assumed to be water-ice, indicating that the high cloud method is appropriate for measuring the opacity. The assumption of water-ice is supported by the agreement in cloud seasonality between MARCI and MSL and water-ice profiles from MCS also detect high altitude clouds near Gale Crater during the aphelion season (discussed in section 4.6). Outside of the aphelion season, cloud formation is inconsistently observed from MSL, and

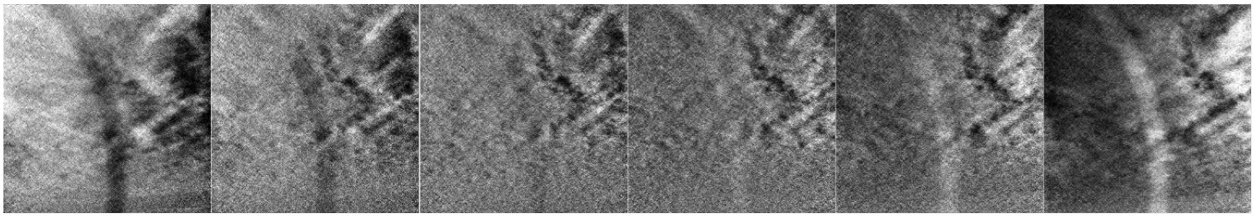

(a) Sol 1258 south-facing SHM

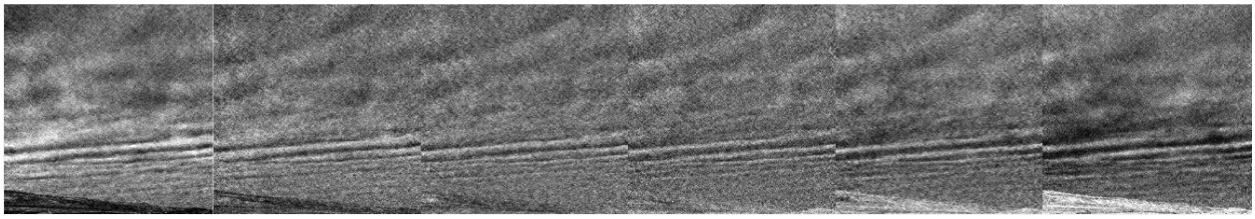

(b) Sol 1302 south-facing SHM

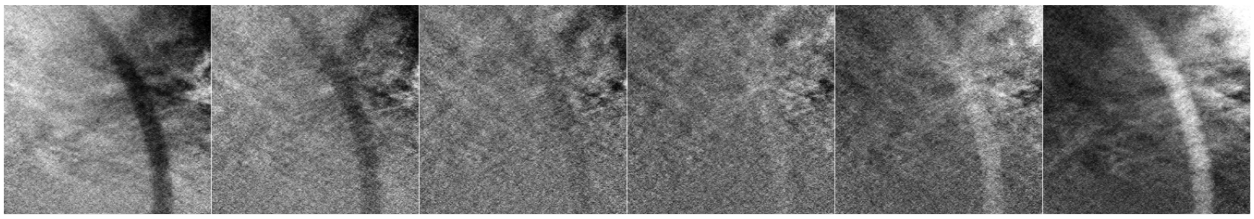

(c) Sol 1138 south-facing SHM

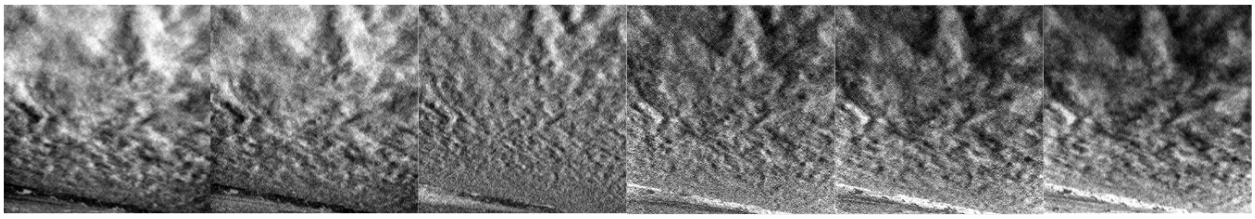

(d) Sol 1292 south-facing SHM

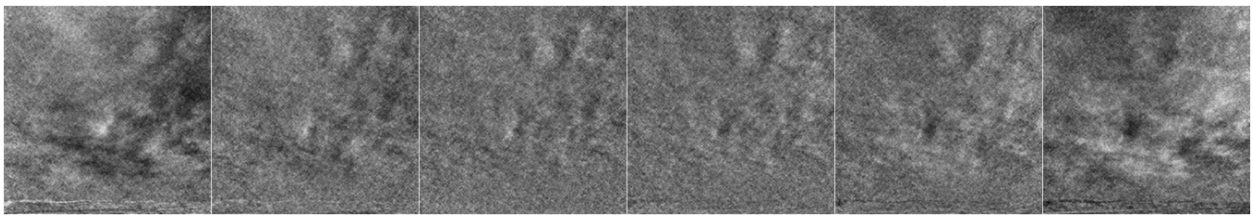

(e) Sol 1338 south-facing SHM

Figure 4.4: Noteworthy SHM observations from MY 33. (a) Six perturbation images from the sol 1258 south-facing SHM showing clouds most prominently in the upper parts of the frame. (b) Sol 1302 south-facing SHM in which straight, evenly-spaced rows of cloud formation are observed translating towards the rover. This formation is consistent with gravity waves. (c) Sol 1138 south-facing SHM showing tenuous clouds as well as a camera artifact. (d) Sol 1292 south-facing SHM in which prominent clouds can be observed in all parts of the frame. (e) Sol 1338 south-facing SHM. In this movie, a portion of the foreground was captured which can be seen at the bottom of the frame.

when clouds are observed, they are often difficult to distinguish against the background, and lack morphologic expression. MARCI weather reports do not show the presence of equatorial clouds, and thus it can be assumed that the cloud features present are dust aerosols aloft. For these periods, the whole atmosphere method is preferred. A summary of the the time period and preferred opacity is given as table 4.1.

The results of $\Delta\tau_{HC}$ and $\Delta\tau_{WA}$ are plotted as a function of season in the upper and middle panels of figure 4.5, respectively. Note that the scale of the y-axis is different for each subplot. The high cloud opacity exceeds the whole atmosphere opacity by a factor of 8.5, on average, which can be attributed to the different assumptions implicit in each of the equations. The seasonality can be observed by examining the relative number of data points over the study period. For example, between $L_S = 60^\circ - 120^\circ$ of MY 32 and 33, there are relatively more data points from the ZMs and SHMs, suggesting more cloud formation at this time of year. This period correlates with the peak in optical thickness as seen by Clancy et al. (1996) and Wolff et al. (1999).

Table 4.1: Mean preferred optical depth for the ZMs and SHMs with the corresponding L_S range. The L_S range for which $\Delta\tau_{HC}$ is preferred corresponds to the periods when high-altitude water-ice clouds are observed from MARCI. Outside of these periods, $\Delta\tau_{WA}$ is preferred.

L_S Range	Mars Year	Mean Preferred Optical Depth (ZMs)	Mean Preferred Optical Depth (SHMs)
$160^\circ - 195^\circ$	31	$\Delta\tau_{HC} = 0.038$	$\Delta\tau_{HC} = 0.035$
$208^\circ - 9^\circ$	31/32	$\Delta\tau_{WA} = 0.006$	$\Delta\tau_{WA} = 0.006$
$10^\circ - 172^\circ$	32	$\Delta\tau_{HC} = 0.031$	$\Delta\tau_{HC} = 0.012$
$173^\circ - 42^\circ$	32/33	$\Delta\tau_{WA} = 0.005$	$\Delta\tau_{WA} = 0.004$
$42^\circ - 146^\circ$	33	$\Delta\tau_{HC} = 0.043$	$\Delta\tau_{HC} = 0.048$
$147^\circ - 160^\circ$	33	$\Delta\tau_{WA} = 0.008$	$\Delta\tau_{WA} = 0.007$

Because of the seasonal presence of water-ice clouds observed from orbit, it is appropriate to discuss the opacity results for the study period with respect to the preferred approximation method. The average cloud opacity, calculated using the preferred method, is given for the ZMs and SHMs in table 4.1, while the entire data set is plotted as a function of season in the lower panel of figure 4.5.

When the ACB is overhead in MY 31, as documented by MARCI, the average high cloud optical depth is $\Delta\tau_{HC} = 0.038$ for the ZMs and $\Delta\tau_{HC} = 0.035$ for the SHMs. For the aphelion season in MY 32, the average cloud opacity is slightly decreased, while in MY 33, there is an increase in the average cloud opacity, as $\Delta\tau_{HC} = 0.043$ for the ZMs and $\Delta\tau_{HC} = 0.048$ for the SHMs. Clancy et al. (1996), Wolff et al. (1999), and Madeleine et al. (2012) found opacities for the ACB to range from $0.2 - 0.6$, however they also noticed that

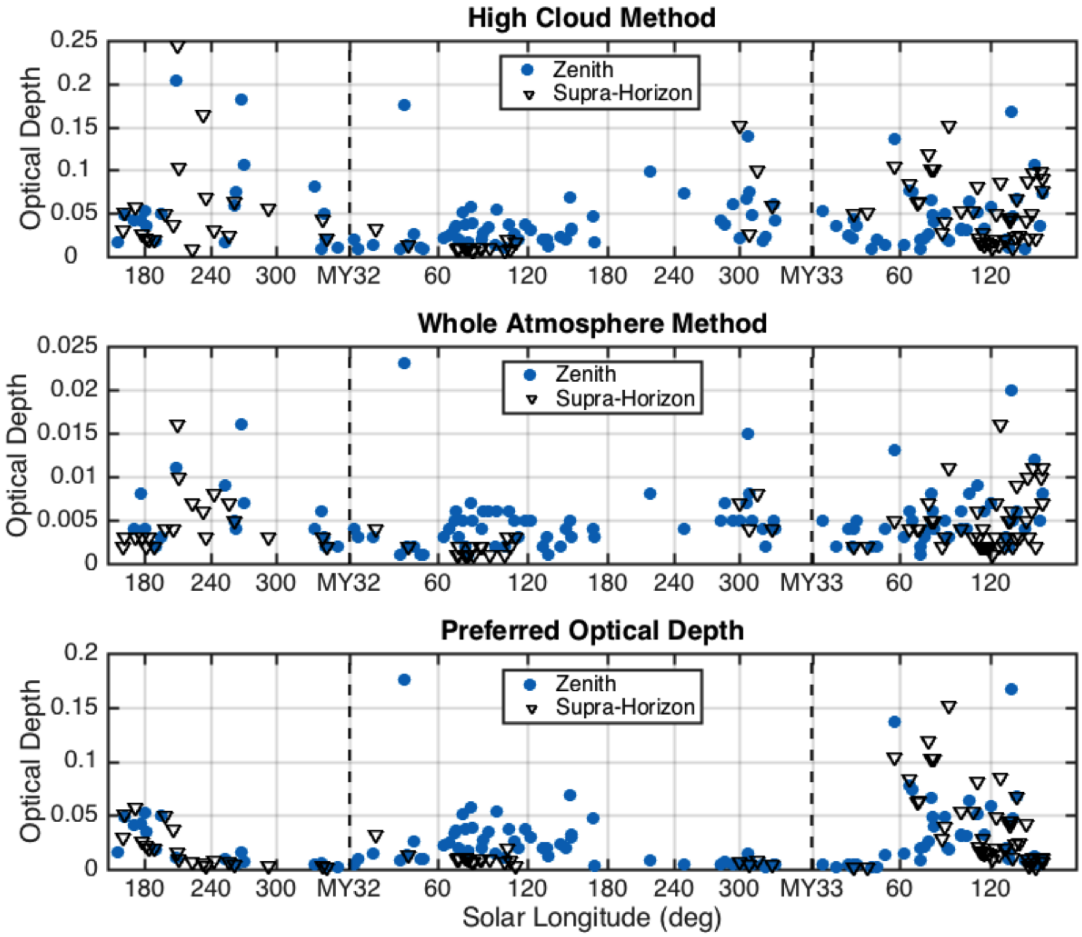

Figure 4.5: Optical depth measurements for ZMs and SHMs using both the High Cloud Approximation method (top) and the Whole Atmosphere approximation method (middle). Note that the y-axis is different for both data subplots. The bottom panel shows the preferred optical depth as a function of season.

the peak in cloud opacity is offset 10° north of the equator. This offset is attributed to the current global distribution of water vapour, given that most of the planet's water is currently trapped in the northern hemisphere.

For the time intervals when the whole atmosphere method is preferred, the average opacity varies between 0.004 and 0.008. This level of opacity is exceptionally low, however it does appear consistent with the quality of observations that were acquired during these time intervals. The majority of these movies rank low on the quality scale, suggesting that the tenuous features are only just visible in the mean frame subtracted sequences.

Even for the high cloud method, the opacity values are low. An optical depth threshold of 0.03 was proposed by Sassen and Cho (1992) to separate visible and sub-visual terrestrial

cirrus clouds, suggesting that the water-ice clouds observed by MSL would be opaque enough to be visible to a human observer on the surface. Although the opacity is low on average, the transmission of solar radiation through the cloud is non-trivial for the those possessing an optical depth of 0.1 or higher. A cloud with an optical depth of 0.1 allows 90% transmission, while an optical depth of 0.2 would allow 80% transmission of the total solar energy to reach the surface. This effect could be large enough to influence temperatures at the surface, however the radiative impacts of the MSL clouds is beyond the scope of this work and will not be discussed.

4.3 Cloud Spacing

Estimations of the cloud spacing obtained from the FFT analysis are plotted as a function of season in figure 4.6. In total there are 199 measurements: 113 from the ZMs and 86 from the SHMs. These data points correspond to observations that ranked quality 1 or higher.

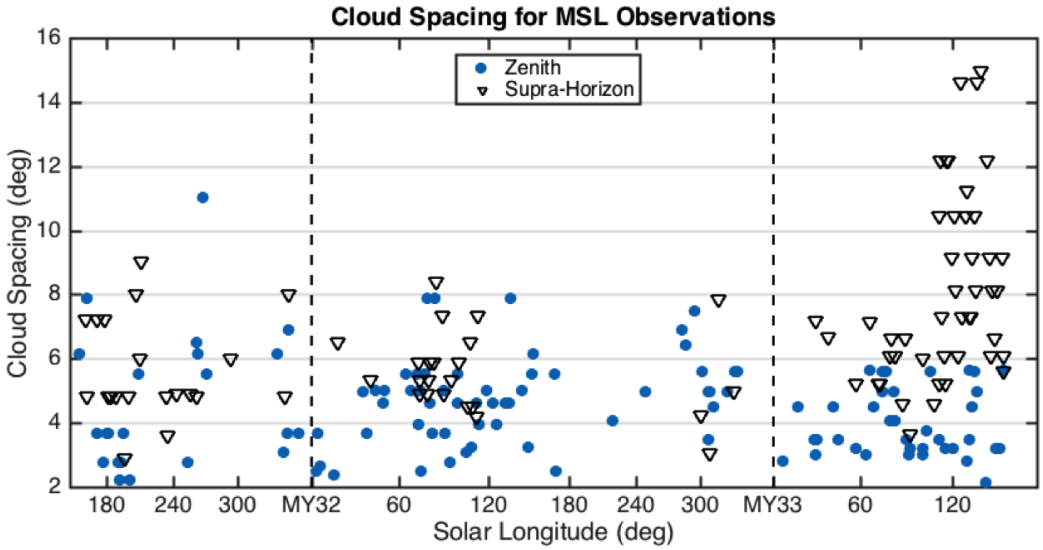

Figure 4.6: Cloud spacing for the ZMs and SHMs over the study period. The spacing is seasonally consistent, with the average spacing of 5.5°. Assuming a height of 30 km, the corresponding distance would be 2.9 km.

To account for the oblique viewing angle of the SHMs, the SHM spacing values have been corrected using the NavCam pointing elevations given in table 3.2. As discussed in section 4.1.2, however, clouds are more frequently observed in the upper parts of the mean frame subtracted images while, due to the longer path length through the atmosphere, the sky nearer the horizon resembles background noise. This can be seen in the sol 1258 and 1138 SHMs shown in figures 4.4a and 4.4c, respectively. Given the vertical gradient of cloud

visibility in the SHMs frames, the peak circular frequency will occur in the upper regions of the frame where the contrast between the cloud and the background sky is greatest. While the precise elevation, or elevation range, of the peak circular frequency for a particular observation cannot be known, it is reasonable to assume it lies somewhere between the top of the image and the centre, or, on average, 11.25° above the image centre. Thus, to approximate the spacing for the SHMs, λ_{CHAR} is divided by $\cos(90 - \theta + 11.25°)$, where θ is the pointing elevation of the NavCam.

The characteristic wavelength, λ_{CHAR}, of the cloud features ranges from 2° to 15°, however approximately 91% of the data lies within the range $2° - 8°$. For both the ZMs and SHMs, λ_{CHAR} lies consistently between $2° - 8°$ from the beginning of the mission up until $L_S = 42$ of MY 33, after which 36% of the SHM spacing values are $> 8°$. The spacing values for the ZMs, however, during the same $L_S = 42° - 160°$ period of MY 33, λ_{CHAR} remains consistently $< 8°$, and does not exhibit the same increase as the SHMs.

Considering the ZMs and the SHMs, the average spacing for the data set is $\overline{\lambda}_{CHAR} = 5.5°$. Although the altitude of the clouds cannot be ascertained through the NavCam images, estimations of the cloud spacing, in units of distance, can be made using orbital observations from MCS. As will be discussed in section 4.6, water-ice opacity retrievals from MCS show a primary cloud deck at approximately 30 km, such as the profile collected at $L_S = 61.1°$. If this height is assumed for the clouds observed in the NavCam movies, the estimated average spacing of the clouds would be approximately 2.9 km.

4.4 Seasonal and Diurnal Wind Direction

The meteorological wind direction was determined by recording the direction of cloud motion for the ZMs acquired during aphelion season when water-ice clouds are observed from orbit. The resultant wind directions are shown as a function of season in figure 4.7a, and as a function of LTST, plotted separately for MY 32 and 33 in figures 4.7b and 4.7c, respectively. In examining the seasonal wind data in figure 4.7a, there are no significant trends observed however a westward cloud motion (270°) is most commonly observed in MY 32 and 33. Additionally, no trends are found when wind direction is plotted as a function of LTST, however the lack of early morning observations, and the time restriction near noon, disallow such information to be obtained in MY 32. Although MY 33, owing to the increased number of morning observations, lends itself better to a discussion of diurnal wind patterns, as is shown in figure 4.7c, no conclusive patterns are observed. Westward winds do appear marginally more frequent in the afternoon, whereas north and northeast winds are more common in the morning hours, however the limited data available prevent any definitive

conclusions from being drawn.

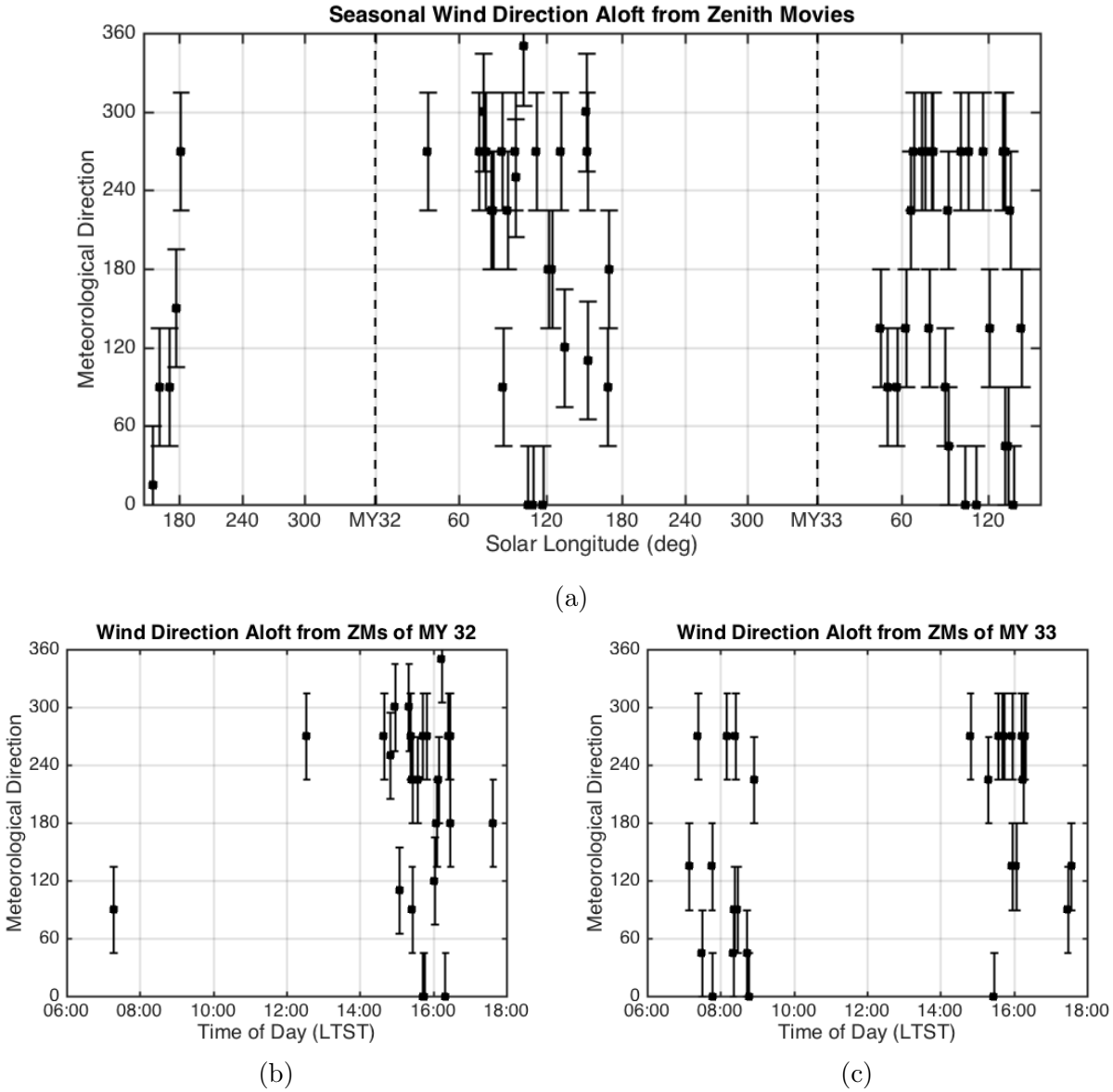

Figure 4.7: (a) Meteorological wind direction obtained for the ZMs as a function of season for the study period with 45° error bars. The meteorological direction is measured in degrees clockwise from north, i.e. 0° is north, 90° is east, etc. (b) Wind direction as a function of LTST for MY 32. (c) Wind direction as a function of LTST for MY 33.

The overwhelming majority of NavCam movies are characterized by clouds moving in a single direction, however a small number of movies appear to exhibit cloud movement in two distinct overlapping motions. This can be explained by the presence of multiple cloud layers aloft. Moores et al. (2015a) observed this phenomenon in the sol 40 SHM (see figure 10 of Moores et al. (2015a)), in which clouds could be seen moving from south to north while

separate clouds exhibited a movement towards the rover over the top of Mt. Sharp. The best example, however, can be seen in the sol 543 ZM captured at approximately 07:16 LTST, which is shown in figure 4.1d. The image panels in figure 4.1d show distinct movement of clouds in two opposing directions: clouds within the red box show movement from east to west, while clouds in the blue box show movement from west to east. Both cloud layers appear to move at a similar speed within the movie, although it is likely that they are at different altitudes. Multiple cloud layers are also observed in two of the MCS water-ice profiles shown in figure 4.9b: $L_S = 190^\circ$ and $L_S = 145^\circ$.

4.5 Detections of Atmospheric Gravity Waves

Atmospheric gravity waves are disturbances in a stably-stratified atmosphere in which a parcel of air oscillates between two altitudes, being pushed and pulled by the buoyancy force and gravitational force, respectively. Gravity waves can be generated by frontal systems as well as air flow over large topographic features (Read and Lewis 2004), and have been important for advancing our understanding of the horizontal temperature gradients of the the mesosphere of Earth's atmosphere (Andrews, Holton, and Leovy 1987). One way in which gravity waves within the atmosphere can be detected is through the presence of clouds that form in the peaks of the wave. These clouds are characterized by long, but not wide, evenly spaced strips of cloud formation. An example of terrestrial gravity wave clouds imaged in Antarctica is shown in figure 4.8a.

Mars has both a stably-stratified atmosphere and large topographic features which enable the presence of gravity waves. When the Mariner 9 probe flew by Mars in 1971, it returned the first direct observations of gravity waves in the Martian atmosphere (Leovy, Briggs, and Smith 1973), and since this time many other observations have been made. The MSL cloud movies have also made several detections of gravity wave clouds, which are likely topographically generated by surface features within the region. Two of the most convincing examples of gravity waves are the sol 1181 ZM and the sol 1302 south-facing SHM, a single frame from which is shown in figure 4.8b and 4.8c, respectively.

The sol 1181 ZM shows tenuous ripples of evenly spaced clouds, that appear most visible in the lower right-hand side of the frame (highlighted by the red box in figure 4.8b). The cloud features appear relatively small within the frame, and exhibit a low characteristic wavelength of $\lambda_{CHAR} = 3.61^\circ$, suggesting that they are located at a high altitude. If these clouds are assumed to be at an altitude of 30 km, the horizontal spacing of the would be approximately 1.8 km. The opacity of these clouds, using the high cloud method, is $\Delta\tau_{HC} = 0.021 \pm 0.003$.

The best detection of gravity waves, however, comes from the sol 1302 south-facing SHM.

(a)

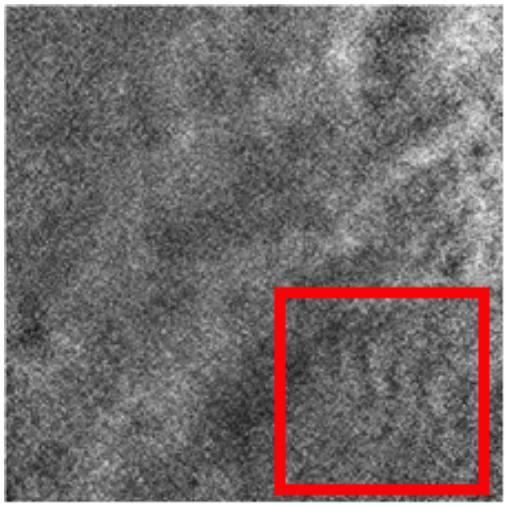

(b)

(c)

Figure 4.8: (a) Cloud formation associated with gravity waves in the antarctic atmosphere on Earth. Photo: Chris Wilson (b) Possible gravity waves from the sol 1181 ZM. Thin, evenly spaced ripples of cloud can be observed (highlighted by the red box) that appear characteristic of gravity waves. (c) A single frame from the sol 1302 SHM in which straight rows of clouds rigidly translate towards the rover.

In this movie, relatively opaque linear rows of clouds ($\Delta\tau_{HC} = 0.045 \pm 0.004$) appear to rigidly translate in a direction towards the rover. Interestingly, these clouds appear more opaque towards the horizon, which is atypical for the SHM observations. This could suggest that the clouds in the sol 1302 SHM are located at a lower altitude in the atmosphere. The characteristic wavelength measured is low, at only $\lambda_{CHAR} = 2.19°$.

4.6 Lower Constraints on the Scattering Phase Function of Martian Clouds

The value of the phase function used in the high cloud equation depends on the scattering angle, and thus should change with each MSL cloud observation. Understanding the relationship between the phase function and the scattering angle enables more information to be obtained about the clouds themselves. Such information lends insight into the physical ice crystal shapes (plates, columns, bullet-rosettes, etc.) that comprise these clouds by comparing their phase function with Earth-based measurements of cirrus clouds and laboratory-derived particle shape phase functions (Chepfer et al. 2002). The high cloud equation (equation 3.8) may be rearranged to solve for the phase function:

$$P(\Theta) = \frac{4\pi I_{\lambda,var}\mu\Delta\lambda}{\Delta\tau_{MCS}F_{\lambda}exp(-\frac{\tau_{COL}}{\mu})} \tag{4.1}$$

In this formulation, instead of using an assumed value of the phase function to calculate $\Delta\tau$, values obtained from the Mars Climate Sounder (MCS) water-ice opacity retrievals, here termed $\Delta\tau_{MCS}$ can be used to place limits on the phase function. The MCS instrument is a limb sounding instrument on board the MRO spacecraft, and is capable of acquiring vertical profiles of temperature, pressure, water-ice, and dust using 8 separate channels in the thermal IR range (Kleinböhl et al. 2009). In total, there are 12 water-ice optical depth retrievals selected from MCS between $L_S = 9° - 161°$ that were acquired within 5° latitude and longitude of Gale Crater. These are shown in figures 4.9a and 4.9b. For each selected water-ice profile an optical depth is given, and is displayed in text on the right-hand side of figure 4.9b.

Using these values, the phase function was calculated for both the ZMs and SHMs that occurred nearest in time to the MCS measurement. The scattering angles were calculated using a spherical coordinate system based on the position of the Sun and the pointing of the NavCam at the time of the NavCam observation. The calculated scattering angles range between 50° and 120°. For both the ZMs and the SHMs, the majority of the scattering angles were between 60° and 80°, however one point, from the Sol 507 SHM, gave a scattering angle

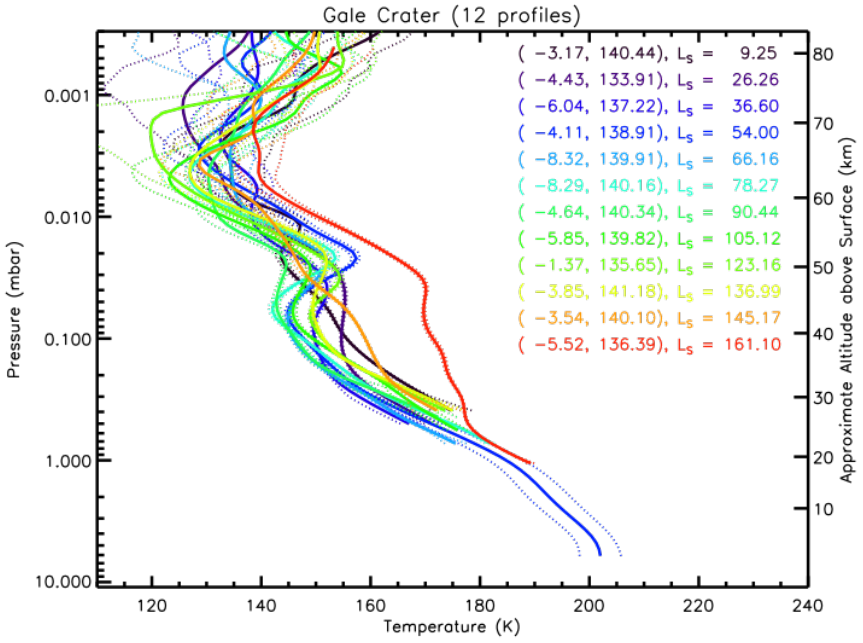

(a)

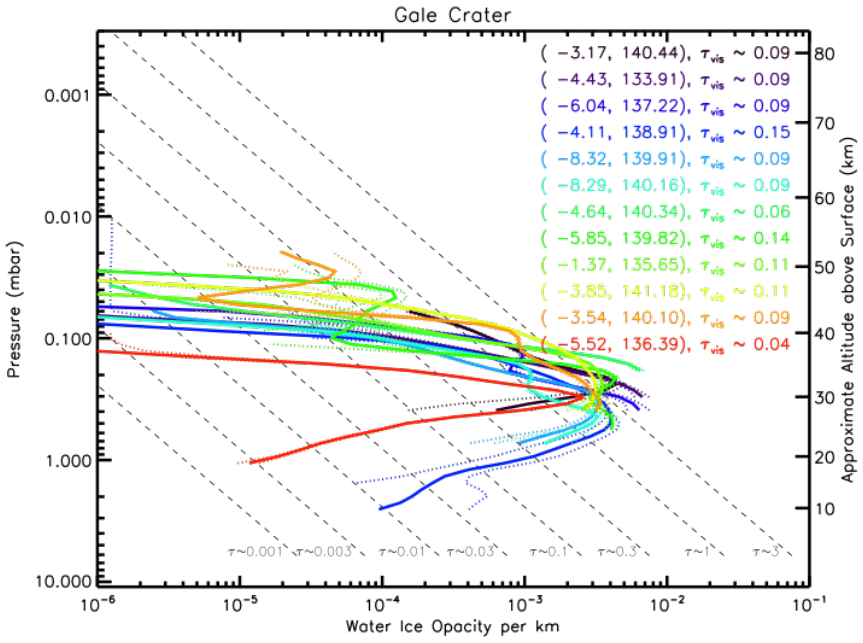

(b)

Figure 4.9: (a) Mars Climate Sounder temperature profiles within 5° latitude and longitude of Gale Crater. (b) MCS water-ice opacity retrievals within 5° latitude and longitude of Gale Crater

of 120°. Tables 4.2 and 4.3 provide the parameters used in the scattering angle calculations as well as the phase function calculations for the Zenith and Supra-Horizon Movies, respectively.

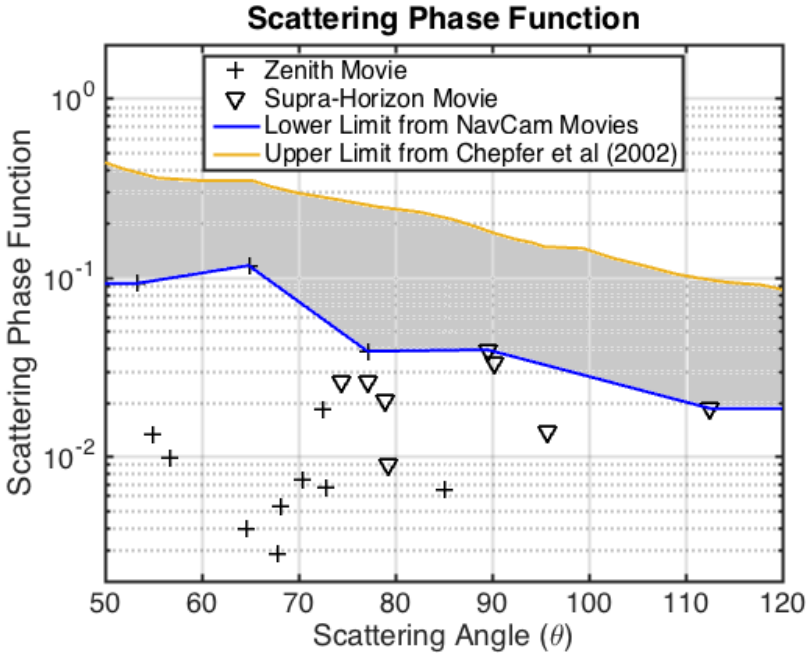

Figure 4.10: The scattering phase function calculated using optical depth measurements provided by MCS. 12 measurements from the ZMs and 8 measurements from the SHMs are shown. The gold line represents the upper limit of the scattering phase function provided by Chepfer et al. (2002) while the blue line represents the lower limit given by the NavCam movies. The grey shaded region represents the scattering phase function range for the Martian Clouds observed within the NavCam movies.

Figure 4.10 shows the phase function distribution calculated from the NavCam movies and MCS data as a function of scattering angle. In total, there are 12 estimates provided from the ZMs, and 8 from the SHMs. This plot shows that for a given scattering angle, a range of phase function values are obtained. This can be explained by the measured value of $I_{\lambda,var}$. Recall that $I_{\lambda,var}$ is the variation in spectral radiance between the cloud and the adjacent region. If the region adjacent the cloud is empty sky, then the measured value of $I_{\lambda,var}$ is a maximum. However, for most of the observations, it is likely that the adjacent region is not entirely empty, but is instead a more tenuous region of the same cloud. If we are not measuring the complete depth of the cloud, then $I_{\lambda,var}$ is lower limit, and, given that $I_{\lambda,var}$ is proportional to P, this also implies that P is a lower limit given that all the remaining parameters in equation 10 are robust. In figure 4.10, the blue line connects the largest calculated values of P, and provides a lower limit on the phase function for the Martian clouds observed in the NavCam movies. The obtained values for P that lie below this curve are measurements in which $I_{\lambda,var}$ is not representative of the full depth of the

Table 4.2: The parameters used in the calculation for the scattering angle and phase function for the Zenith Movies. The scattering angle was calculated using a spherical coordinate system based on the position of the sun given in Solar Elevation and Solar Azimuth, and the position of the NavCam, given in Viewing Elevation and Viewing Azimuth.

Sol	L_S	LTST	$\Delta\tau_{MCS}$	Solar El.	Solar Az.	View El.	View Az.	SA	P
363	6.79	17:38	0.09	5.0	273.3	85.2	181.6	85.2	6.46E-03
424	36.8	16:17	0.09	23.4	288.1	85.1	181.1	68.1	5.25E-03
429	38.5	16:27	0.09	26.7	288.4	85.1	181.1	64.9	1.16E-01
453	49.5	15:55	0.15	27.5	294.1	85.1	178.9	64.7	3.90E-03
493	67.4	07:33	0.09	19.4	63.5	85.1	179.0	72.8	6.66E-03
513	76.5	14:56	0.09	38.1	306.2	85.0	179.7	55.0	1.31E-02
543	89.9	07:16	0.06	15.1	62.3	85.1	179.1	77.2	3.85E-02
574	104.2	16:13	0.14	21.9	298.6	85.1	180.9	70.4	7.28E-03
612	122.2	16:05	0.11	24.6	295.8	84.9	178.8	67.8	2.85E-03
638	134.9	15:20	0.11	35.8	295.5	84.9	178.1	56.7	9.79E-03
663	147.7	16:36	0.09	19.0	285.6	84.9	179.1	72.5	1.81E-02
701	168.2	15:25	0.04	37.8	280.0	84.9	179.7	53.3	9.22E-02

Table 4.3: The parameters used in the calculation for the scattering angle and phase function for the Supra-Horizon Movies. The scattering angle was calculated using a spherical coordinate system based on the position of the sun given in Solar Elevation and Solar Azimuth, and the position of the NavCam, given in Viewing Elevation and Viewing Azimuth.

Sol	L_S	LTST	$\Delta\tau_{MCS}$	Solar El.	Solar Az.	View El.	View Az.	SA	P
388	19.0	14:41	0.09	47.8	287.3	38.6	134.6	90.25	3.34E-02
435	41.2	14:43	0.09	44.5	298.3	38.4	134.8	95.73	1.38E-02
505	72.8	12:40	0.15	59.7	341.5	38.6	134.9	79.24	8.90E-03
507	73.8	15:47	0.09	27.7	300.4	38.4	134.5	112.57	1.84E-02
517	78.3	12:34	0.09	59.6	344.6	38.4	134.7	78.94	2.04E-02
553	94.5	12:00	0.06	60.2	359.7	38.7	134.9	74.47	2.62E-02
579	106.5	12:25	0.14	60.6	348.1	38.6	134.9	77.17	2.61E-02
590	111.6	13:45	0.11	52.0	318.5	38.4	134.9	89.53	3.93E-02

cloud.

In figure 4.10, the upper limit is shown as a gold line, and is taken from figure 1 of Chepfer et al. (2002). To aide the reader, figure 1 of Chepfer et al. (2002) is reproduced here as figure 4.11. This line represents the upper limit of P for 14 different ice crystal types for scattering angles between $L_S = 50^\circ - 120^\circ$. The gray-shaded region between the upper and lower limit curves represents the range of P with respect to scattering angle for the Martian clouds observed in the Zenith and Supra-Horizon Movies. By comparing P for the 14 different ice-crystal types shown in figure 1 of Chepfer et al. (2002) with the shaded region shown in figure 4.10, the majority of the ice-crystal types fall within this region, and thus represent

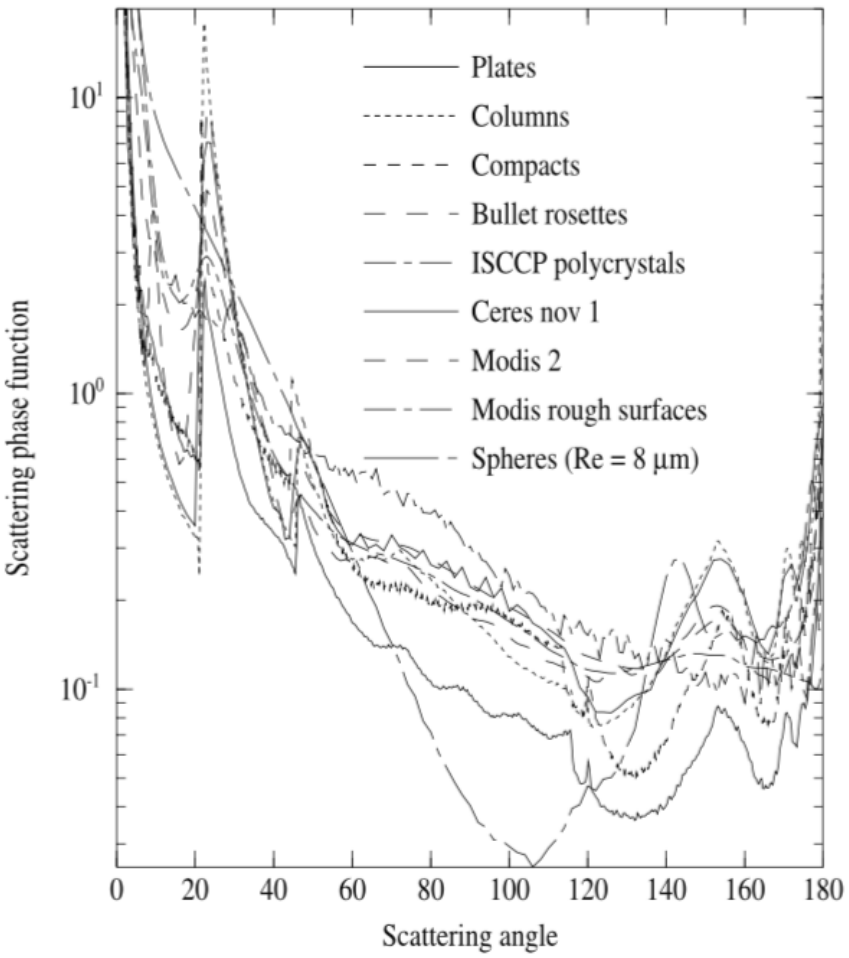

Figure 4.11: Plot from Chepfer et al. (2002) showing laboratory derived measurements for the scattering phase function over a range of scattering angles for 14 different ice-crystal types.

potential crystal types for the MSL clouds. The scattering phase function for the spheres, however, dips below the lower limit curve set by the NavCam and MCS measurements and can tentatively be eliminated as a potential ice-crystal shape for the MSL clouds. A greater distribution of scattering angles is needed to further constrain the ice-crystal shapes of the MSL clouds, however, this preliminary analysis is the first attempt to restrict the phase function of Martian clouds. This initial analysis indicates that the clouds within the Zenith and Supra-Horizon Movies are not composed of material with exotic scattering properties.

4.7 Thresholds for Cloud Detection as Evidenced by the featureless SHMs

Recent analysis of the atmospheric movies has highlighted the role that the length of time between the first and last image of the movie, hereafter referred to as span, plays in the ability of the observation to successfully resolve clouds. The ZMs and the Original Mt. Sharp Movies consist of eight images that span 91 seconds. This combination of time span and frame number has been seen to produce high quality movies using mean frame subtraction, as is evidenced by the numerous movies that detect clouds with good contrast using this combination.

However, the Mt. Sharp + LOS were implemented on sol 594 ($L_S = 113^\circ$), and consisted of only four images captured over 39 seconds. The shorter run-time was selected for purely operational reasons: the short duration allowed this observation to be captured more frequently. These new movies also utilized an alternate pointing such that a portion of Mt. Sharp was captured in the frame. This necessitated applying less compression to the individual images to ensure that fine details in the sky were preserved for analysis. The decrease in compression, in turn, required a reduction in the number of frames to keep the total data volume for the observation unchanged. While the new pointing was able to provide information on dust levels within the crater, these new observations did not prove useful for detecting clouds, as clouds were not observed in any of the Mt. Sharp + LOS movies. This was surprising given that ZMs consistently detected clouds during $L_S = 113^\circ - 167^\circ$ of MY 32 (see table A.1) and water-ice clouds at equatorial latitudes were regularly reported from MARCI up until $L_S = 172^\circ$ in MY 32 (Malin et al. 2014a).

There were two possible causes of the apparently featureless SHMs: either clouds were unusually thin or absent during this period, or, alternatively the change to the observation inadvertently decreased its sensitivity. The fact that clouds continued to be observed in the ZMs suggests that it was the change in the observation that was at fault, which in turn suggests that either (1) the decrease in the number of frames or (2) the decrease in the span of the frames might have increased the cloud detection threshold. To isolate which of these factors was the cause of the apparent lack of clouds in the new SHM, we began by looking at the movies acquired during the early periods of the mission, which had a higher frame number, longer time span and displayed distinctive clouds after mean frame subtraction. By degrading these movies and running them with different combinations of time span and frame number, we could determine the degree to which each parameter affects the quality of the movie.

The sol 49 ZM was a good candidate for degradation; it is one of the higher quality movies

and was acquired with 26 frames covering 325 seconds. The initial test was to degrade the sol 49 ZM by running it using the mean frame subtraction technique with the first four frames in the sequence, spanning 39 seconds, and also running it with four frames that spanned the entire 325 seconds. Figure 4.12 shows the results of this test. Image panel (a) shows 8 perturbation images from the sol 49 ZM that span the entire 325 seconds, with the upper leftmost image taken at t = 0. Image panel (b) shows the sol 49 ZM as run with the first four frames in the sequence while panel (c) shows the same movie ran with four frames that span the entire 325 seconds. By running the movie with only the initial four frames, the quality of the movie is significantly diminished, as each frame appears more homogeneous and the clouds cannot be clearly discerned. In contrast, by running the movie with four frames that preserve the original time span, the clarity and contrast of the clouds is also preserved.

The sol 49 test showed a clear relationship between the quality of the movie and movie span, however an additional test using synthetic data was constructed to determine the time span threshold necessary for detecting the tenuous clouds. In this test, we simulated the clouds that are visible in the atmospheric movies by propagating a sine wave with a 30-pixel wavelength diagonally across a 512×512 pixel image. Gaussian noise was added to simulate the noise from the NavCam, and then the images were compressed as they would be onboard the rover before transmission to Earth. The images were then re-expanded, and processed identically to the ZMs and SHMs using the mean frame subtraction technique. Instead of varying the time span as was done with the degradation tests, the equivalent adjustment was the distance, or number of cycles, the sine wave was allowed to propagate. The number of cycles was adjusted between 1/8 and 1, in addition to adjusting the number of frames. The results, documented in 4.13, showed that increasing the number of cycles resulted in better contrast and quality. In fact, by increasing the span to cover the amount of time required for the clouds to translate through one wavelength, a maximum sensitivity was derived. To correct the issue of the featureless SHMs, new observations were created with a 240 second time span.

The results of the degradation tests and the synthetic data tests showed a clear relationship between the distance that the clouds translate across the frame and the quality of the movie. By increasing the time between successive images in the sequence, the clouds are able to translate a greater distance across the frame. This has important implications for increasing the contrast of the observed clouds due to the mean frame subtraction technique applied. However, there are implications of this that apply specifically to the SHMs given the low elevation angle of the camera. When clouds in the SHMs are moving in a direction towards or away from the camera, they are translating only a fraction of the distance that they would if they were moving in a direction parallel to the lens of the camera. Thus, the

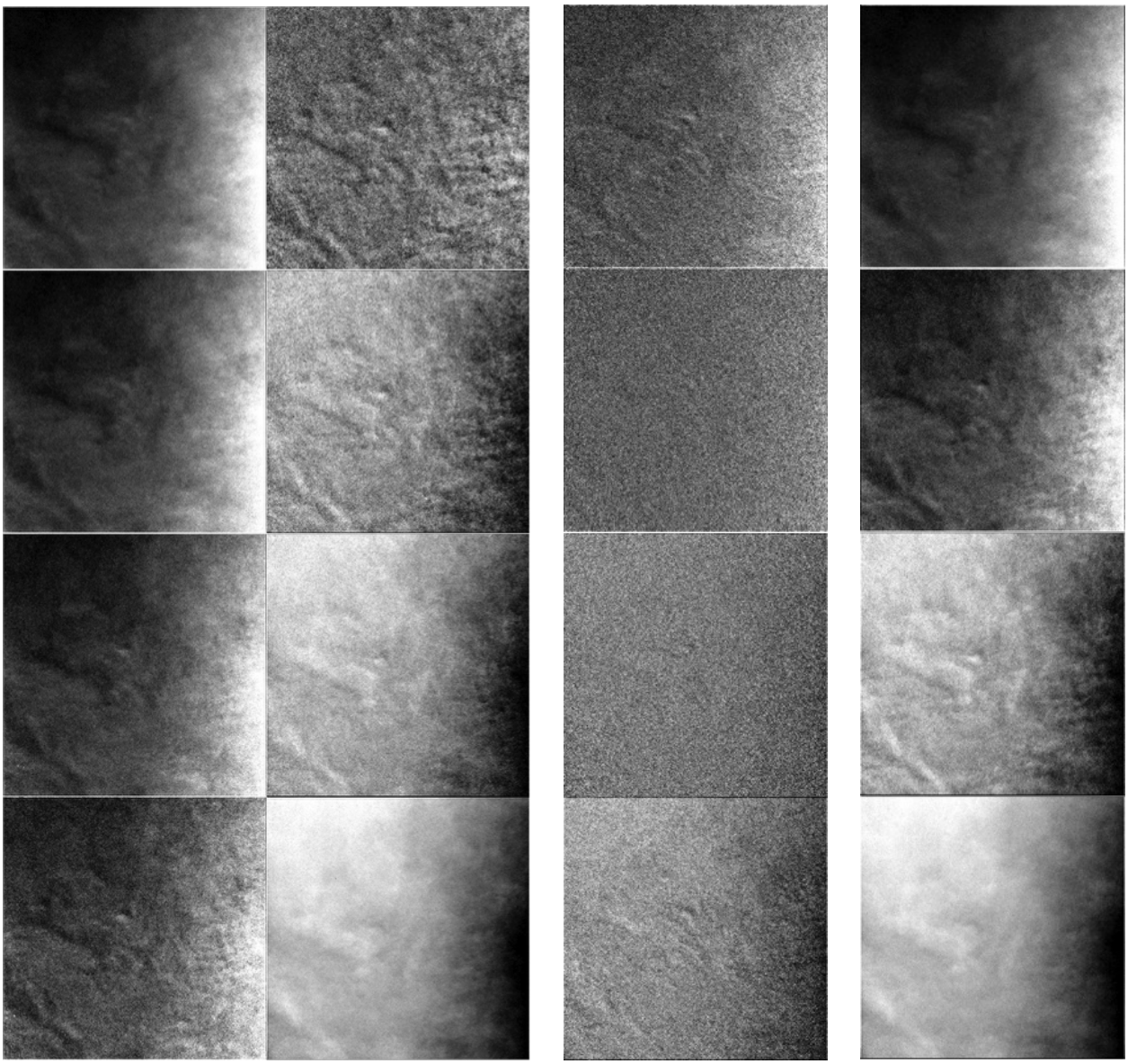

(a) (b) (c)

Figure 4.12: Sol 49 degradation test. (a) 8 perturbation images from sol 49 ZM that span 325 seconds. The top left frame is the first frame of the sequence and represents t = 0, with the sequence moving in time from top to bottom. The upper right image is the 16th frame in the sequence, and represents t = 203 sec while the bottom righthand image is the last frame, representing t = 325 sec. This movie was run using 26 frames, however only 8 are included here. (b) Sol 49 degraded to the first four images that span 39 seconds. Note the homogeneity and low resolution of the images. (c) Sol 49 degraded to four images that span the 325 seconds. Note how the clarity of the clouds matches that of the original movie.

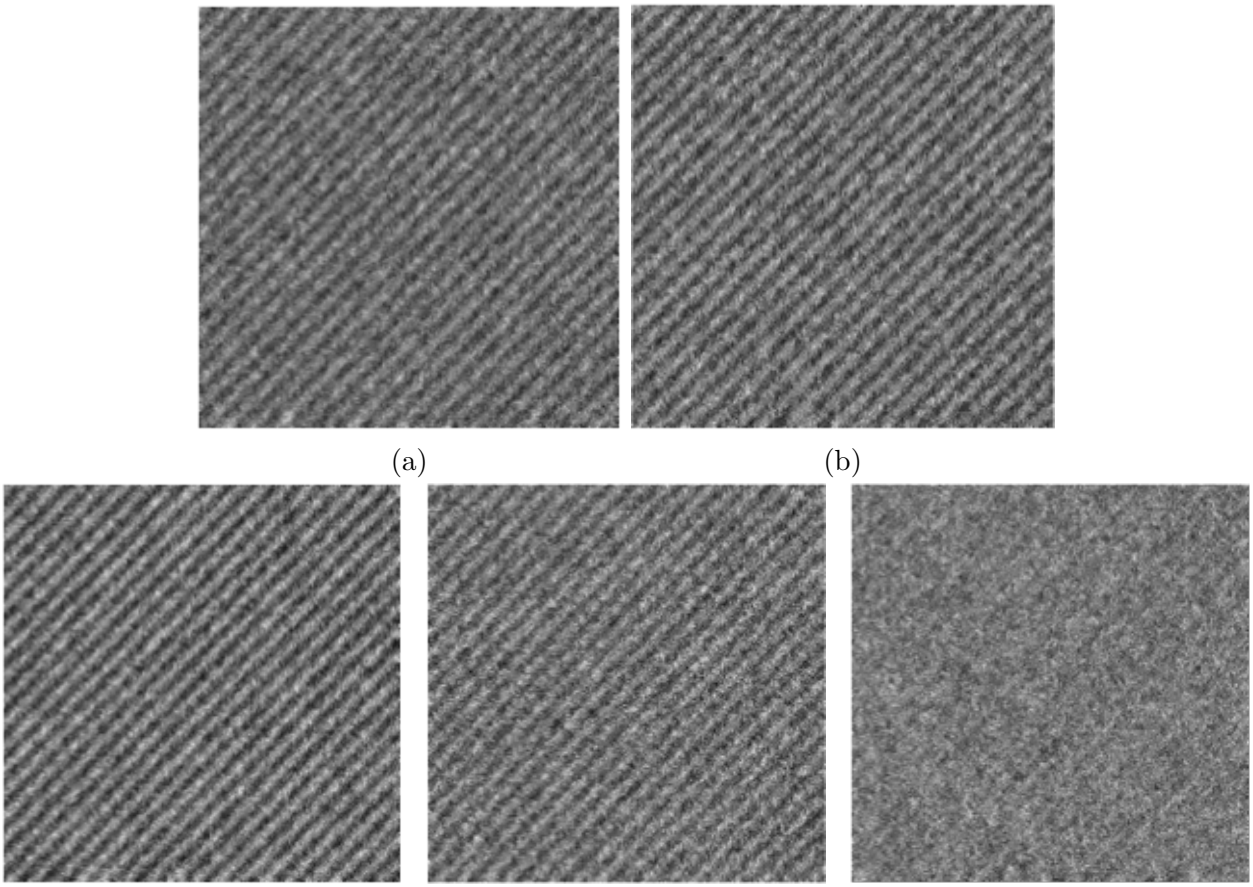

Figure 4.13: (a) single frame from synthetic data test with 4 frames allowing 1 wavelength translation. (b) A single frame from synthetic data test with 8 frames allowing 1 wavelength translation. (c) A single frame from synthetic data test with 4 frames allowing 1/2 wavelength translation (d) A single frame from synthetic data test with 4 frames allowing 1/4 wavelength translation time. (e) A single image of the synthetic data test run with 4 frames and allowing the sine wave to translate 1/8 of a wavelength. This test confirmed that the time span was the important parameter that affected movie quality, and that by allowing the clouds to translate one wavelength, a maximum sensitivity was derived.

disparity of cloud detection between the ZMs and SHMs is likely a result of the relative sensitivity of the observations due to the difference in elevation angle pointing of the NavCam. The fact that ZMs and SHMs acquired during the early parts of the mission (sol $0 - 60$) contemporaneously observe clouds might indicate an unusually cloudy period in the mission. Additionally, it is unlikely that clouds are not present in the SHMs during the $594 - 800$ period as clouds are regularly detected within the ZM data set.

Chapter 5

Terrestrial Cloud Experiment: Instrumentation and Setup

5.1 York University Lidar Instrument

A lidar instrument operates by rapidly pulsing a laser into the atmosphere and collecting the backscattered radiation using a telescope positioned adjacent to the laser transmitter. The backscattered radiation is measured as a function of time, which is converted to distance using the speed of light. The specific wavelength of the pulsed laser depends on the targeted atmospheric species: for detecting water-ice clouds, a 532 nm laser is used while dust aerosols require a wavelength of 1064 nm.

The York University lidar instrument is housed on the fourth floor of the Petrie Science and Engineering building at York University's Keele campus in Toronto, ON. It was built as a prototype of the lidar instrument that flew on the Phoenix Mars Lander in 2008, which made atmospheric measurements of condensate clouds (Whiteway et al. 2009) and dust (Komguem et al. 2013) in the north polar region of Mars. The York University lidar prototype was used to perform similar measurements on Earth in order to develop and characterize the methods that would later be used in the Martian environment (Popovici 2012; Whiteway et al. 2008). Both the Phoenix and York University lidar instruments have the same functionality, and are only appreciably different in terms of appearance and laser output energy.

The York lidar measurements are made using a Nd:YAG (neodymium-doped yttrium aluminum garnet) laser which is rapidly pulsed vertically into the atmosphere at a frequency of 20 Hz. A common way to display the return signal of the lidar is known as a contour plot. A contour plot is a 3-dimensional map showing the local time on the x-axis, altitude on the y-axis, and the lidar extinction coefficient (units of 1/km) on the colour axis. The

benefit of displaying the data this way is that it provides an accurate portrayal of the cloud altitude thickness as a function of time. An example of the lidar contour plot from the second coordinated experiment on May 5, 2016 is shown in the right panel of figure 5.1.

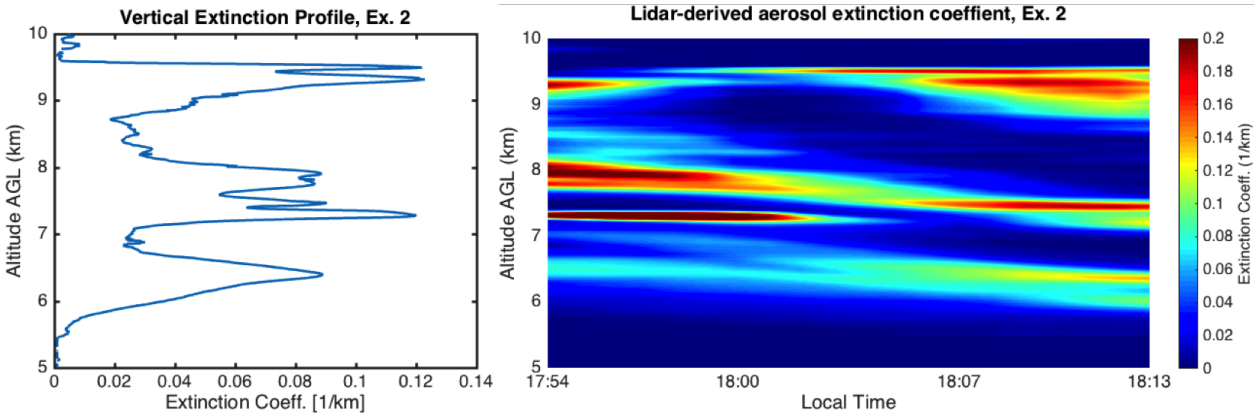

Figure 5.1: Left: A vertical extinction profile of cirrus clouds created by taking the time-averaged extinction at each altitude from the lidar contour plot. Right: Example of a lidar contour plot from the York University lidar instrument. Shown on the y-axis is the altitude above ground level (AGL) and plotted on the x-axis is the local time. The extinction coefficient (units of 1/km) of the lidar beam is represented by the colour axis, with the colourbar showing the corresponding extinction values.

From this measurement, three distinct layers of water-ice cloud are visible by their high extinction value, which are located at 6.5, 8 and 9 km above ground level (AGL). By taking the time-averaged extinction at each altitude, as is shown in the left panel of figure 5.1, the three layers become even more apparent. To determine the cloud opacity derived from the lidar measurements, the vertical extinction profile is integrated over the altitude range of the cloud at each sampled time interval (approximately 1 minute), and plotted as a function of time.

5.2 Description of Photographic System

The imager used for the lidar-coordinated experiments was a DCC1545M scientific camera (shown in figure 5.2a). The DCC1545M, manufactured by ThorLabs and hereby referred to as "ThorCam", uses a monochromatic CMOS sensor with a bit depth of 8 bits per pixel, giving each pixel a possible DN between 0 and 255. A radiometric calibration was performed on the camera to determine its output response in DN for a given spectral radiance input and exposure time. The final conversion factor obtained from the calibration was 2.3×10^{-3} W ms DN^{-1} m^{-2} Sr^{-1}, which was applied to all experimental image sequences. A comprehensive description of the calibration procedure, apparatus and analysis is given in appendix B.

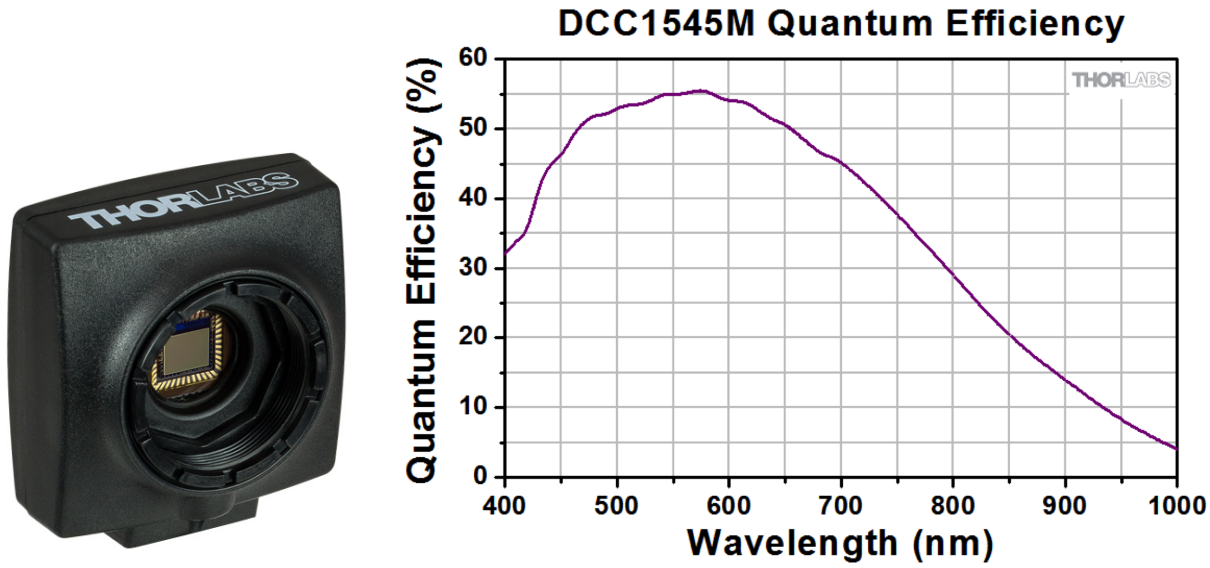

(a) (b)

Figure 5.2: (a) An image of the DCC1545M, without the lens and showing the CMOS sensor. (b) The Quantum Efficiency (QE) as a function of wavelength for the CMOS sensor of the DCC1545M.

The camera's CMOS sensor is 1280×1024 pixels in resolution and is responsive to wavelengths between $400 - 1000$ nm. The quantum efficiency (QE) for the sensor is shown in figure 5.2b. Note that the ThorCam is sensitive to a wider distribution of wavelengths than is the MSL NavCam. Given that clouds are spectrally neutral within this region of the electromagnetic spectrum, i.e. they attenuate all wavelengths of light evenly in this region, the difference in spectral responsivity between the two imagers does not need to be separately accounted for. A 12 mm focal length lens with an aperture of 1.4 mm was affixed to the camera. The resulting FOV is 30° for the horizontal and 24° for the vertical (38.5° specified for the diagonal).

5.2.1 Experimental Set up and Terrestrial Data Set

In total, 4 lidar-coordinated experiments were conducted between September of 2015 and June of 2016. As the position of the Sun in the early afternoon was not suitable for atmospheric imaging using a vertical camera pointing, all 4 experiments were conducted between 13:30 and 18:00 local time. The date of each experiment was selected based on the presence of high altitude cirrus clouds in the vicinity of York University, and the scheduling coordination between the lidar operator and the camera operator.

To acquire a terrestrial Zenith Movie, the ThorCam was positioned vertically using a tri-

Table 5.1: Lidar Experiment Summary Table

	Experiment Number			
	1	2	3	4
Date	Sep. 30, 2015	May 5, 2016	May 11, 2016	June 1, 2016
Local Time	15:40	17:54	17:09	16:51
Solar Elevation	32.5°	25.6°	34.8°	41.1°
Solar Azimuth	226.2°	268.3°	261.8°	261.7°
Scattering Angle	57.5°	64.4°	55.2°	48.9°
Exposure Time (ms)	11.3	15	5	7
Neutral Density Filter	-	2.4	2.2	2.5

pod mount, such that the elevation angle for the pointing was 90°. Stray light was minimized by positioning the camera in a shaded region for which the overhead sky was unobstructed. For experiments 2, 3 and 4, this was directly outside of the building that housed the lidar instrument, and in the case of the first experiment, was on the roof of the same building. Imaging and lidar data were collected over a 20 minute time interval using a synchronized start and end time. The imaging data was acquired using an identical frame rate as the original ZMs, such that one image was captured every 13 seconds. Thus, each experimental image sequence consists of 80 images. All subsequent analysis is achieved using flat field and dark current corrected images. Mean frame subtraction is not performed as it is not needed to identify the cirrus clouds.

Given that the opacity calculations rely on precise measurements of radiance, it is necessary to account for all the light that is entering the optical system of the camera. Furthermore, it is important to ensure that the images are not saturated. The radiometric calibration of the ThorCam did not account for the aperture setting of the camera, and only took into account the camera's exposure time. Thus for each experiment, the aperture was set to a maximum position, and the exposure time was adjusted to control the amount of light entering the system. Even for the lowest exposure time allowable for the camera, however, the brightness of the outdoor scene was great enough to oversaturate the images. To further restrict the amount of light entering the camera's optical system, a set of Neutral Density Filters (NDFs) was used.

NDFs transmit (or attenuate) all wavelengths of light light evenly, and therefore act as a virtual aperture for which the quantified radiance transmission can be determined. The transmission of the NDF is given as $T = 10^{-OD}$, where OD is the optical depth of the NDF. To utilize the camera's full dynamic range, a combination of NDFs and exposure time was used. The optical depth of the NDF used for each experiment, along with the camera exposure time, is provided in table 5.1.

5.3 Terrestrial Optical Depth Measurements

As the MSL methods for deriving cloud opacity were originally formulated for the Martian environment, adapting them to the terrestrial environment requires updating the equation's constituent terms. Beginning with the numerator of high cloud equation (equation 3.8), the single term that requires modification is the bandpass of the imager. For the ThorCam, this value is 600 nm, which is obtained from the QE of the CMOS detector provided by the manufacturers (shown in figure 5.2b).

Moving to the denominator of the high cloud equation, the values of the scattering phase function used for the terrestrial adaptation are based on laboratory-derived measurements provided by Chepfer et al. (2002) (reproduced here as figure 4.11). Chepfer et al. (2002) present the results of the scattering phase function of 14 different ice crystal types for a range of scattering angles. As the specific ice-crystal types that comprise the terrestrial cirrus clouds cannot be known, an average value of the phase function is calculated using the maximum and minimum P value at the derived scattering angle. The scattering angle, given a vertical camera pointing, is simply the camera elevation angle (90°) minus the solar zenith angle. A list of the scattering angles for the coordinated experiments is given in table 5.1.

The in-band solar flux at the top of Earth's atmosphere was determined by using a reference standard for solar spectral distribution provided by the American Society for Testing Materials (ASTM). This spectra is known as the ASTM G-173 and is shown in figure 5.3. The ASTM G-173 provides the spectral irradiance of the Sun as a function of wavelength at the top of Earth's atmosphere, as well as through 1.5 air masses (solar zenith angle 48.2°), using a mean Earth-Sun distance. The in-band solar flux at the top of Earth's atmosphere, denoted as $F_{\lambda,0}$, is found by computationally integrating the extraterrestrial radiance between 400 and 1000 nm. The in-band flux obtained is $F_{\lambda,0} = 842$ W/m^2 at the top of Earth's atmosphere, which is assumed constant for all opacity calculations.

Finally, the atmospheric column opacity τ_{COL}, which is used to determine both $\Delta\tau_{HC}$ and $\Delta\tau_{WA}$, must be amended to reflect the different atmospheric environments of Earth and Mars. For the Martian cloud calculations, the atmospheric opacity values are obtained from solar disc measurements using images from the rover's MastCam. These observations are executed with regular frequency (on average once every 10 sols) to quantitatively monitor the rise and fall of dust within the atmosphere, which changes on diurnal and seasonal timescales. On Earth, the atmospheric opacity does not oscillate in the same way that it does on Mars, and thus for all calculations a single value is used.

Earth's atmospheric column opacity was determined using Beer's law. This law relates

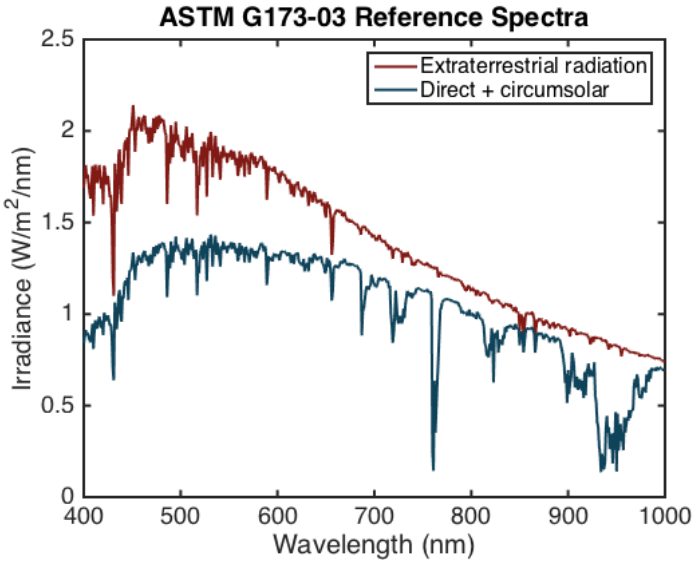

Figure 5.3: ASTM G-173 Reference spectra used to calculate in-band solar flux and atmospheric opacity for the terrestrial high cloud method. The red line is the solar irradiance at the top of Earth's atmosphere, and the blue line is the solar irradiance through 1.5 air masses. This spectra shows the O_2 absorption features at 760 nm and the broad H_2O absorption feature between $900 - 1000$ nm.

the transmittance of in-band solar flux through the atmosphere with the atmospheric opacity. This relationship is given as equation 5.1.

$$\frac{F_\lambda}{F_{\lambda,0}} = \exp\left(\frac{-\tau_{COL}}{\mu}\right) \tag{5.1}$$

Calculating the atmospheric opacity in this way accounts for the absorption features that exist in the in-band spectral region, such as the prominent O_2 absorption features at approximately 760 nm and the H_2O broad absorption feature between $900 - 1000$ nm. These absorption features can be seen in the ASTM G-173 solar distribution spectra obtained through 1.5 air masses, which is shown as the "direct + circumsolar" curve in figure 5.3. To solve for τ_{COL}, the in-band solar flux after it has traversed the atmospheric column, denoted as F_λ, must first be determined. By integrating the ASTM G-173 "direct + circumsolar" curve between $400 - 1000$ nm, F_λ was found to be 689 W/m^2. Plugging in this value, $F_{\lambda,0} = 842$ W/m^2 found earlier, and $\mu = cos(48.2°)$, the derived in-band atmospheric opacity through one air mass is 0.20. This value was used for all opacity calculations.

5.4 Terrestrial Adaptation of Opacity Approximation Methods

Cloud opacity is calculated for the MSL observations using the variation in spectral radiance between a single cloudy region and clear sky region of the image. Therefore, the values of cloud opacity for the MSL ZMs and SHMs represent the optical depth of a specific region of cloud within the camera's FOV, which is likely representative of the the broader area within the time span of the movie. The benefit of this method is that the human operator is able to discern between clouds and other camera artifacts that populate many of the cloud images. However, an alternative method is employed here to show how the cloud opacity fluctuates over the data collection period, which is then directly compared with the lidar-derived values.

First, all cloud sequence images are converted to a radiance map by multiplying the images by the radiometric conversion factor on a pixel-by-pixel basis. An individual image from the sequence is then selected for which a region of the clear sky is visible, and a small area of this region (100×100 pixels) is averaged, and assumed to radiance of the sky. The sky radiance is subtracted from each pixel for all sequence images, thereby converting each pixel into a value of $I_{\lambda,VAR}$. The images are subsequently transformed into an optical depth map by multiplying each pixel by the remaining terms in the high cloud and whole atmosphere equations. An example of an optical depth map created using the high cloud and whole atmosphere methods for the 15th frame of the second experiment is given in figure 5.4.

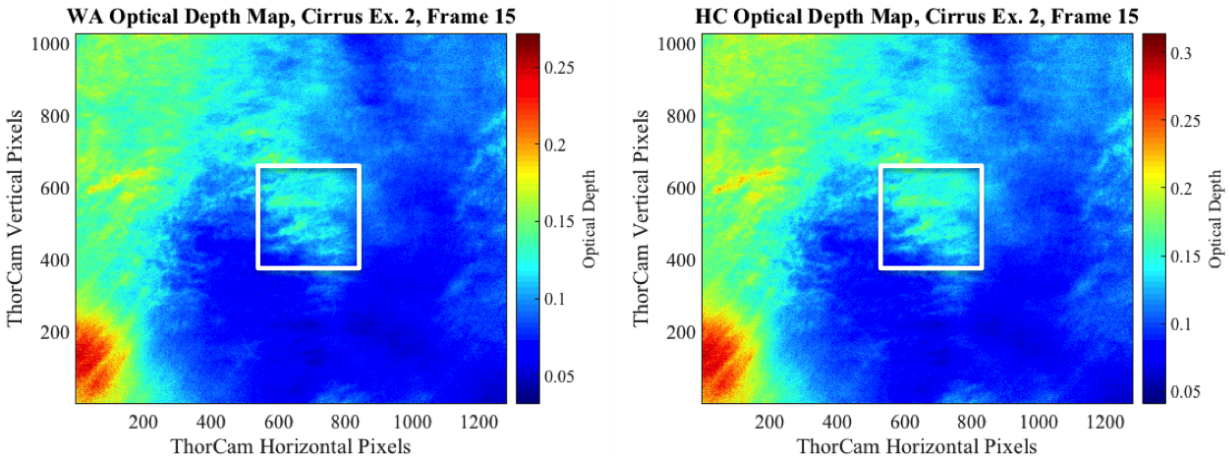

(a) (b)

Figure 5.4: (a) An optical depth map of the 15th frame of the second coordinated experiment using the whole atmosphere method. The white box shows the static region averaged for each sequence image to determine how the opacity changes over the movie span. (b) An optical depth map of the same frame calculated using the high cloud model.

To determine how the cloud opacity changes with time, a static 300×300 pixel area positioned at the image centre is averaged for each sequence image. This method was employed to show how $\Delta\tau_{HC}$ and $\Delta\tau_{WA}$ vary in time as compared to the lidar-derived value. The value of $\Delta\tau_{WA}$ is calculated and reported in the experimental results for comparative purposes only. Unlike the high cloud method, the whole atmosphere method is not suitable for water-ice clouds, it is not expected to agree with the lidar-derived values.

Chapter 6

Lidar-Coordinated Experimental Results

6.1 Cirrus Cloud Optical Depths: Lidar-dervied vs. Camera-derived

The first experiment was conducted on September 30th, 2015 at approximately 15:40 local time. The results of the lidar and camera data from this experiment are documented in figure 6.1. At the time of the experiment, cirrus clouds were scattered in the region, exhibiting a movement to the northeast. By examining the contour plot shown in the upper panel, patches of cirrus clouds are visible between $9-10.5$ km in altitude for the majority of the data collection collection period, with the exception of the final 3-4 minutes. The time-averaged vertical extinction profile shown in the lower left panel of figure 6.1 gives a clear boundary of the vertical extent of the cirrus clouds. The lidar-derived optical depth, $\Delta\tau_{LIDAR}$, as a function of time is shown in the optical depth comparison plot in the lower right panel. $\Delta\tau_{LIDAR}$ varies between 0.08 and 0.77, with an average value of $\overline{\Delta\tau}_{LIDAR} = 0.368$ for the data collection period.

In figure 6.1, a single frame from the corresponding imaging data for experiment 1 is shown as an optical depth map created using the high cloud and whole atmosphere methods. For experiment 1, $\Delta\tau_{WA}$ varies between 0.012 and 0.143, however the high cloud values are unexpectedly much lower, and range from 4.7×10^{-4} to 6.4×10^{-3}, with an average value of $\overline{\Delta\tau}_{HC} = 3.6 \times 10^{-4}$. Table 6.1 presents a summary of the lidar coordinated experiments, showing the average values for $\Delta\tau_{LIDAR}$, $\Delta\tau_{HC}$ and $\Delta\tau_{WA}$ for each experiment. Also included in table 6.1 is a ratio of the average camera-derived opacity with $\overline{\Delta\tau}_{LIDAR}$. This ratio is presented to quantitatively compare the correlation between the high cloud and whole

atmosphere opacities with the lidar values. For the first experiment, $\overline{\Delta\tau}_{HC}/\overline{\Delta\tau}_{LIDAR} = 0.0011$, suggesting a poor agreement between $\Delta\tau_{HC}$ and $\Delta\tau_{LIDAR}$. The results from this experiment are inconsistent with expected results given that $\Delta\tau_{WA}$ is considerably lower than $\Delta\tau_{HC}$ for nearly all MSL observations (see tables A.1 and A.2). This disagreement will be revisited at the end of this section.

The findings from the second experiment, documented in figure 6.2, were closer to expected results. The lidar contour plot shows three prominent cloud decks at 6.5, 7.5, and 9 km. These cloud decks are also evident in the vertical extinction profile. For this experiment, the clouds are thinner than in experiment 1, as $\Delta\tau_{LIDAR}$ varies between 0.17 and 0.25, with an average value of 0.207. As is shown in the optical depth comparison plot for figure 6.2, the camera derived values exhibit a different relative position than in the previous experiment. Here, $\Delta\tau_{HC}$ is in closer agreement with the $\Delta\tau_{LIDAR}$ as is demonstrated by higher mean ratio of 0.428, while $\Delta\tau_{WA}$ is slightly decreased, and has a marginally higher mean ratio of $\overline{\Delta\tau}_{WA}/\overline{\Delta\tau}_{LIDAR} = 0.327$. The clouds present for the third experiment, shown in figure 6.3 were similar in opacity to experiment 2, as $\overline{\Delta\tau}_{LIDAR} = 0.194$. Here, the high cloud opacity is in excellent agreement with the lidar-derived values, as $\overline{\Delta\tau}_{HC} = 0.211$, and $\overline{\Delta\tau}_{HC}/\overline{\Delta\tau}_{LIDAR}$ is 1.090. Although the whole atmosphere method was higher for this experiment, the findings are more consistent with expected results, given that $\Delta\tau_{WA}$ is lower than $\Delta\tau_{HC}$ for nearly all MSL observations.

Table 6.1: Summary table showing the average optical depth values obtained for each opacity calculation method for each lidar-coordinated experiment.

Experiment	$\overline{\Delta\tau}_{LIDAR}$	$\overline{\Delta\tau}_{HC}$	$\overline{\Delta\tau}_{HC}/\overline{\Delta\tau}_{LIDAR}$	$\overline{\Delta\tau}_{WA}$	$\overline{\Delta\tau}_{WA}/\overline{\Delta\tau}_{LIDAR}$
1	0.368	3.62e-4	0.0011	0.068	0.215
2	0.207	0.089	0.428	0.037	0.327
3	0.194	0.211	1.090	0.091	0.467
4	0.511	0.361	0.707	0.068	0.133

The atmospheric conditions of the fourth experiment were characterized by cirrostratus clouds at an altitude of $9.5 - 11$ km, as can be seen in the lidar contour plot and vertical profile in figure 6.4. The clouds present during this experiment were more opaque than in preceding experiments, as the average lidar-derived optical depth was $\overline{\Delta\tau}_{LIDAR} = 0.511$. By examining the optical depth comparison plot in figure 6.4, the values for $\Delta\tau_{HC}$ are in good agreement with $\Delta\tau_{LIDAR}$ for the first half of the experiment, however the two curves deviate in the second half of the experiment. Despite this deviation, $\overline{\Delta\tau}_{HC} = 0.361$, which is approximately 71% of the lidar-derived value, suggesting a relatively good match between these two methods. The whole atmosphere values are appreciably lower for the entire data

collection period, varying between 0.036 and 0.092. $\overline{\Delta\tau}_{WA}$ for experiment 4 is 0.068, while $\overline{\Delta\tau}_{WA}/\overline{\Delta\tau}_{LIDAR} = 0.133$, which is the lowest of all 4 experiments.

By examining $\overline{\Delta\tau}_{WA}/\overline{\Delta\tau}_{LIDAR}$ in table 6.1, it can be observed that as $\Delta\tau_{LIDAR}$ increases, $\overline{\Delta\tau}_{WA}/\overline{\Delta\tau}_{LIDAR}$ decreases. During experiments 2 and 3, for which $\Delta\tau_{LIDAR}$ is approximately 0.2, $\overline{\Delta\tau}_{WA}/\overline{\Delta\tau}_{LIDAR}$ is greatest, and ranges between 0.327 and 0.427. However, as the opacity increases to $\Delta\tau_{LIDAR} = 0.511$ in the fourth experiment, which is more than double that measured in experiments 2 and 3, $\overline{\Delta\tau}_{WA}/\overline{\Delta\tau}_{LIDAR}$ decreases to 0.133. The anti-correlation between $\Delta\tau_{WA}$ and $\Delta\tau_{LIDAR}$ can be attributed to assumptions regarding the scattering properties for the whole atmosphere method, and is expected given that the whole atmosphere method is not appropriate for water-ice clouds.

The opacity values reported for $\Delta\tau_{WA}$ and $\Delta\tau_{HC}$ in experiment 1 are inconsistent with expected values, as well other measurements obtained from the subsequent experiments. It is suspected that the anomalous results from experiment 1 are due to an inadvertent adjustment to the aperture of the camera during the experimental set up. As this aperture adjustment was unintentional, its setting was not documented in the lab notes and was unaccounted for in the calibration. If the aperture was partially closed, the measured radiance values of the camera image would be reduced relative to their true values, which would lead to smaller values of opacity. In theory, as $\Delta\tau_{WA}$ relies on a fractional radiance between $I_{\lambda,VAR}$ and $I_{\lambda,MEAN}$, it should be unaffected by the change in aperture. However, given that $\Delta\tau_{HC}$ depends on absolute radiance measurements ($I_{\lambda,VAR}$), a change in the aperture that is unaccounted for in the calibration would lead to erroneous opacity measurements.

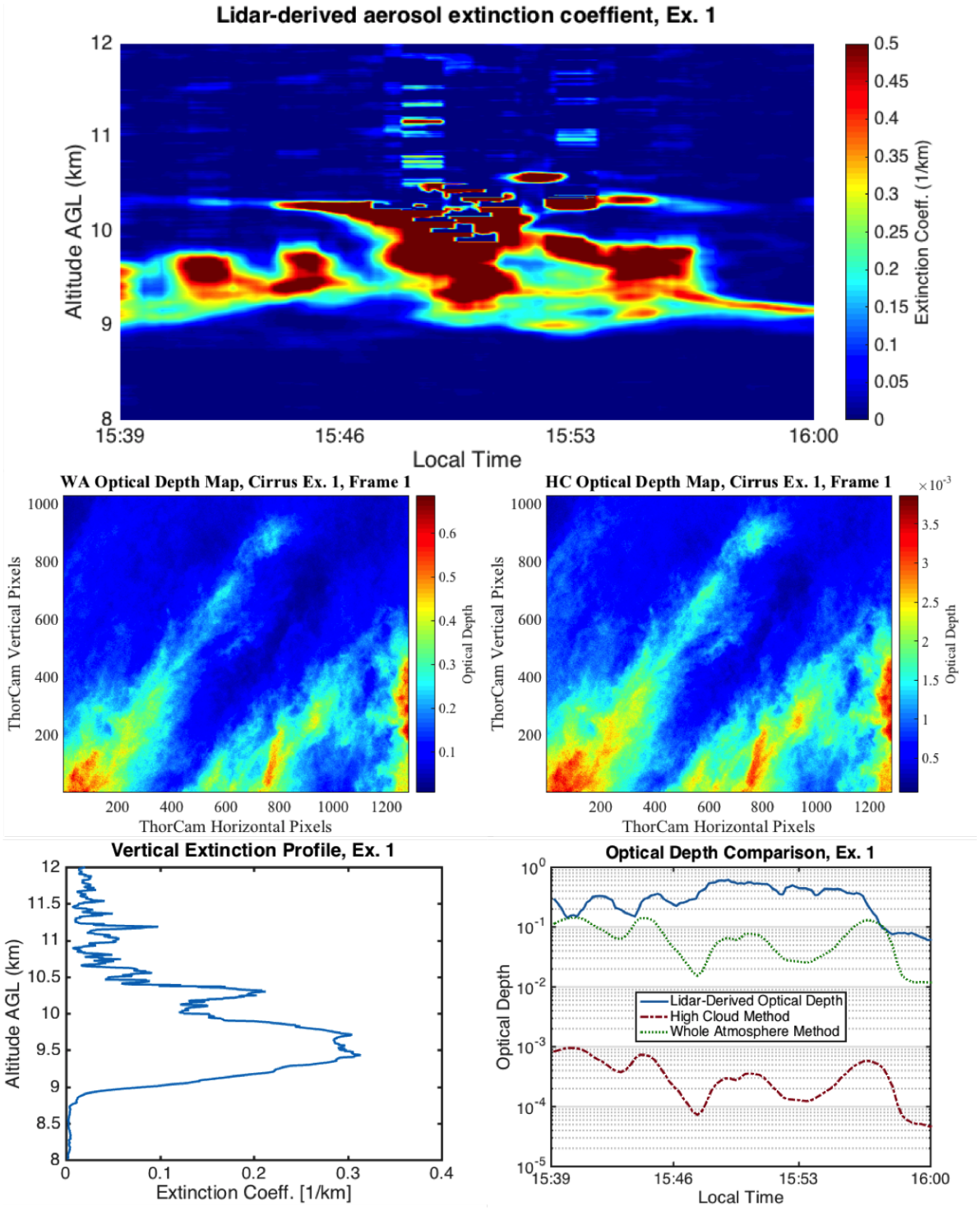

Figure 6.1: Top: Lidar contour map showing the altitude (y-axis) and the aerosol extinction coefficient (colour axis) vs. time (x-axis). Middle left: HC Optical depth map of frame number 1. Middle right: WA Optical depth map of frame number 1. Bottom left: Time-averaged vertical extinction profile showing a primary cloud deck at 9.5 km. Bottom right: cirrus cloud optical depth derived using the HC method, WA method and the York U lidar instrument. The first experiment is anomalous, and it is suspected that the aperture was partially closed inadvertently.

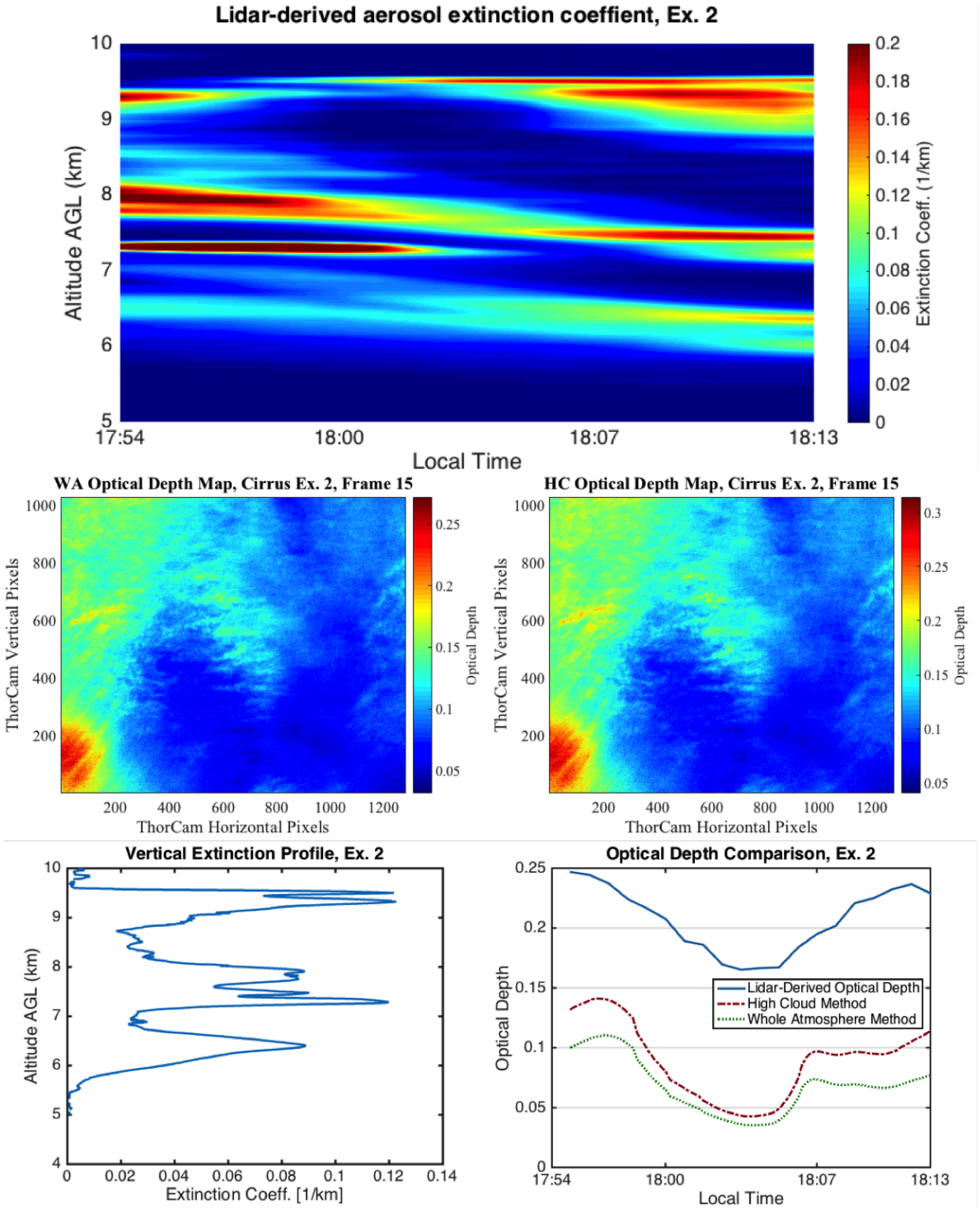

Figure 6.2: A summary of the lidar and camera data collected for the second coordinated experiment on May 5, 2016. See figure caption 6.1 for a description of the layout. For this experiment, $\overline{\Delta\tau}_{LIDAR} = 0.207$, $\overline{\Delta\tau}_{HC} = 0.089$, $\overline{\Delta\tau}_{WA} = 0.037$.

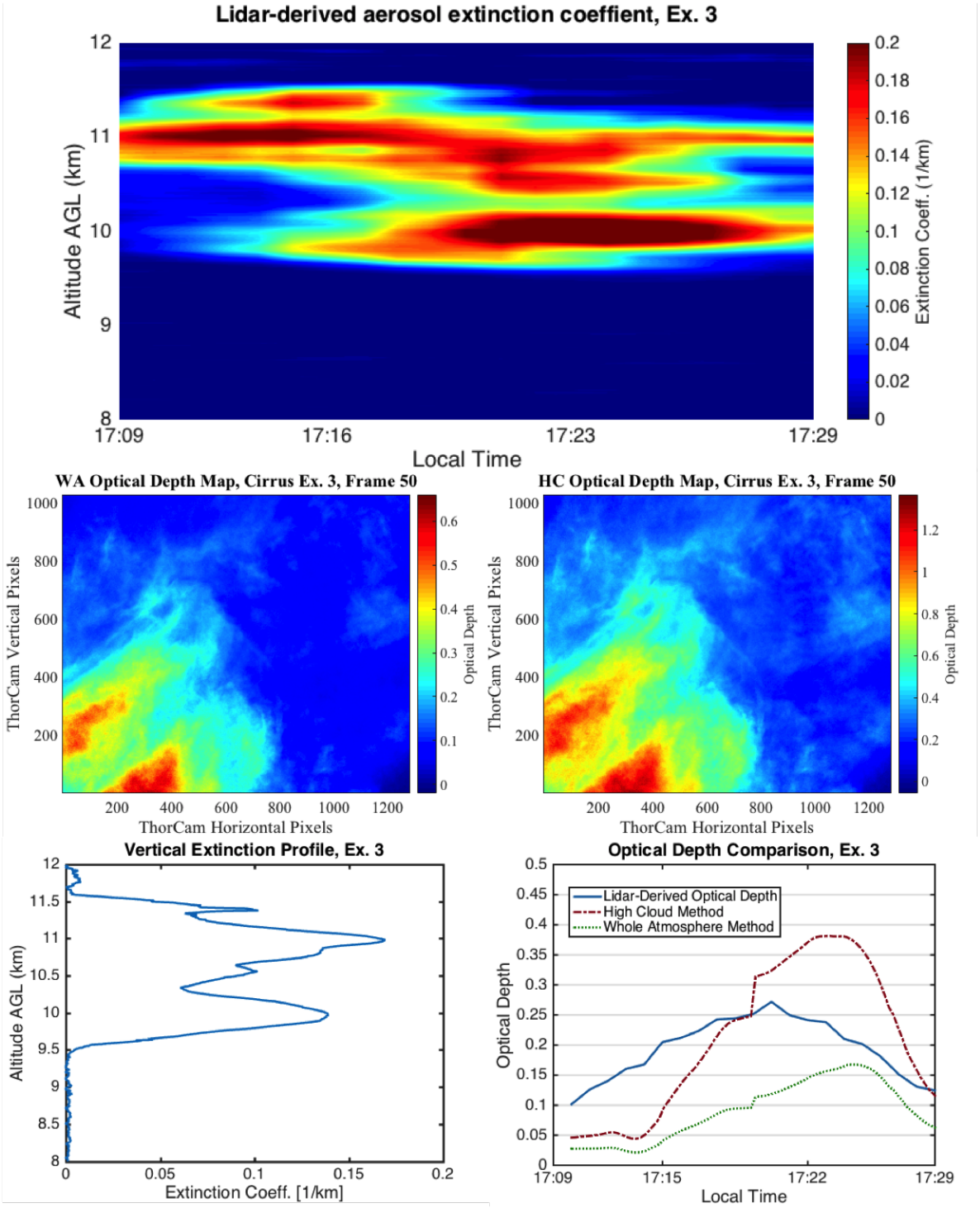

Figure 6.3: A summary of the lidar and camera data collected for the second coordinated experiment on May 11, 2016. See figure caption 6.1 for a description of the layout. For this experiment, $\overline{\Delta\tau}_{LIDAR} = 0.194$, $\overline{\Delta\tau}_{HC} = 0.211$, $\overline{\Delta\tau}_{WA} = 0.091$.

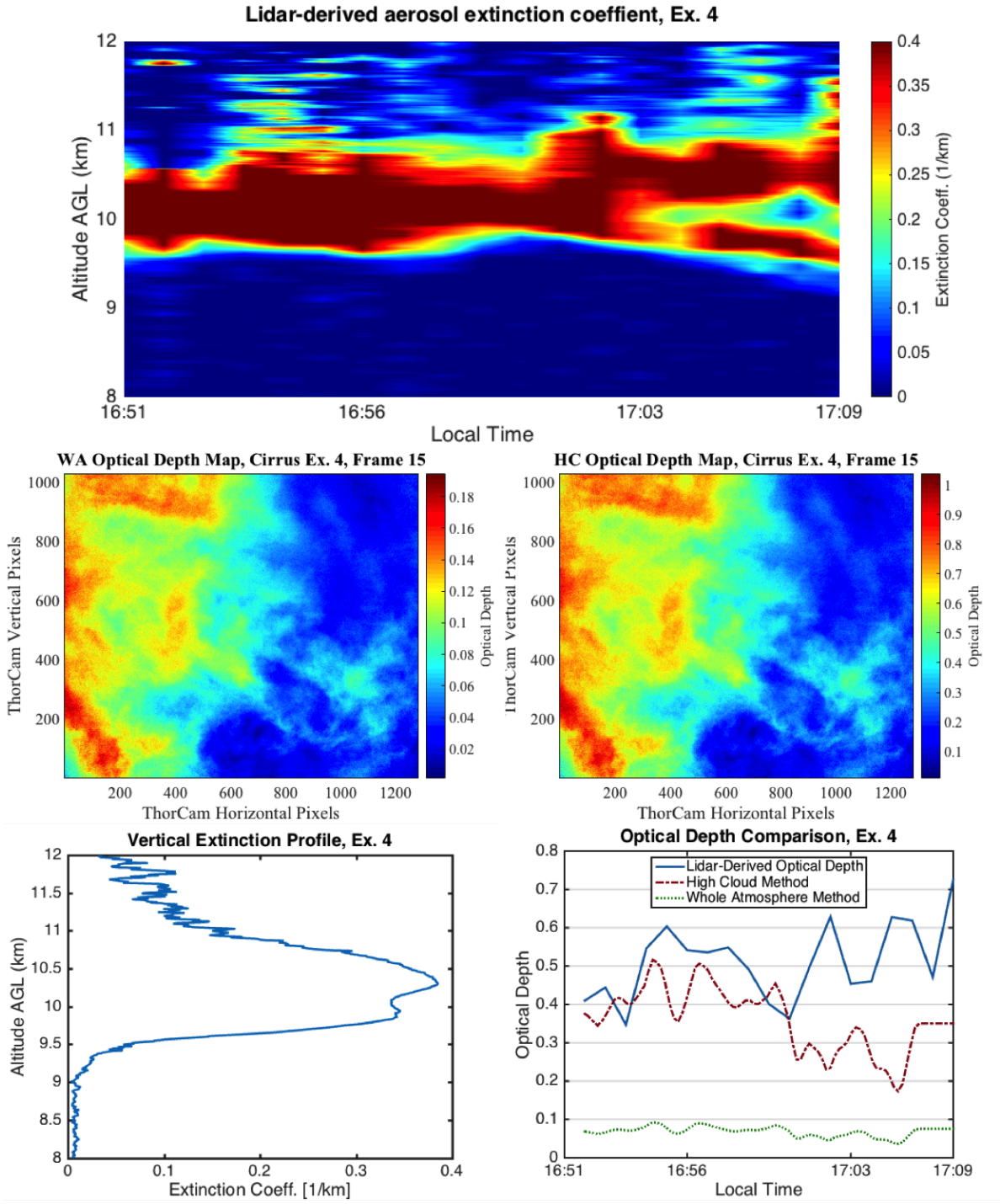

Figure 6.4: A summary of the lidar and camera data collected for the second coordinated experiment on June 1, 2016. See figure caption 6.1 for a description of the layout. For this experiment, $\overline{\Delta\tau}_{LIDAR} = 0.511$, $\overline{\Delta\tau}_{HC} = 0.361$, $\overline{\Delta\tau}_{WA} = 0.068$.

6.2 Observations of Sub-visual Terrestrial Cirrus Clouds

In addition to the lidar-coordinated experiments, further analysis was conducted to understand how sub-visual water-ice clouds, such as those seen in the MSL movies, would appear on Earth after the mean frame subtraction technique. On May 6, 2016, a series of filtered and unfiltered Zenith Movies were collected at the York University campus using the ThorCam and a set of laser line filters. A separate filtered ZM was collected at 400 nm, 450 nm, 500 nm, 550 nm, 600 nm, 650 nm, 700 nm, 750 nm and 800 nm. A description of the filter set, including transmission data from the manufacturer as well as UV and NIR spectrometer measurements are shown in appendix B.2.5.

The sky directly above the university at the time of imaging was entirely clear, however distant cirrus clouds could be observed in the east. The filtered ZMs were collected using an identical frame rate as the MSL long span observations, with one image captured every 38 seconds. The movies were then processed in the exact same way as the MSL observations using the mean frame subtraction.

Five perturbation images from the 650 nm, 700 nm, 750 nm filtered sequences are documented in figure 6.5, along with the sol 509 ZM for visual comparison. These filters are shown as they are within the spectral range of the MSL NavCam, although this is somewhat arbitrary as clouds are spectrally neutral in the visible/NIR region of the spectrum. The cloud features present in the filtered observations appear consistent in angular size, shape and brightness between each filter acquired. In each of the filtered sequences shown in figure 6.5, the terrestrial cloud features bear a stunning resemblance to a large majority of the Martian cloud features in the MSL NavCam movies, such as the large clouds in the sol 193 ZM (figure 4.1b). In each sequence, clouds cannot be observed in raw images, but are clearly visible in the perturbation images.

The optical depth was calculated for each filtered image sequence using the high cloud model and the method described for the MSL observations. The variation in spectral radiance was found between the cloud and the sky, and the solar flux and atmospheric opacity was determined for each wavelength using the ASTM G-173 reference spectra. The values of $\Delta\tau_{HC}$ and $\Delta\tau_{WA}$ are plotted with their 95% confidence interval in figure 6.6.

For $\Delta\tau_{HC}$, the calculated values range between 0.006 and 0.08, with an average opacity of 0.04. The calculated values here are consistent with the values reported by MSL from the ZMs and SHMs during aphelion season. Given that the filtered observations were acquired sequentially, and thus are not imaging the same portion of the sky in time, subtle changes in cloud opacity are expected for each filter sequence. The calculated values of $\Delta\tau_{WA}$ are consistently lower, ranging between 6×10^{-4} and 0.01.

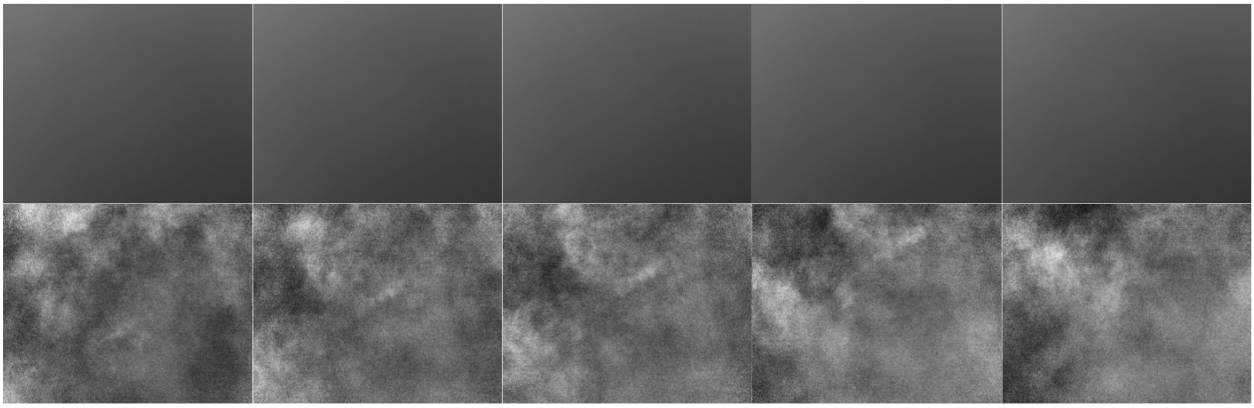

(a) 650 nm filter

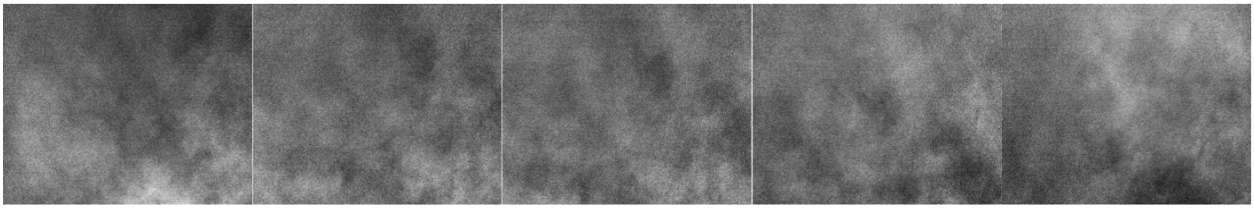

(b) 700 nm filter

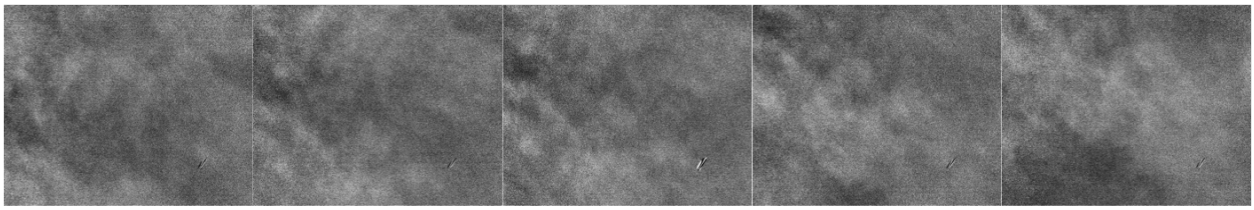

(c) 750 nm filter

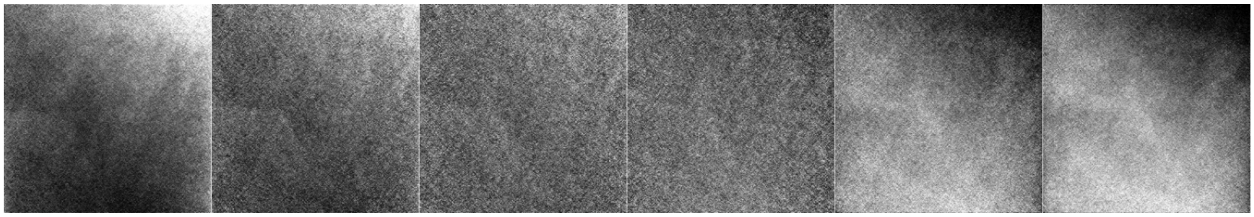

(d) Sol 509 ZM

Figure 6.5: (a) 5 frames from a terrestrial cloud sequence using a 650 nm filter showing raw unprocessed frames (top) along with mean frame subtracted images (bottom). (b) 5 mean frame subtracted images frames using 700 nm filter (c) 5 mean frame subtracted images using 750 nm filter. (d) 6 mean frame subtracted frames from the sol 509 ZM for which a similar cloud opacity was measured.

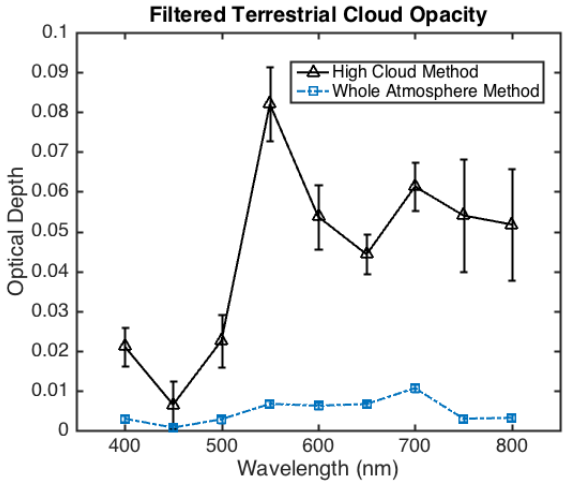

Figure 6.6: Opacity of terrestrial sub-optical water-ice clouds derived using the high cloud model and whole atmosphere model presented with the 95% confidence interval. For the high cloud model, the values are consistent with those reported by MSL from the ZMs and SHMs during aphelion season.

Chapter 7

Conclusion

Over the course of the first two Martian years of the MSL mission, 233 Zenith Movies and 272 Supra-Horizon Movies were acquired to characterize the cloud activity at Gale Crater, Mars. The clouds observed are suggestive of diffuse water-ice clouds during the aphelion season, given their seasonal occurrence and regular spacing. Seasonal variation is observed in both the Zenith and Supra-Horizon Movie data sets, with enhanced cloud activity occurring between $L_S = 0^\circ - 180^\circ$ of MY 32 and 33, corresponding to autumn and winter in the southern hemisphere. The seasonality is well correlated with orbital observations from MARCI, which report high altitude equatorial clouds throughout $L_S = 10^\circ - 172^\circ$ of MY 32 and $L_S = 42^\circ - 146^\circ$ of MY 33. The mean frame subtraction technique applied to the MSL sequences allows for the detection of optically thin clouds that cannot be observed from orbit, which explains the broader seasonality of the ZMs and SHMs.

Using the high cloud opacity method developed by Moores et al. (2015a), the optical depth range for the MSL clouds is $\Delta\tau_{HC} = 0.007 - 0.245$, with an average value of 0.045. In MY 32 and 33, the peak in cloud opacity occurs between $L_S = 60^\circ - 120^\circ$, which corresponds to the time of year when the aphelion cloud belt is present at equatorial latitudes. Additionally, 12 water-ice profiles were collected near Gale Crater from MCS throughout the $L_S = 9^\circ - 161^\circ$ of MY 32. These opacity retrievals show a primary cloud deck at approximately 30 km in altitude, with optical depths that are in agreement with the high cloud model, ranging between 0.04 and 0.15. The average spacing for the clouds apparent over the study period was found to be 5.5°, corresponding to a distance of 2.9 km assuming a cloud base of 30 km.

Preliminary analysis is presented in an effort to restrict the phase function of the Martian clouds by using MCS water-ice opacity retrievals and spectral radiance measurements from the NavCam movies. This analysis is achieved by rearranging the high cloud model to solve for the phase function. The initial results indicate that the Martian clouds do not

deviate in ice-crystal make up from the cirrus clouds on Earth according to laboratory-derived scattering phase functions of 14 different ice crystals shapes Chepfer et al. (2002). Only the spheres were tentatively eliminated, however further investigation is needed.

On sol 594 of the mission, the Supra-Horizon Movie was altered in an effort to enhance the science return of the observation. The new observation consisted of a different aspect ratio, shorter time span, and reduced frame number. The new SHM was able to provide information on dust levels within the crater; however, the new observation did not prove useful for detecting clouds. Separate tests showed that the shortened time span was responsible for the featureless Supra-Horizon Movies from sol $594 - 910$. Further analysis using synthetic data was performed to determine the numeric threshold for the minimum time span needed to detect clouds within the atmospheric movies. This test showed that the time span required to detect clouds using the mean frame subtraction technique was one that allowed the clouds to translate one wavelength over the course of the movie span. To correct the issue of the featureless SHMs, a long span SHM was implemented on sol 911, which has since captured a number of interesting cloud formations, such as the prominent gravitational waves detected on sol 1302.

Finally, to validate the cloud opacity measurements from Moores et al. (2015a) and Kloos et al. (2016), the high cloud method was tested by imaging terrestrial cirrus clouds, and comparing it with contemporaneous lidar measurements. The high cloud method was found to produce opacity values that were lower than expected, however, the high cloud values were, on average, within 40% of the lidar-derived measurement, excluding the first experiment. More data is needed to refine the accuracy of the high cloud method, however the initial experimental results indicate that the assumptions implicit in the equation are justified.

Bibliography

Andrews, David G, James R Holton, and Conway B Leovy (1987). *Middle atmosphere dynamics*. Vol. 40. Academic press.

Audouard, J, S Piqueux, F Poulet, M Vincendon, and B Gondet (2015). "Analysis of Curiosity surface temperature Data". In: *European Planetary Science Congress 2015, held 27 September-2 October, 2015 in Nantes, France, Online at http://meetingorganizer. copernicus. org/EPSC2015, id. EPSC2015-300*. Vol. 10, p. 300.

Benson, Jennifer L, Boncho P Bonev, Philip B James, Kathy J Shan, Bruce A Cantor, and Michael A Caplinger (2003). "The seasonal behavior of water ice clouds in the Tharsis and Valles Marineris regions of Mars: Mars Orbiter Camera observations". In: *Icarus* 165.1, pp. 34–52.

Chepfer, H., P. Minnis, D. Young, and L. Nguyen (2002). "Estimation of cirrus cloud effective ice crystal shapes using visible reflectances from dual-satellite measurments". In: *Journal of Geophysical Resarch* 107.D23, p. 4730.

Clancy, R Todd, Michael J Wolff, and Philip R Christensen (2003). "Mars aerosol studies with the MGS TES emission phase function observations: Optical depths, particle sizes, and ice cloud types versus latitude and solar longitude". In: *Journal of Geophysical Research: Planets* 108.E9.

Clancy, RT, BJ Sandor, MJ Wolff, PR Christensen, MD Smith, JC Pearl, BJ Conrath, and RJ Wilson (2000). "An intercomparison of ground-based millimeter, MGS TES, and Viking atmospheric temperature measurements: Seasonal and interannual variability of temperatures and dust loading in the global Mars atmosphere". In: *Journal of Geophysical Research: Planets* 105.E4, pp. 9553–9571.

Clancy, RT, AW Grossman, MJ Wolff, PB James, DJ Rudy, YN Billawala, BJ Sandor, SW Lee, and DO Muhleman (1996). "Water vapor saturation at low altitudes around Mars aphelion: a key to Mars climate?" In: *Icarus* 122.1, pp. 36–62.

Curran, Robert J, Barney J Conrath, Rudolf A Hanel, Virgil G Kunde, and JC Rearl (1973). "Mars: Mariner 9 spectroscopic evidence for H2O ice clouds". In: *Science* 182.4110, pp. 381–383.

Dickinson, C, JA Whiteway, L Komguem, JE Moores, and MT Lemmon (2010). "Lidar measurements of clouds in the planetary boundary layer on Mars". In: *Geophysical Research Letters* 37.18.

Gómez-Elvira, J, C Armiens, L Castañer, M Domínguez, M Genzer, Francisco Gómez, R Haberle, A-M Harri, V Jiménez, H Kahanpää, et al. (2012). "REMS: The environmental sensor suite for the Mars Science Laboratory rover". In: *Space science reviews* 170.1-4, pp. 583–640.

Grotzinger, John P, Joy Crisp, Ashwin R Vasavada, Robert C Anderson, Charles J Baker, Robert Barry, David F Blake, Pamela Conrad, Kenneth S Edgett, Bobak Ferdowski, et al. (2012). "Mars Science Laboratory mission and science investigation". In: *Space science reviews* 170.1-4, pp. 5–56.

Hale, A Snyder, LK Tamppari, DS Bass, and MD Smith (2011). "Martian water ice clouds: A view from Mars Global Surveyor Thermal Emission Spectrometer". In: *Journal of Geophysical Research: Planets* 116.E4.

Hinson, DP and RJ Wilson (2004). "Temperature inversions, thermal tides, and water ice clouds in the Martian tropics". In: *Journal of Geophysical Research: Planets* 109.E1.

Jakosky, Bruce M and Crofton B Farmer (1982). "The seasonal and global behavior of water vapor in the Mars atmosphere: Complete global results of the Viking atmospheric water detector experiment". In: *Journal of Geophysical Research: Solid Earth* 87.B4, pp. 2999–3019.

Kleinböhl, Armin, John T Schofield, David M Kass, Wedad A Abdou, Charles R Backus, Bhaswar Sen, James H Shirley, W Gregory Lawson, Mark I Richardson, Fredric W Taylor, et al. (2009). "Mars Climate Sounder limb profile retrieval of atmospheric temperature, pressure, and dust and water ice opacity". In: *Journal of Geophysical Research: Planets* 114.E10.

Kloos, Jacob L, John E Moores, Mark Lemmon, David Kass, Raymond Francis, Manuel de la Torre Juárez, María-Paz Zorzano, and F Javier Martín-Torres (2016). "The first Martian year of cloud activity from Mars Science Laboratory (sol 0–800)". In: *Advances in Space Research* 57.5, pp. 1223–1240.

Komguem, L, JA Whiteway, C Dickinson, M Daly, and MT Lemmon (2013). "Phoenix LIDAR measurements of Mars atmospheric dust". In: *Icarus* 223.2, pp. 649–653.

Lemmon, MT (2014). "The Mars science laboratory optical depth record". In: *LPI Contributions* 1791, p. 1338.

Leovy, CB, GA Briggs, and BA Smith (1973). "Mars atmosphere during the Mariner 9 extended mission: Television results". In: *Journal of Geophysical Research* 78.20, pp. 4252–4266.

Liou, K.N. (2002). "An Introduction to Atmospheric Radiation". In: *Academic Press* ISBN 0-12-451451-0.

— (1992). *Radiation and Cloud Processes in the Atmosphere: Theory, Observation and Modeling.* ISBN 0-19-504910-1. New York, NY: Oxford University Press.

Madeleine, J-B, Francois Forget, Aymeric Spiga, Michael J Wolff, Franck Montmessin, Mathieu Vincendon, Denis Jouglet, Brigitte Gondet, J-P Bibring, Yves Langevin, et al. (2012). "Aphelion water-ice cloud mapping and property retrieval using the OMEGA imaging spectrometer onboard Mars Express". In: *Journal of Geophysical Research: Planets* 117.E11.

Maki, J, D Thiessen, A Pourangi, P Kobzeff, T Litwin, L Scherr, S Elliott, A Dingizian, and M Maimone (2012). "The Mars science laboratory engineering cameras". In: *Space science reviews* 170.1-4, pp. 77–93.

Malin, M. C., B. A. Cantor, A. W. Britton, and M. R. Wu (2015). "MRO MARCI Weather Report for the week of 14 September 2015 – 20 September 2015, Malin Space Science Systems Captioned Image Release, MSSS-393". In:

— (2013). "MRO MARCI Weather Report for the week of 19 August 2013 – 25 August 2013, Malin Space Science Systems Captioned Image Release, MSSS-288". In:

— (2016). "MRO MARCI Weather Report for the week of 25 April 2016 – 1 May 2016, Malin Space Science Systems Captioned Image Release, MSSS-426". In:

Malin, M. C., B.A. Cantor, M. R. Wu, and L. M. Saper (2014a). "MRO MARCI Weather Report for the week of 4 August 2014 – 10 August 2014". In:

Malin, M. C., B. A. Cantor, A. W. Britton, and M. R. Wu (2014b). "MRO MARCI Weather Report for the week of 4 August 2014 – 10 August 2014, Malin Space Science Systems Captioned Image Release, MSSS-338," in:

Mateshvili, Nina, Didier Fussen, Filip Vanhellemont, Christine Bingen, Jan Dodion, Franck Montmessin, Severine Perrier, Emmanuel Dimarellis, and Jean-Loup Bertaux (2007). "Martian ice cloud distribution obtained from SPICAM nadir UV measurements". In: *Journal of Geophysical Research: Planets* 112.E7.

Montmessin, Franck, RM Haberle, F Forget, Y Langevin, RT Clancy, and J-P Bibring (2007). "On the origin of perennial water ice at the south pole of Mars: A precession-controlled mechanism?" In: *Journal of Geophysical Research: Planets* 112.E8.

Montmessin, Franck, F Forget, P Rannou, M Cabane, and RM Haberle (2004). "Origin and role of water ice clouds in the Martian water cycle as inferred from a general circulation model". In: *Journal of Geophysical Research: Planets* 109.E10.

Moore, Casey A, John E Moores, Mark T Lemmon, Scot CR Rafkin, Raymond Francis, Jorge Pla-García, Robert M Haberle, María-Paz Zorzano, F Javier Martín-Torres, John

R Burton, et al. (2016). "A full martian year of line-of-sight extinction within Gale Crater, Mars as acquired by the MSL Navcam through sol 900". In: *Icarus* 264, pp. 102–108.

Moores, John E, Mark T Lemmon, Peter H Smith, Leonce Komguem, and James A Whiteway (2010). "Atmospheric dynamics at the Phoenix landing site as seen by the Surface Stereo Imager". In: *Journal of Geophysical Research: Planets* 115.E1.

Moores, John E, Mark T Lemmon, Scot CR Rafkin, Raymond Francis, Jorge Pla-Garcia, Manuel De La Torre Juárez, Keri Bean, David Kass, Robert Haberle, Claire Newman, et al. (2015a). "Atmospheric movies acquired at the Mars Science Laboratory landing site: Cloud morphology, frequency and significance to the Gale Crater water cycle and Phoenix mission results". In: *Advances in Space Research* 55.9, pp. 2217–2238.

Moores, John E, Mark T Lemmon, Henrik Kahanpää, Scot CR Rafkin, Raymond Francis, Jorge Pla-Garcia, Keri Bean, Robert Haberle, Claire Newman, Michael Mischna, et al. (2015b). "Observational evidence of a suppressed planetary boundary layer in northern Gale Crater, Mars as seen by the Navcam instrument onboard the Mars Science Laboratory rover". In: *Icarus* 249, pp. 129–142.

Peale, SJ (1973). "Water and the Martian W cloud". In: *Icarus* 18.3, pp. 497–501.

Pla-García, J and S Rafkin (2015). "Meteorological Circulations at Gale Environment Through Rover Environmental Monitoring Station (REMS) Observations and Mesoscale Modeling (MRAMS)". In: *European Planetary Science Congress 2015, held 27 September-2 October, 2015 in Nantes, France, Online at http://meetingorganizer. copernicus. org/EPSC2015, id. EPSC2015-103*. Vol. 10, p. 103.

Popovici, Vlad (2012). *Atmospheric Lidar Measurements on Earth and Mars*. Library and Archives Canada= Bibliothèque et Archives Canada.

Read, Peter and Stephen Lewis (2004). *The Martian Climate Revisited - Atmosphere and Environment of a Desert Planet*. Springer.

Richardson, Mark I, R John Wilson, and Alexander V Rodin (2002). "Water ice clouds in the Martian atmosphere: General circulation model experiments with a simple cloud scheme". In: *Journal of Geophysical Research: Planets* 107.E9.

Sassen, Kenneth and Byung Sung Cho (1992). "Subvisual-thin cirrus lidar dataset for satellite verification and climatological research". In: *Journal of Applied Meteorology* 31.11, pp. 1275–1285.

Savijärvi, HI, A-M Harri, and O Kemppinen (2015). "Mars Science Laboratory diurnal moisture observations and column simulations". In: *Journal of Geophysical Research: Planets* 120.5, pp. 1011–1021.

Smith, Michael D, Joshua L Bandfield, Philip R Christensen, and Mark I Richardson (2003). "Thermal Emission Imaging System (THEMIS) infrared observations of atmospheric dust and water ice cloud optical depth". In: *Journal of Geophysical Research: Planets* 108.E11.

Smith, SA and BA Smith (1972). "Diurnal and seasonal behavior of discrete white clouds on Mars". In: *Icarus* 16.3, pp. 509–521.

Trokhimovskiy, Alexander, Anna Fedorova, Oleg Korablev, Franck Montmessin, Jean-Loup Bertaux, Alexander Rodin, and Michael D Smith (2015). "Mars? water vapor mapping by the SPICAM IR spectrometer: Five martian years of observations". In: *Icarus* 251, pp. 50–64.

Vasavada, AR, JP Grotzinger, RE Arvidson, FJ Calef, JA Crisp, S Gupta, J Hurowitz, N Mangold, S Maurice, ME Schmidt, et al. (2014). "Overview of the Mars Science Laboratory mission: Bradbury landing to Yellowknife Bay and beyond". In: *Journal of Geophysical Research: Planets* 119.6, pp. 1134–1161.

Vasavade, Ashwin. *Science Goals*. URL: `https://msl-scicorner.jpl.nasa.gov/ScienceGoals/` (visited on 2012).

Wang, Huiqun and Andrew P Ingersoll (2002). "Martian clouds observed by Mars Global Surveyor Mars Orbiter Camera". In: *Journal of Geophysical Research: Planets* 107.E10.

Welch, Peter D (1967). "The use of fast Fourier transform for the estimation of power spectra: A method based on time averaging over short, modified periodograms". In: *IEEE Transactions on audio and electroacoustics* 15.2, pp. 70–73.

Whiteway, JA, L Komguem, C Dickinson, C Cook, M Illnicki, J Seabrook, V Popovici, TJ Duck, R Davy, PA Taylor, et al. (2009). "Mars water-ice clouds and precipitation". In: *Science* 325.5936, pp. 68–70.

Whiteway, James, Michael Daly, Allan Carswell, Thomas Duck, Cameron Dickinson, Leonce Komguem, and Clive Cook (2008). "Lidar on the Phoenix mission to Mars". In: *Journal of Geophysical Research: Planets* 113.E3.

Wilson, R John, Gregory A Neumann, and Michael D Smith (2007). "Diurnal variation and radiative influence of Martian water ice clouds". In: *Geophysical research letters* 34.2.

Wolff, Michael J, James F Bell, Philip B James, R Todd Clancy, and Steven W Lee (1999). "Hubble Space Telescope observations of the Martian aphelion cloud belt prior to the Pathfinder Mission: Seasonal and interannual variations". In: *Journal of Geophysical Research: Planets* 104.E4, pp. 9027–9041.

Wolff, MJ, RT Clancy, D Banfield, and K Cuozzo (2005). "Water ice clouds as seen from the Mars Exploration Rovers". In: *AGU Fall Meeting Abstracts*.

Appendix A

MSL Atmospheric Movie Summary Tables

Table A.1: Zenith Movie summary table.

Sol	**LTST**	L_S	**Qual.**	τ_{HC}	$\pm 95\%$	τ_{WA}	$\pm 95\%$	λ_{CHAR}
14	16:24	157.9	4	**0.016**	**0.0045**	0.040	0.0116	6.14
24	15:35	163.2	4	**0.048**	**0.0123**	0.096	0.0246	7.89
39	16:21	172.1	5	**0.041**	**0.0071**	0.004	0.0007	3.68
49	16:40	177.7	5	**0.042**	**0.0045**	0.008	0.0008	2.76
54	15:54	180.6	4	**0.052**	**0.0086**	0.004	0.0007	3.68
56	16:05	181.8	3	**0.035**	**0.0152**	0.082	0.0354	3.68
70	16:49	190.0	1	**0.018**	**0.0070**	0.002	0.0008	2.76
78	15:36	194.8	0	**0.050**	**0.0117**	0.003	0.0007	3.68
100	15:13	208.3	3	0.203	0.0315	**0.011**	**0.0017**	5.52
170	17:57	253.3	4	0.016	0.0041	**0.009**	**0.0024**	2.76
183	15:51	261.8	2	0.059	0.0171	**0.005**	**0.0015**	6.50
186	14:49	263.7	2	0.074	0.0189	**0.004**	**0.0011**	6.14
193	09:23	268.1	4	0.182	0.0143	**0.016**	**0.0013**	11.04
198	08:48	271.3	3	0.106	0.0179	**0.007**	**0.0012**	5.52
300	14:14	333.4	2	0.081	0.0270	**0.004**	**0.0012**	6.14
310	17:53	339.0	3	0.008	0.0023	**0.006**	**0.0017**	3.07
314	14:45	341.1	2	0.050	0.0205	**0.003**	**0.0012**	3.68
316	15:49	342.2	2	0.020	0.0109	**0.002**	**0.0011**	6.90
332	16:50	350.9	2	0.011	0.0070	**0.002**	**0.0011**	3.68
357	17:15	3.8	4	0.019	0.0044	**0.004**	**0.0010**	2.51
363	17:38	6.8	5	0.009	0.0028	**0.003**	**0.0010**	2.64

383	17:04	16.6	1	**0.014**	**0.0034**	0.003	0.0006	2.36
424	16:17	36.1	1	**0.008**	**0.0049**	0.001	0.0006	4.99
429	16:27	38.5	8	**0.176**	**0.0043**	0.023	0.0006	3.68
432	16:43	39.9	3	**0.013**	**0.0030**	0.002	0.0005	2.02
443	15:16	44.9	1	**0.026**	**0.0043**	0.002	0.0003	5.02
453	15:55	49.5	3	**0.010**	**0.0053**	0.001	0.0006	4.60
486	16:14	64.4	1	**0.022**	**0.0024**	0.003	0.0004	5.52
493	07:33	67.4	1	**0.024**	**0.0027**	0.004	0.0004	5.02
502	16:12	71.6	2	**0.033**	**0.0026**	0.005	0.0004	5.52
504	16:20	72.5	2	**0.036**	**0.0025**	0.006	0.0004	3.94
507	15:49	73.8	1	**0.020**	**0.0036**	0.003	0.0004	5.02
513	14:56	76.5	4	**0.051**	**0.0038**	0.005	0.0004	5.52
517	12:31	78.3	1	**0.037**	**0.0104**	0.002	0.0004	7.89
522	15:38	80.6	2	**0.017**	**0.0034**	0.001	0.0003	4.60
525	15:25	81.9	4	**0.057**	**0.0028**	0.007	0.0003	3.68
528	15:34	83.2	3	**0.038**	**0.0028**	0.005	0.0004	7.89
541	16:24	89.1	3	**0.020**	**0.0023**	0.004	0.0004	5.02
543	07:16	89.9	4	**0.027**	**0.0023**	0.006	0.0005	3.68
550	16:08	93.2	2	**0.034**	**0.0023**	0.006	0.0004	2.76
561	15:22	98.2	3	**0.014**	**0.0036**	0.002	0.0005	5.52
562	14:49	98.7	5	**0.054**	**0.0035**	0.006	0.0004	4.60
574	16:13	104.2	3	**0.011**	**0.0024**	0.002	0.0004	3.07
581	15:45	107.5	4	**0.037**	**0.0025**	0.006	0.0004	3.25
588	16:19	110.7	2	**0.026**	**0.0020**	0.005	0.0004	4.60
593	16:24	113.1	3	**0.019**	**0.0019**	0.003	0.0003	3.94
603	15:42	117.8	4	**0.037**	**0.0025**	0.005	0.0004	5.02
612	16:05	122.2	3	**0.030**	**0.0023**	0.005	0.0004	4.60
630	14:39	131.0	4	**0.019**	**0.0053**	0.002	0.0004	4.60
636	16:02	134.0	3	**0.019**	**0.0026**	0.003	0.0004	4.60
638	15:20	135.0	3	**0.012**	**0.0031**	0.001	0.0003	7.89
654	15:07	143.1	2	**0.023**	**0.0219**	0.002	0.0020	5.02
663	16:36	147.8	3	**0.019**	**0.0058**	0.004	0.0011	3.25
669	15:19	150.9	4	**0.068**	**0.0134**	0.005	0.0010	5.52
670	15:42	151.4	4	**0.030**	**0.0096**	0.003	0.0010	6.14
671	15:04	152.0	4	**0.032**	**0.0107**	0.003	0.0009	6.14
701	15:25	168.3	4	**0.047**	**0.0145**	0.004	0.0011	5.52
703	17:37	169.4	1	**0.017**	**0.0026**	0.003	0.0005	2.51
785	16:03	218.6	2	0.099	0.0261	**0.008**	**0.0020**	4.08
834	15:24	250.3	3	0.073	0.0209	**0.004**	**0.0012**	4.99
886	15:14	283.9	1	0.041	0.0154	**0.005**	**0.0020**	6.90
892	07:07	287.7	1	0.037	0.0076	**0.007**	**0.0015**	6.42

904	15:39	295.2	1	0.061	0.0104	**0.005**	**0.0009**	7.49
915	17:14	302.0	1	0.021	0.0041	**0.005**	**0.0009**	5.61
924	07:48	307.5	2	0.067	0.0105	**0.007**	**0.0011**	4.99
925	07:48	308.1	2	0.139	0.0095	**0.015**	**0.0010**	3.46
927	15:55	309.3	2	0.075	0.0067	**0.008**	**0.0007**	4.99
931	07:51	311.7	1	0.048	0.0081	**0.005**	**0.0008**	4.49
947	06:44	321.1	1	0.018	0.0055	**0.004**	**0.0011**	2.01
951	15:11	323.4	1	0.023	0.0106	**0.002**	**0.0008**	4.99
963	15:15	330.3	1	0.060	0.0116	**0.005**	**0.0010**	5.61
966	15:39	332.0	1	0.041	0.0113	**0.004**	**0.0011**	5.61
1033	15:13	7.4	1	0.052	0.0141	**0.005**	**0.0012**	2.81
1054	15:37	17.8	2	0.036	0.0074	**0.002**	**0.7928**	4.49
1072	16:29	26.5	1	0.024	0.0047	**0.004**	**0.0007**	1.87
1077	15:37	28.9	1	0.022	0.0071	**0.002**	**0.0007**	3.46
1079	15:20	29.8	2	0.043	0.0086	**0.004**	**0.0007**	2.99
1082	16:12	31.2	2	0.035	0.0059	**0.005**	**0.0008**	3.46
1105	06:50	41.7	2	0.008	0.0021	**0.002**	**0.0005**	4.49
1113	16:03	45.6	1	**0.019**	**0.0052**	0.002	0.0006	3.46
1124	17:27	50.6	1	**0.013**	**0.0016**	0.004	0.0006	1.45
1138	08:27	56.8	6	**0.136**	**0.0060**	0.013	0.0006	3.21
1152	07:08	63.1	2	**0.014**	**0.0024**	0.003	0.0004	2.99
1159	08:54	66.2	2	**0.077**	**0.0052**	0.006	0.0004	5.64
1163	14:48	68.1	2	**0.074**	**0.0073**	0.005	0.0005	4.49
1176	08:10	73.8	1	**0.020**	**0.0034**	0.002	0.0004	5.61
1176	16:16	74.0	1	**0.008**	**0.0027**	0.001	0.0004	4.99
1181	15:57	76.2	3	**0.021**	**0.0029**	0.003	0.0004	3.61
1187	07:45	78.8	3	**0.026**	**0.0030**	0.004	0.0004	4.08
1190	15:40	80.3	3	**0.066**	**0.0041**	0.008	0.0005	4.08
1193	15:43	81.6	3	**0.048**	**0.0038**	0.006	0.0005	4.99
1194	08:52	81.9	1	**0.040**	**0.0064**	0.004	0.0006	4.08
1211	08:21	89.6	6	**0.049**	**0.0044**	0.005	0.0005	3.46
1215	16:15	91.6	2	**0.020**	**0.0025**	0.003	0.0004	2.99
1216	07:29	91.9	3	**0.018**	**0.0023**	0.003	0.0004	3.21
1234	15:11	100.2	1	**0.032**	**0.0036**	0.004	0.0004	2.99
1235	07:22	100.5	5	**0.031**	**0.0023**	0.006	0.0004	3.21
1241	15:27	103.5	1	**0.031**	**0.0031**	0.004	0.0004	3.74
1246	08:24	105.7	2	**0.063**	**0.0036**	0.008	0.0005	5.61
1258	07:46	111.3	4	**0.051**	**0.0029**	0.009	0.0005	3.46
1268	16:18	116.2	2	**0.032**	**0.0022**	0.006	0.0004	3.21
1278	15:56	120.9	4	**0.058**	**0.0035**	0.007	0.0004	3.21
1298	15:34	130.7	3	**0.020**	**0.0024**	0.003	0.0003	2.81
1302	08:42	132.5	3	**0.016**	**0.0022**	0.002	0.0003	5.64

1302	16:12	132.7	2	**0.010**	**0.0020**	0.002	0.0004	3.46
1306	08:20	134.5	5	**0.167**	**0.0037**	0.020	0.0004	4.49
1309	15:17	136.2	2	**0.047**	**0.0043**	0.005	0.0005	5.61
1314	08:46	138.6	1	**0.067**	**0.0047**	0.006	0.0004	4.99
1326	17:33	144.9	4	**0.008**	**0.0011**	0.004	0.0005	2.14
1340	15:25	152.2	4	0.106	0.0067	**0.012**	**0.0007**	3.21
1347	07:35	155.7	1	0.036	0.0044	**0.005**	**0.0006**	3.21
1352	15:35	158.6	1	0.073	0.0066	**0.008**	**0.0007**	5.64

Table A.2: Supra-Horizon Movie summary table.

Sol	**LTST**	L_S	**Qual.**	τ_{HC}	$\pm 95\%$	τ_{WA}	$\pm 95\%$	λ_{CHAR}
23	14:07	163.0	7	**0.030**	**0.007**	0.002	0.001	7.21
25	14:30	164.0	6	**0.051**	**0.014**	0.003	0.001	4.81
40	15:22	172.6	6	**0.057**	**0.011**	0.003	0.001	7.21
50	15:37	178.3	5	**0.026**	**0.011**	0.003	0.001	7.21
55	16:50	181.2	3	**0.022**	**0.009**	0.002	0.001	4.81
59	16:51	183.6	2	**0.019**	**0.008**	0.003	0.001	4.81
67	15:06	188.2	2	**0.020**	**0.010**	0.002	0.001	4.81
84	14:16	198.4	1	**0.050**	**0.013**	0.004	0.001	4.81
95	15:51	205.2	2	**0.037**	**0.010**	0.004	0.001	8.01
101	12:22	208.8	5	0.245	0.032	**0.016**	**0.002**	6.01
103	16:14	210.2	4	0.103	0.026	**0.010**	**0.003**	9.01
123	18:01	222.9	4	0.009	0.003	**0.007**	**0.003**	1.80
139	12:09	233.0	1	0.165	0.084	**0.006**	**0.003**	4.81
142	12:08	235.0	2	0.068	0.043	**0.003**	**0.002**	3.60
155	12:31	243.4	1	0.030	0.012	**0.008**	**0.003**	4.88
175	11:48	256.4	1	0.024	0.010	**0.007**	**0.003**	4.88
184	14:57	262.4	2	0.063	0.025	**0.005**	**0.002**	4.81
233	12:20	293.6	3	0.056	0.032	**0.003**	**0.002**	6.01
312	12:26	340.0	1	0.044	0.039	**0.003**	**0.003**	4.81
317	14:40	342.7	1	0.022	0.021	**0.002**	**0.002**	8.01
388	14:41	19.0	2	**0.032**	**0.012**	0.004	0.001	6.51
435	14:43	41.2	3	**0.013**	**0.006**	0.002	0.001	5.33
505	12:40	72.8	3	**0.009**	**0.006**	0.001	0.001	5.86
507	13:45	73.8	4	**0.009**	**0.005**	0.001	0.001	5.33
507	15:47	73.8	1	**0.011**	**0.005**	0.002	0.001	4.88
517	12:34	78.3	4	**0.011**	**0.005**	0.001	0.001	4.88

520	11:29	79.6	4	**0.011**	**0.005**	0.001	0.001	5.33
522	12:07	80.5	2	**0.010**	**0.005**	0.001	0.001	5.86
527	16:21	82.8	2	**0.007**	**0.003**	0.002	0.001	5.86
530	12:40	84.0	2	**0.007**	**0.004**	0.001	0.001	8.38
539	13:25	88.1	3	**0.010**	**0.004**	0.002	0.001	7.33
541	15:33	89.1	2	**0.010**	**0.004**	0.002	0.001	4.88
553	12:00	94.5	3	**0.010**	**0.005**	0.001	0.001	5.33
564	16:01	99.6	3	**0.003**	**0.003**	0.001	0.001	5.86
575	14:34	104.7	2	**0.007**	**0.004**	0.001	0.001	4.51
579	12:25	106.5	4	**0.019**	**0.004**	0.003	0.001	6.51
583	16:08	108.4	1	**0.008**	**0.003**	0.002	0.001	4.51
590	13:45	111.6	1	**0.017**	**0.003**	0.003	0.001	7.33
914	12:24	301.3	1	0.151	0.021	**0.007**	**0.001**	4.22
927	16:00	309.3	2	0.026	0.005	**0.004**	**0.001**	3.05
939	12:21	316.3	1	0.100	0.015	**0.008**	**0.001**	7.84
961	12:17	329.1	1	0.059	0.017	**0.004**	**0.001**	4.98
1079	12:51	29.7	1	0.049	0.017	**0.002**	**0.001**	7.18
1098	11:53	38.6	1	0.051	0.017	**0.002**	**0.001**	6.64
1138	8:33	56.8	4	**0.104**	**0.010**	0.005	0.001	5.21
1159	8:49	66.2	3	**0.084**	**0.011**	0.004	0.001	7.12
1171	16:15	71.8	1	**0.062**	**0.005**	0.004	0.000	5.21
1173	16:10	72.7	3	**0.063**	**0.007**	0.004	0.000	5.21
1187	7:46	78.8	3	**0.119**	**0.009**	0.007	0.001	6.08
1190	15:45	80.3	3	**0.102**	**0.009**	0.005	0.001	6.63
1194	8:47	81.9	1	**0.102**	**0.013**	0.005	0.001	6.08
1206	16:33	87.5	1	**0.028**	**0.006**	0.002	0.001	4.56
1210	16:33	89.3	1	**0.040**	**0.006**	0.003	0.001	6.63
1216	7:24	91.9	4	**0.152**	**0.008**	0.011	0.001	3.65
1235	7:31	100.6	1	**0.053**	**0.007**	0.004	0.001	5.98
1252	14:45	108.6	1	**0.053**	**0.007**	0.003	0.000	4.56
1258	7:41	111.3	4	**0.081**	**0.007**	0.006	0.001	5.21
1259	13:28	111.8	2	**0.021**	**0.003**	0.003	0.000	10.43
1261	13:06	112.8	1	**0.017**	**0.003**	0.002	0.000	12.16
1263	15:11	113.8	4	**0.016**	**0.004**	0.002	0.001	7.29
1265	8:31	114.6	2	**0.028**	**0.003**	0.004	0.000	6.08
1268	16:26	116.2	3	**0.014**	**0.003**	0.002	0.001	5.21
1270	13:18	117.0	1	**0.004**	**0.003**	0.001	0.000	12.16
1272	10:13	117.9	3	**0.016**	**0.004**	0.002	0.001	12.16
1276	15:41	120.0	1	**0.015**	**0.002**	0.002	0.000	9.12
1280	8:34	121.7	1	**0.010**	**0.003**	0.001	0.000	10.42
1283	15:49	123.3	2	**0.019**	**0.002**	0.003	0.000	8.10

1286	8:33	124.7	5	**0.049**	**0.003**	0.007	0.000	6.08
1289	12:07	126.2	1	**0.013**	**0.003**	0.002	0.000	14.59
1292	7:25	127.6	8	**0.085**	**0.002**	0.016	0.000	7.29
1297	14:17	130.2	1	**0.019**	**0.002**	0.002	0.000	10.42
1299	13:45	131.1	2	**0.020**	**0.002**	0.003	0.000	11.21
1302	8:51	132.5	8	**0.045**	**0.004**	0.005	0.001	7.29
1304	14:03	133.6	3	**0.041**	**0.003**	0.005	0.000	7.29
1306	8:29	134.5	5	**0.045**	**0.003**	0.006	0.000	9.12
1309	15:26	136.2	1	**0.011**	**0.003**	0.002	0.000	10.43
1312	9:07	137.6	2	**0.023**	**0.003**	0.003	0.000	8.10
1314	13:30	138.7	5	**0.067**	**0.005**	0.009	0.001	14.61
1319	12:17	141.2	5	**0.024**	**0.003**	0.003	0.000	14.95
1328	11:53	145.8	3	**0.042**	**0.005**	0.005	0.001	12.16
1331	9:31	147.3	5	0.088	0.006	**0.010**	**0.001**	9.12
1333	14:52	147.3	1	0.022	0.005	**0.003**	**0.001**	6.08
1336	9:20	149.9	2	0.050	0.006	**0.006**	**0.001**	8.10
1338	13:50	151.1	4	0.096	0.006	**0.011**	**0.001**	6.63
1343	9:38	153.6	1	0.021	0.009	**0.002**	**0.001**	8.10
1350	12:59	157.5	2	0.098	0.010	**0.010**	**0.001**	9.12
1351	12:54	158.0	1	0.076	0.008	**0.007**	**0.001**	6.08
1352	15:35	158.6	5	0.091	0.006	**0.011**	**0.001**	5.61

Appendix B

Radiometric Calibration of ThorLabs DCC1545 Imager

B.1 Introduction

Obtaining absolute spectral radiance from pixel intensity or digital number (DN) necessitates the radiometric calibration of the imaging device. This calibration requires understanding how the output of the camera responds to a given input of spectral radiance, and must take into account all instrument parameters that effect light input or the instrument's output. These factors include incident power on the camera's sensor, the quantum efficiency of the sensor (QE), the exposure time, the aperture of the lens as well as the lens transmission. Each of these has some impact on the DN, and an accurate calibration must convolve all of these together in order to understand the relative contribution that each has on the camera output. This document aims to provide a comprehensive overview of the process undertaken to radiometrically calibrate a ThorLabs DCC1545 CMOS camera, referred to as "ThorCam.

The calibration was performed using an integrating sphere, two broadband light sources, and a set of laser line filters. The system was simplified by controlling the aperture of the lens. Because the aperture of the lens requires manual adjustment, its setting cannot be accurately known. Given a constant illumination, an imperceptible difference in aperture adjustment can significantly affect the DN. To minimize uncertainty, the maximum aperture was used and the exposure time was varied. Thus, the calibration sought the relationship between DN, spectral radiance, and exposure time, such that the final conversion factor would have units of W ms DN^{-1} m^{-2} Sr^{-1}.

B.2 Instrumentation

B.2.1 ThorCam CMOS Imager

The ThorCam is a VIS/NIR imager that uses a monochromatic CMOS sensor with a 1280×1024 pixel resolution. The DCC1545 model has a bit depth of 8 bits per pixel, giving each pixel a possible DN between 0 and 255. The CMOS sensor is sensitive to wavelengths between 400 nm and 1000 nm, with the QE peaking in the visible part of the electromagnetic spectrum at 570 nm. The QE curve for the CMOS sensor is shown in figure 5.2b.

B.2.2 MVL12WA Lens

Fixed to the ThorCam is a 12mm focal length lens with an aperture of 1.4 mm. The resulting FOV is 38.5° specified for the diagonal. The lens itself attenuates light, and while this attenuation is relatively small, it must be taken into account in order to accurately characterize the spectral radiance at the camera's sensor. The transmission data for the MVL12WA lens, provided by ThorLabs, is shown below in figure B.1.

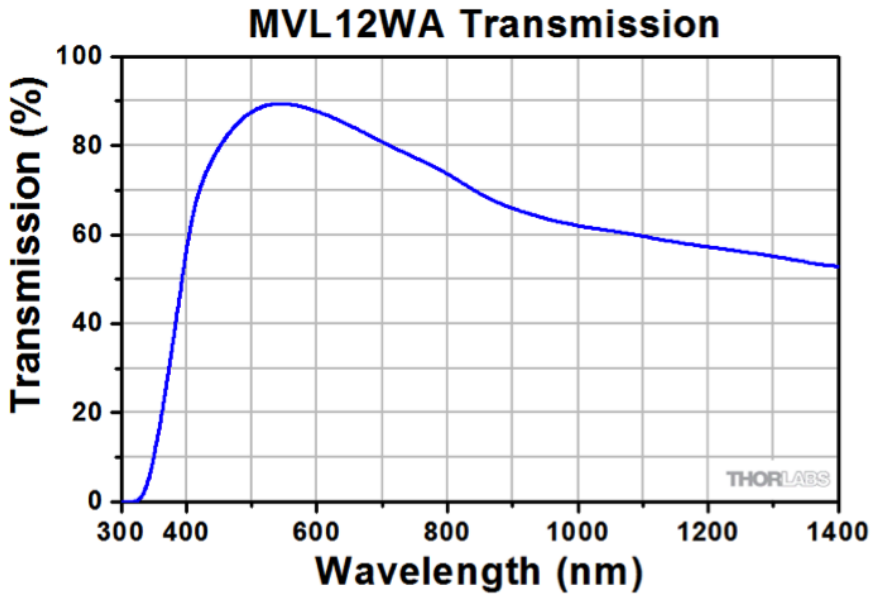

Figure B.1: Lens Transmission for the MVL12WA Lens using for the calibration and Lidar-coordinated experiments.

B.2.3 Integrating Sphere

An integrating sphere 30 cm in diameter was used to generate the flat field images necessary for the calibration. The inner surface of the integrating sphere is coated in Barium Sulfate

($BaSO_4$), whose reflectance spectrum is shown below in figure B.2. The integrating sphere was equipped with two ports, which shall be referred to as the entrance port and detection port. The entrance port was 7 cm in diameter, and was the point of entry for the power source, which illuminated the sphere's inner surface. The detection port was 7.5 cm in diameter and was where the ThorCam was positioned to acquire the flat field images. The port fraction, denoted as f, is the ratio of the port area relative to the total area of the integrating sphere, which was measured to be 0.0216.

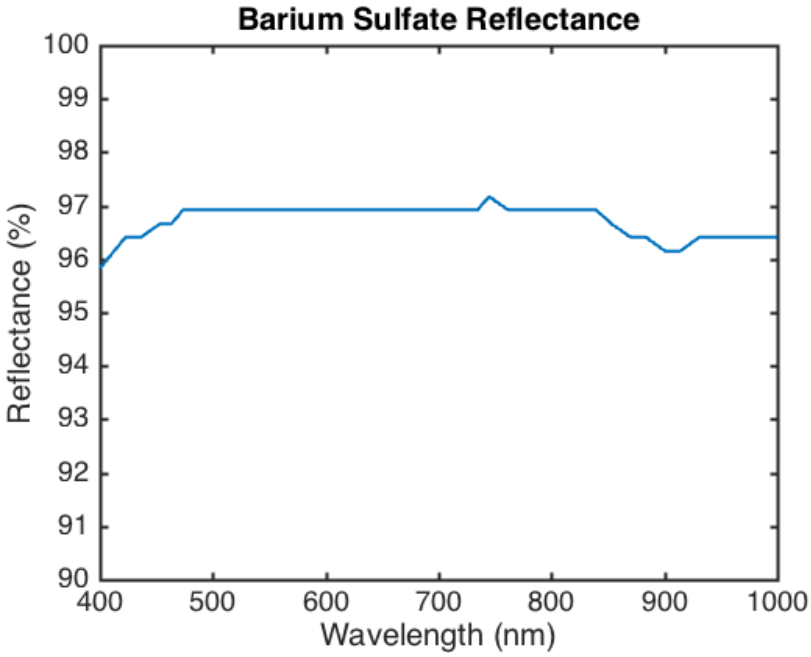

Figure B.2: Reflectance spectra for Barium Sulfate ($BaSO_4$).

B.2.4 Power Sources

Two broadband power sources were used to perform the calibration: an SLS 201 manufactured by ThorLabs, and a xenon arc lamp manufactured by Newport. The SLS 201 is a tungsten halogen stabilized light source that provides a blackbody radiation spectrum from $300 - 2300$ nm, with a peak wavelength of 1000 nm. The normalized spectral power distribution for the SLS 201 is provided in figure B.3a. The total power across all wavelengths is 10 mW, however the in-band power for the ThorCam is approximately 3.2 mW. The xenon arc lamp is substantially more powerful than the SLS 201, and puts out a total power 300 W distributed over wavelengths between 200 nm and 2400 nm. The irradiance of the xenon arc lamp provided by the manufacturers is shown in figure B.3b.The spectral distribution of the SLS 201 and the xenon arc lamp were measured using a combination of UV and NIR

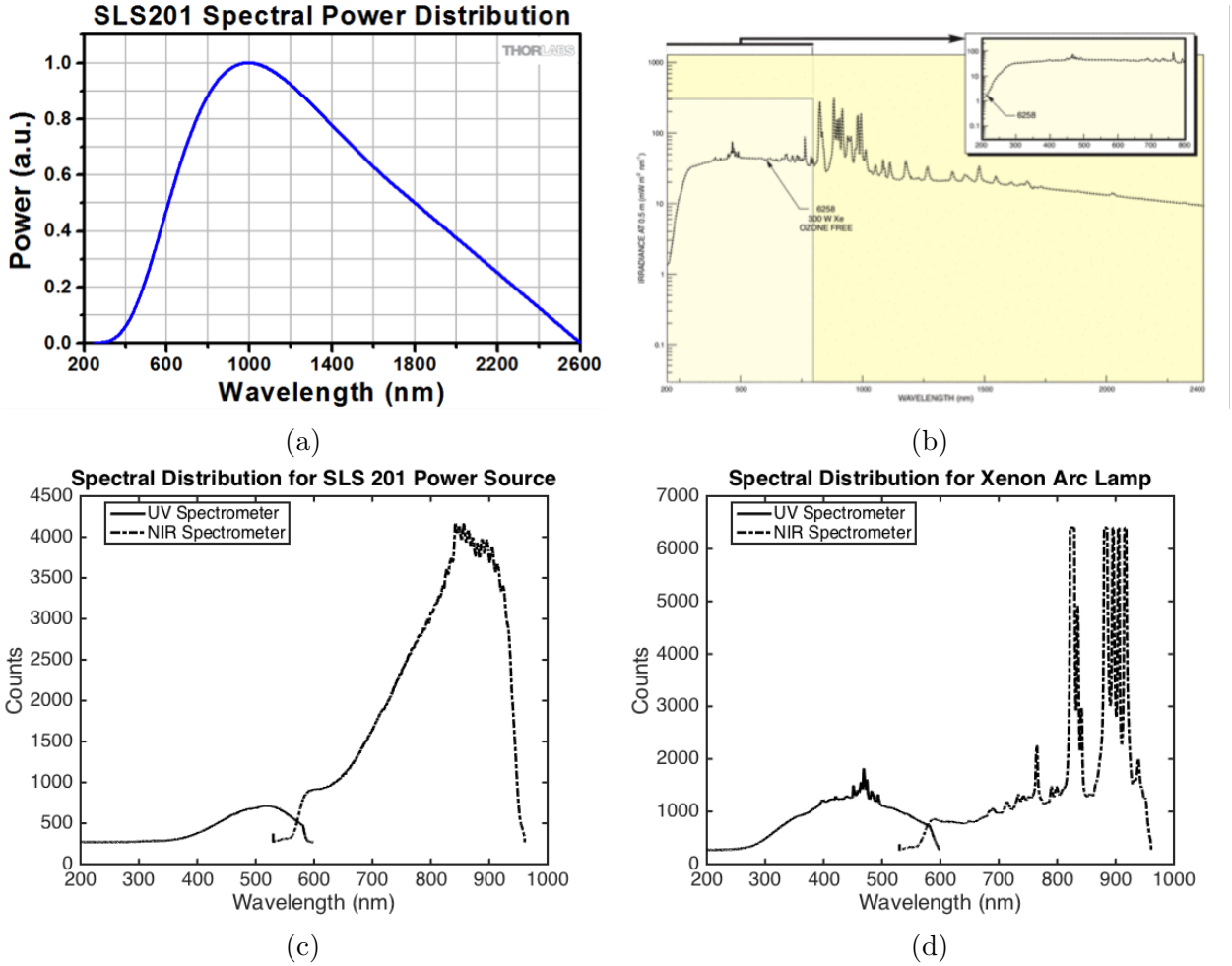

Figure B.3: (a) Normalized power distribution for the SLS 201 power source. The combined power of all wavelengths is 10mW, however the in-band power is 3.2 mW. (b) Spectral distribution of xenon arc lamp provided by the manufacturer. (c) Spectral distribution for the SLS 201 measured with using a Maya 2000 UV and NIR Spectrometer.(d) Spectral distribution for the Xenon Arc Lamp measured with using a Maya 2000 UV and NIR Spectrometer.

spectrometers, which are shown in figure B.3c and B.3d, respectively.

B.2.5 Filters

The calibration was performed at specific wavelengths through the use of a set of laser line filters manufactured by Thorlabs. Each filter varied slightly in percent transmission (see figure B.4a below for transmission data), and had a Full Width Half Maximum (FWHM) of 10 nm. The wavelengths of the nine filters used for the calibration using the Xenon Arc source were: 400 nm, 450nm, 500nm, 550nm, 600nm, 650nm, 700nm, 750nm, and 800nm. Due to the low power output by the SLS 201 at short wavelengths, the 400nm and 450nm

filters could not be used with this light source, however the xenon arc lamp utilized all nine filters. The width of each filter was tested using a UV and NIR spectrometer to test the specifications provided by the manufacturers.

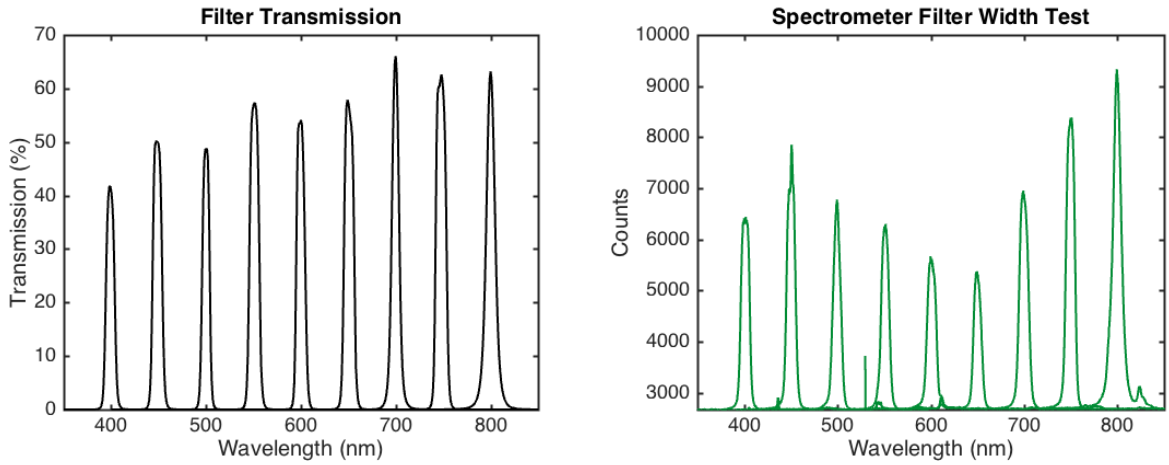

(a) (b)

Figure B.4: (a) Transmission data for each filter used in the calibration. (b) Spectral distribution for each calibration filter using the xenon arc lamp and UV and NIR spectrometers. This test was performed to determine how the bandpass of each filter compared to the expected value provided by ThorLabs.

Throughout the calibration process, each filter served two functions. The first was to determine the power output at each filter wavelength of the power sources. This was achieved through the use of a Newport 843-R laser power meter which was positioned at the entrance port of the integrating sphere which was illuminated with the power source. Secondly, each filter was used to take a filtered flat field image with the ThorCam in order to understand the camera's output at each filter wavelength. The apparatus used to acquire the flat field images is shown in figure B.5.

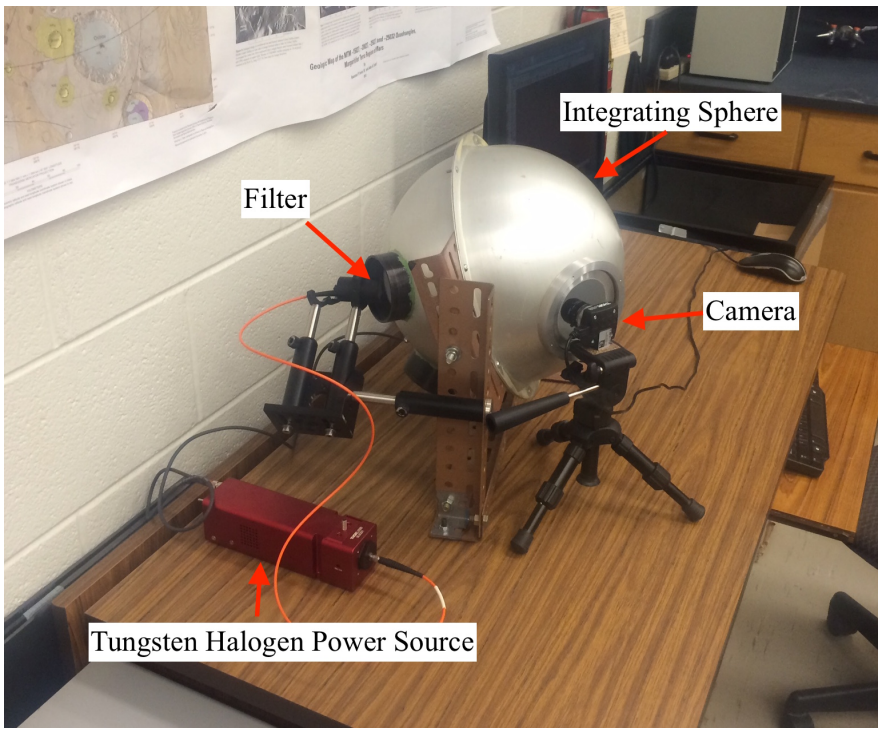

Figure B.5: Flat field image apparatus.

B.3 Data Acquisition and Analysis

B.3.1 Flat Field Image Acquisition Procedure

Using the set up depicted in figure B.5, flat field images were acquired with each of the filters discussed in section B.2.5 at a range of different exposure times. The steps taken to acquire the images are described as follows:

1. Power up the power source, and position the beam of light such that the entire beam falls on the baffle
2. Connect the camera to the computer, and open the ThorCam software
3. Open the aperture on the ThorCam all the way and tighten the locking screw
4. Focus the camera on the hemispheric seam within the integrating sphere
5. Position the FOV of the camera to a blank region of the integrating sphere, away from the hemispheric seam and shadowed regions created by the baffle
6. Place the appropriate filter in front of the source beam
7. Adjust the exposure time to initial minimum setting (this varied for each power source)
8. Increase exposure time at set intervals, capturing an image at each adjusted exposure time.
9. Switch the filter, and repeat steps 8 and 9
10. Put the lens cap on and repeat steps 8 and 9 to capture dark current

In total, there were 63 flat field images captured for the SLS 201, given 9 exposure times associated with each of the 7 filters; for the xenon arc lamp, 36 flat field images were captured given 4 exposure times and 9 filters. To eliminate anomalous effects exhibited by the outer edges of the flat field images, each image was cropped to remove the outer 10 columns and rows. Thus, each new flat field image was comprised of 1004 vertical pixels and 1260 horizontal pixels. All subsequent analysis discussed was performed using the cropped images. Furthermore, each image was dark corrected prior to analysis.

B.3.2 Radiometric Fall Off

For an idealized flat field image, the image sensor is uniformly exposed, and thus the pixel intensity should also be spatially uniform over the entire image. However, the geometry of the photographic system must be taken into consideration. It is known that for a uniformly

illuminated image, the image brightness decreases with increasing radial distance from the image centre. This is known as radiometric fall off, also commonly referred to as vignetting. The amount by which the brightness decreases, for a lens with ideal properties, is quantified by the cosine fourth law and is given as equation B.1 below:

$$y = \cos^4(\theta) \tag{B.1}$$

Here, θ is the subtended angle between the image centre and a given pixel, which can be determined by using the FOV of the camera's lens, and y denotes the pixel intensity in DN. By taking the average DN of a ring of pixels of an expanding radius centred on the image centre, a comparison of the radiometric fall off can be made to an idealized version of the system. This was executed for the 900 ms exposed flat field image (with dark current subtracted) for each filter of the SLS 201. Each curve was then normalized, and averaged together, the result of which is compared to the cosine fourth law in figure B.6.

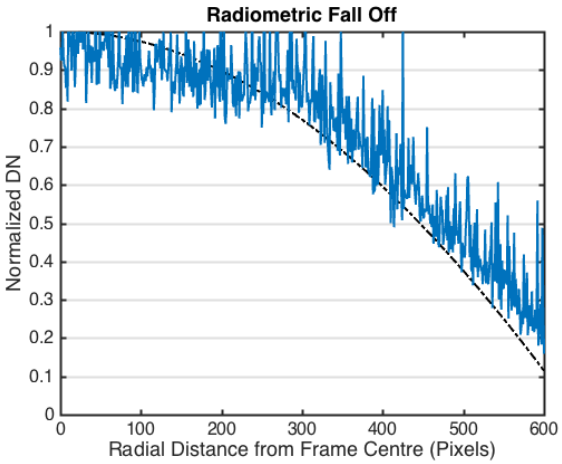

Figure B.6: Radiometric fall off for flat field images showing the cosine fourth law (dashed line), which shows how the intensity decreases with increasing radial distance from the image centre for a uniformly illuminated image. The red line shows the averaged radiometric fall off for the 900ms exposed flat field image for each filter.

B.3.3 Response Linearity

Knowledge of the relationship between exposure time and the DN is critical to making spectral radiance determinations from the DN values. The rate at which the DN changes with exposure time is dependent on the incident power, the quantum efficiency of the camera's sensor and the lens transmission. Figure B.7 plots the average DN as a function of exposure time for the SLS 201 power source and the xenon arc lamp.

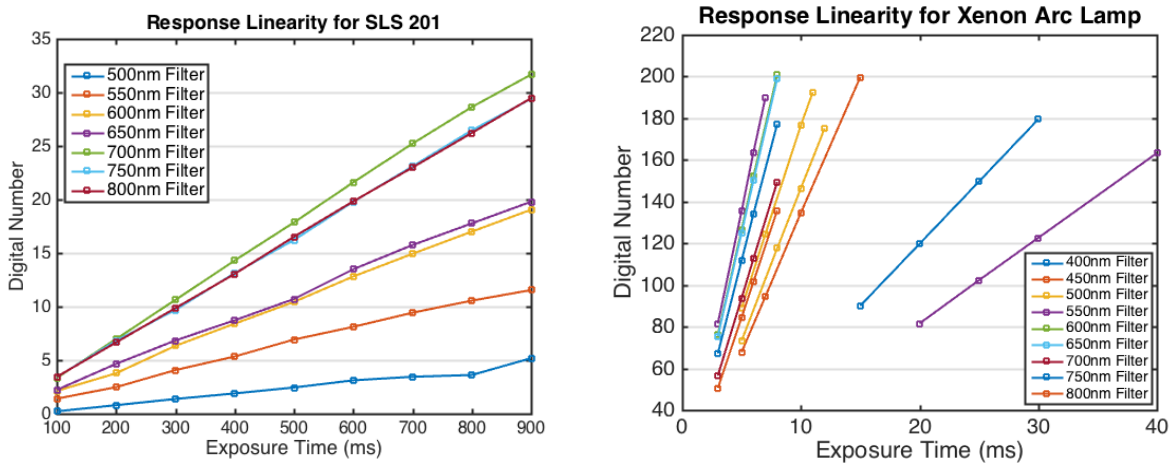

(a) (b)

Figure B.7: (a) Average DN vs exposure time for each filter series using the SLS 201 power source. The rate at which the DN changes with exposure time for each filter depends on the incident power, QE, and lens transmission. (b) Average DN vs exposure time for each filter series using the Xenon Arc Lamp.

Because each filter series has a unique power, quantum efficiency and lens transmission associated with it, the rate at which the DN changes with exposure time will differ for each series by an amount proportional to the product of the power, quantum efficiency and lens transmission. Note that this is only the case given that the reflectance of the integrating sphere is nearly constant at all filter wavelengths (see figure B.2).

Each filter series was linearly fit in order to obtain the slope of each line as well as the y-intercept. The slope represents the rate at which the DN changes with exposure time for each filter series, and is further divided by the bandpass of the filter to account for the wavelength interval over which the flat field was acquired. The y-intercept represents the DN produced for a 0 ms exposure time, also known as the offset. Given that each flat field image has already been dark and bias corrected, the offset represents a non-real DN value that should be subtracted from each pixel of each flat field image. However, as is shown in table B.1, for each filter series the offset is a non-integer value. The data-fitting algorithm in some cases produced a line with a negative offset, however in all cases the offset is insignificant as it is near to zero. For the remainder of this analysis, it is ignored.

B.3.4 Measured Power and Calibration Results

Using the Newport 843-R power meter, the power was measured at the entrance port of the integrating sphere for the SLS 201 and the xenon arc lamp. The resultant power data from these measurements, plotted in figures B.8 and B.8b, were converted to spectral radiance by

Table B.1: Table showing the slope and offset obtained from a linear fit of each filter series of flat field images for the SLS 201 and xenon arc lamp power sources.

	SLS 201		**Xenon Arc Lamp**	
$\lambda(nm)$	DN/ms/nm	Offset	DN/ms/nm	Offset
400	-	-	0.60	0.004
450	-	-	1.35	-0.01
500	6.3e-4	-0.35	1.78	0.03
550	1.4e-3	0.13	2.53	0.004
600	2.2e-3	-0.2	2.51	-0.02
650	2.3e-3	0.08	1.88	0.004
700	3.6e-3	-0.09	2.23	0.02
750	3.3e-3	0.08	1.68	0.03
800	3.3e-3	0.13	1.46	0.02

dividing by the area of the sensor for the power meter (1 cm^2), the bandwidth of the filter (10 nm), and the projected solid angle of the integrating sphere (π). To get the conversion factor needed, the DN/ms/nm term is divided by the calculated spectral radiance for each filter wavelength. This gives units of DN m^2 Sr W^{-1} ms^{-1}. This can be interpreted as the DN per radiance per ms exposure time. The conversion factor, plotted as a function of wavelength is shown below in figure B.8c for the SLS 201 and the xenon arc lamp. The final conversion factor was obtained by taking the average for both power sources across all of the wavelengths, which was found to be 2.33×10^{-3} W ms DN^{-1} m^{-2} Sr^{-1}.

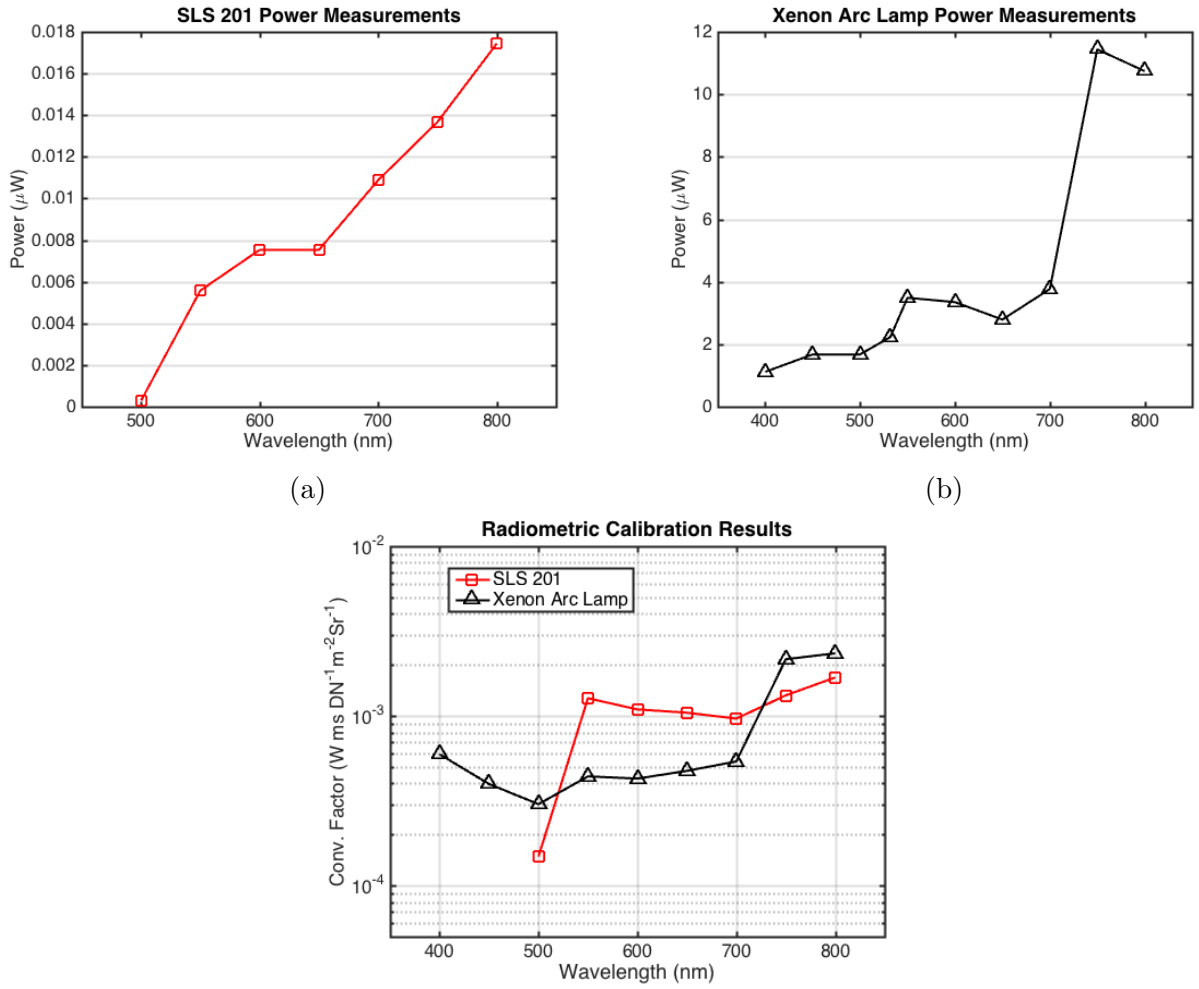

Figure B.8: (a) Power measurements of the SLS 201 light source acquired using the Newport 843-R power meter at the entrance port of the integrating sphere. (b) Power measurements acquired of the xenon arc lamp using the Newport 843-R power meter at the entrance port of the integrating sphere. (c) Calibration results showing the conversion factor on the y-axis with units of W ms DN^{-1} m^{-2} Sr^{-1} and wavelength in nm on the x-axis. The final conversion factor was obtained by taking the average conversion factor for both power sources across all of the calibration wavelengths.